

Alma Mater Studiorum – Università di Bologna

DOTTORATO DI RICERCA IN

FISICA

Ciclo XIII

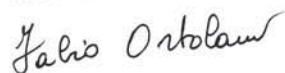
Settore scientifico-disciplinare di afferenza: FIS/03 FISICA DELLA MATERIA

Advanced SPM studies on the growth of ultrathin films of organic
semiconductors at metal and dielectric interfaces

Presentata da: Andreas Straub

Coordinatore Dottorato

Prof. Fabio Ortolani



Relatori



Prof. Federico Boscherini

Prof. Fabio Biscarini



Esame finale anno 2011

Summary

1. Introduction/Motivation/Abstract	3
2. Fundamentals	4
2.1. Organic semiconductors and organic electronics	4
2.2. Growth phenomena at surfaces: OMBD and thin films	8
2.3. Scanning Probe Microscopy techniques	11
2.3.1. Non-contact AFM	11
2.3.2. Scanning tunnelling microscopy	13
3. Materials and experimental setup	15
3.1. Molecules	15
3.1.1. Sexithiophene 6T	16
3.1.2. Pentacene	21
3.1.3. Perylene PDI8CN2	21
3.2. Substrates and preparation techniques	22
3.2.1. Graphite (HOPG)	22
3.2.2. Native silicon oxide (Si/SiO _x 2 nm)	26
3.2.3. Gold single crystal – Au(111)	27
3.2.4. Polycrystalline Au	28
3.2.5. OFET testpattern structures	31
3.3. Experimental setup	35
3.3.1. UHV system overview	35
3.3.2. Custom-built vibration isolation	39
3.3.3. VT-UHV SPM	43
3.3.4. In-situ OME cell and real-time SPM	45
3.4. SPM tips, mounting and fabrication	50
3.4.1. STM tips	51
3.4.2. AFM tips	54
4. Organic-metal and organic-dielectric interface	55
4.1. T6 on Au(111) single crystal	56
4.2. T6 on polycrystalline gold surfaces	63
4.3. T6 on native silicon oxide	68
4.4. T6 on indium tin oxide	68
4.5. Pentacene and perylene on device testpatterns	78
5. In-situ real-time morphology evolution of 6T on native silicon oxide at variable temperature	84
5.1. Motivation	84
5.2. Experimental	85
5.3. Results	87
6. Real-time in-situ deposition on technological OFET testpatterns	96
6.1. 6T on Trento-type testpattern	99
6.2. 6T on Fraunhofer-type testpattern	100
6.3. Molecular reorganization during OMBD and NC-AFM	104
6.4. Summary	111
7. References	112

1. Introduction/Motivation/Abstract

Many studies on the morphology, molecular orientation, device performance, substrate nature and growth parameter dependence have been carried out since the proposal of Sexithiophene (6T) for organic electronics [1]

However, these studies were mostly performed on films thicker than 20nm and without specifically addressing the relationship between morphology and molecular orientation within the nano and micro structures of ultrathin films of 0-3 monolayers.

In 2004, the observation that in OFETs only the first few monolayers at the interface in contact with the gate insulator contribute to the charge transport [2], underlined the importance to study submonolayer films and their evolution up to a few monolayers of thickness with appropriate experimental techniques.

We present here a detailed Non-contact Atomic Force Microscopy and Scanning Tunneling Microscopy study on various substrates aiming at the investigation of growth mechanisms. Most reported similar studies are performed on ideal metals in UHV. However it is important to investigate the details of organic film growth on less ideal and even technological surfaces and device testpatterns. The present work addresses the growth of ultra thin organic films in-situ and quasi real-time by NC-AFM. An organic effusion cell is installed to evaporate the organic material directly onto the SPM sample scanning stage.

2. Fundamentals

2.1. Organic semiconductors and organic electronics

The interesting electronic properties of organic semiconductors have already been investigated in the early 20th century [3, 4]. Basic charge carrier transport models [5, 6] were established around 1980 driven by the discovery of electroluminescent organic materials in 1960.

After the first organic semiconductor application in 1970, the first metal oxide semiconductor structure was demonstrated in 1983 [7].

The breakthrough of organic electronics came with the demonstration of the first organic field effect transistor (OFET) also termed organic thin film transistor (OTFT) in 1986 [8]. At the same time, the development of an organic heterojunction solar cell and an organic light emitting diode were reported. The later developed soluble organic semiconductors promise to be useful for production process upscaling and printable circuits [9, 10]. However the performance of organic electronics devices remain some orders of magnitude below the performance offered by crystalline silicon devices.

Nowadays, the charge carrier transport in organic semiconductors and the charge injection at the organic/gold interface are not well understood.

Figure 2.1.1A shows the sp² hybridization with the perpendicular p_z-orbital. Each of the three sp² orbitals contains one electron and so does the p_z-orbital. In a molecular chain of alternating double and single bonds the overlapping sp² orbitals form a σ-bond while the overlapping p_z-orbitals form the π-bond like illustrated in Figure 2.1.1B. The σ-bonds are much stronger than the weaker π-bonds. On an isolated molecule, the energy levels are discrete and shown schematically in Figure 2.1.1D for the ethylene molecule(B).

From an electronical point of view, the most interesting molecular orbitals are the highest occupied orbital (HOMO) and the lowest unoccupied molecular orbital (LUMO). These energy levels form energy bands for the case of an infinitely long organic semiconductor like shown in Figure 2.1.1C. A π conjugated molecule forms delocalized π-bonds perpendicular to the sp² hybridized plane that can transport electrons or holes.

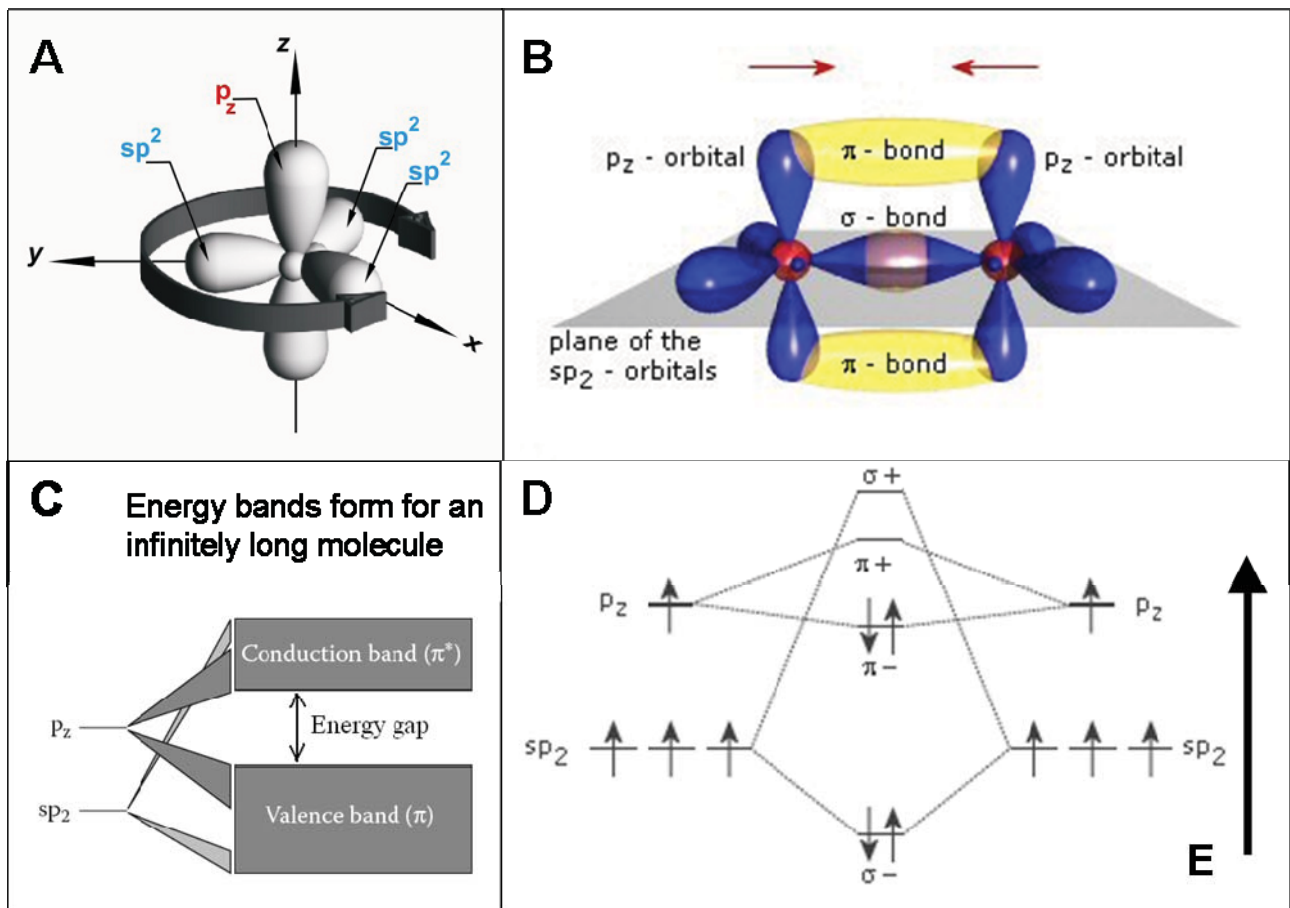


Figure 2.1.1: (A) Atomic orbitals of a carbon atom with sp^2 hybridization. (B) Molecular orbitals of two double bonded carbon atoms forming π -bonds and σ -bonds. (C) An infinitely long conjugated carbon backbone leads to the formation of a conduction band and a valence band. (D) Schematic representation of the molecular energy levels with bonding and antibonding molecular orbitals.

Charge carriers in organic semiconductors can be p-type or n-type carriers. Charge transfer in organic semiconductors occurs via a hopping mechanism describe by transport models related to highly disordered systems. Many amorphous and polycrystalline organic semiconductors sustain either positive or negative charge carriers, but not both. Other than in inorganic semiconductor technologies, n-type and p-type do not refer to the majority carriers in the organic semiconductor. Crystalline materials can usually transport both holes and electrons. Disordered electronic systems instead often only favour one type of charge carrier. Hole transporting organic semiconductors are therefore called p-type semiconductors and n-type semiconductors in the case of electron transporting organic materials. An important complication of both n-type and p-type semiconductors is their poor stability against oxidation and reduction reactions. This is one reason why Organic Material Beam Deposition (OMDB) is carried out in vacuum.

Figure 2.1.2 shows the experimental and theoretical values for the energy gaps for the family of polyacenes. The energy gap can be modified depending on the degree of conjugation in a molecule. The longer the molecule, the smaller the gap.

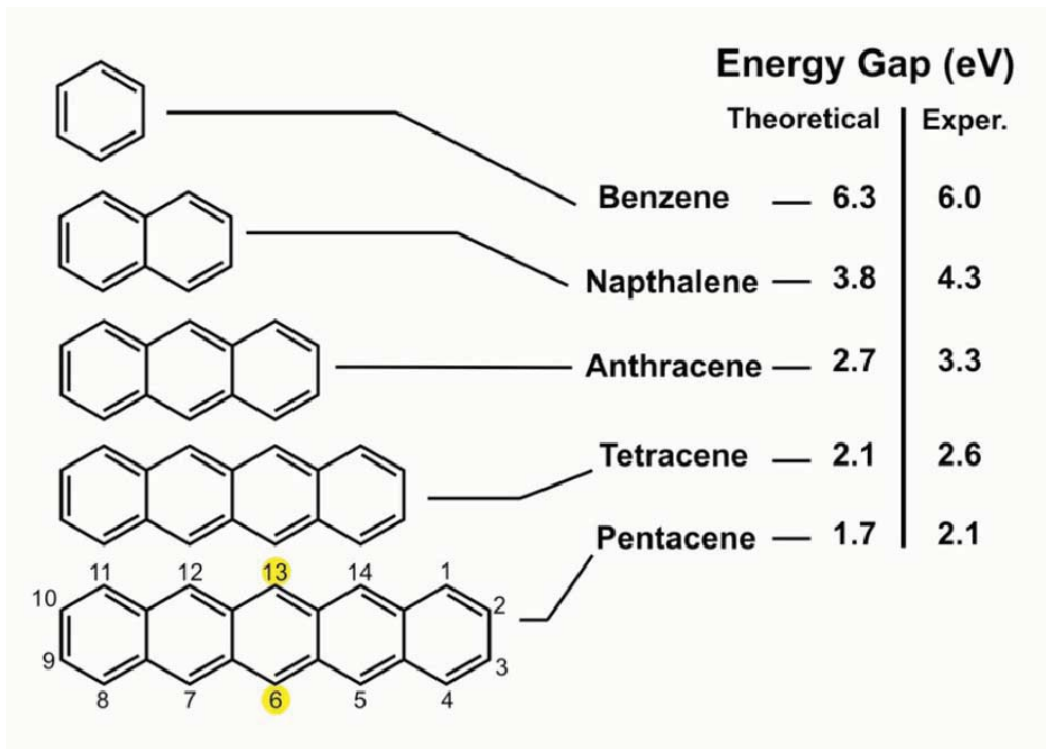


Figure 2.1.2: Molecular structure of the first five polyacenes and their predicted and measured HOMO-LUMO transitions [11]. Note that the carbon atom positions for pentacene have been tagged. Positions 6 and 13 (here in yellow) have been identified as the most exposed to oxidation.

The physical properties of organic semiconductors can be tuned at two different levels. At the molecular level where the chemical structure is responsible for the tailoring of properties and at the supramolecular level where the packing, the order and orientation of molecules with respect to the substrate are relevant.

Established and newly proposed device layouts in organic electronics take advantage of enhanced charge transport properties along preferential directions exploiting molecular orientation and crystallographic axes [12].

From a technological point of view, thin solid films are more attractive for device fabrication than single crystals. One example is the bottom contact OFET layout (used also as test patterns in this work) where a multilayer film of upright standing rodlike organic molecules (e.g. Pentacene, Sexithiophene) form a semiconducting channel on the silicon oxide for charge transport parallel to the surface between source and drain Au electrodes. A sketch of a typical bottom contact test pattern with an upright standing rodlike active organic material is shown in Figure 2.1.3.

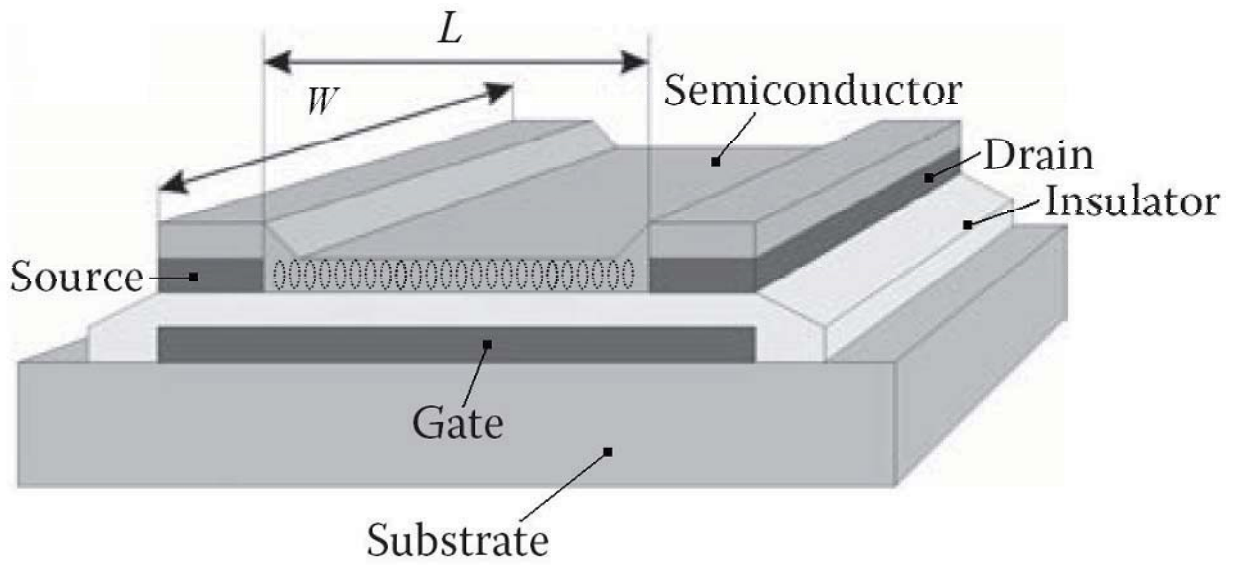


Figure 2.1.3: Typical bottom contact OFET test pattern layout that exploits the preferential standing configuration (here denoted schematically for one single ML) with enhanced charge transport parallel to the surface [13].

2.2. Growth phenomena at surfaces: OMBD and thin films

Growth phenomena at surfaces employing Organic material beam deposition (OMBD) are non equilibrium processes. In Figure 2.2.2 the relevant molecular processes of the complex OMBD growth scenario are schematically represented [REF].

In literature three major growth modes have been identified, namely (1) Frank-van-der-Merwe or layer-by-layer, (2) Stranski-Krastanov or layer-by-layer + islands and (3) Vollmer-Weber or island growth like shown in Figure 2.2.1 together with considerations on the surface energies that favour the growth mode.

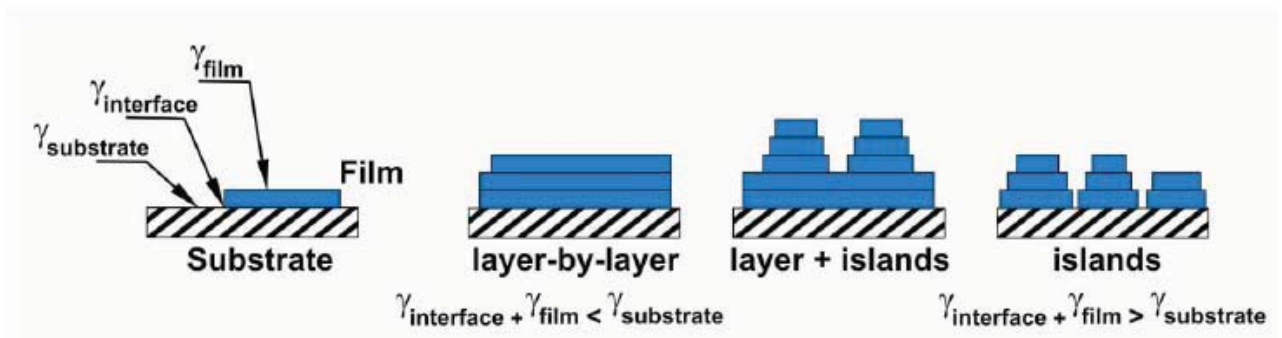


Figure 2.2.1: Growth modes of organic thin films grown by OMBD and considerations about the surface and interface energies that determine the modes [Courtesy of Dr. S.D. Quiroga].

Depending on the growth parameters deposition rate, substrate temperature, substrate (surface energy) and molecule type the growth mode is selected but also transitions between and combinations of these principal growth modes have been reported.

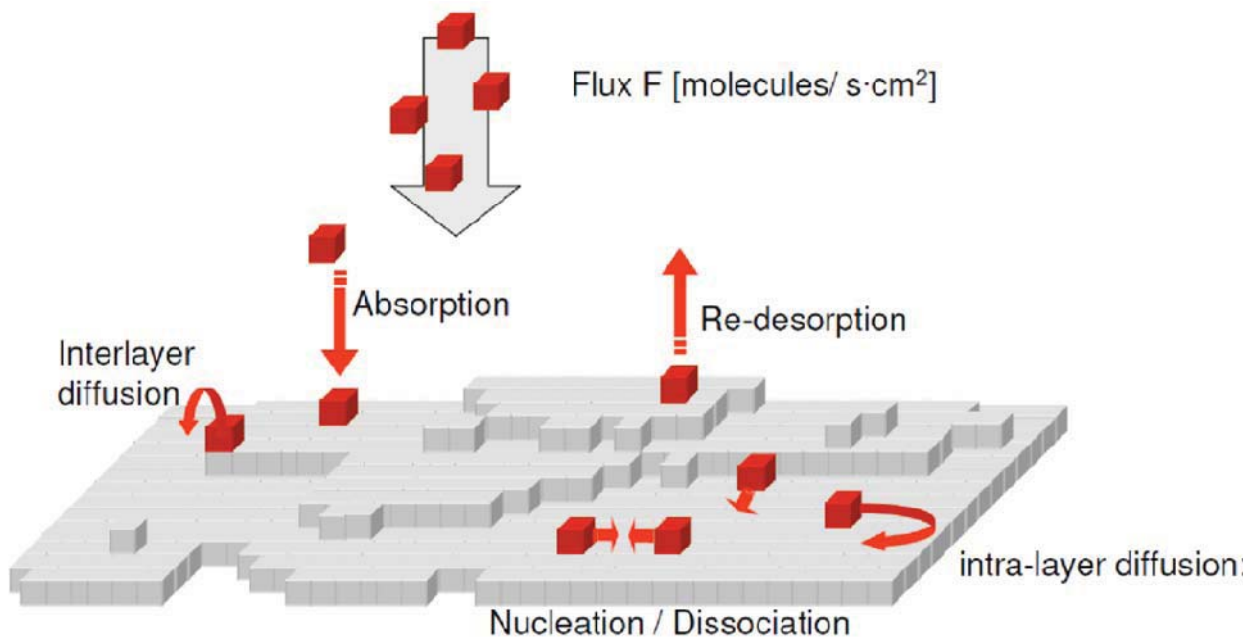


Figure 2.2.2: Schematic representation of dynamic molecular processes at the sample surface during Organic material beam deposition (OMBD).

The film structures growing on the surface (excluding the amorphous form) can be categorized into three phases¹⁴: the bulk crystalline phase, the so-called “thin film” phase and an intermediate flat-lying phase. Sexithiophene and pentacene in the bulk crystalline phase consist of herringbone-type packing, similar to the crystal structure of other small, conjugated molecules^{15,16}. The thin-film phase differs from the bulk phase mainly in terms of $d(001)$ spacing. In the thin-film phase, the long axis of the rodlike molecules stands nearly perpendicular to the substrate, as compared to the tilted axis in the bulk phase; as a result the lattice spacing in the $d(001)$ direction of the thin film phase is slightly longer than that of the bulk phase¹⁷.

In the flat-lying phase, the molecules are oriented with their long axis parallel to the substrate, but this structure is only seen for the first molecular layer(s) on several substrates including metals, clean Si(100) and only for the first layer and submonolayer coverages on silicon oxide. The flat-lying phase is likely substrate-mediated and exists only at the interface, where the molecule-substrate interaction is rather strong. It is generally believed that the flat-lying phase changes to the herringbone structure as films grow thicker¹⁸.

Regarding in particular the organization of pentacene and sexithiophene on Au(111) single crystal surfaces, scientists agree on the flat-lying adsorption of the first monolayer¹⁴. The adsorption of lying-down aromatic molecules on nonreactive metal surfaces is usually believed to be of van-der-Waals origin, in particular, due to polarization of π -electron density on the molecule and surface electron density of the metal.

There have been reports on flat adsorbed 6T on thermal silicon oxide that undergo a transition into the standing phase when one monolayer coverage is reached [¹⁹]. Figure 2.2.3 shows a schematic representation of the orientational transition. Instead on native silicon oxide the same group did not find flat lying molecules. This was attributed to a strong molecular interaction between the OH groups and the 6T.

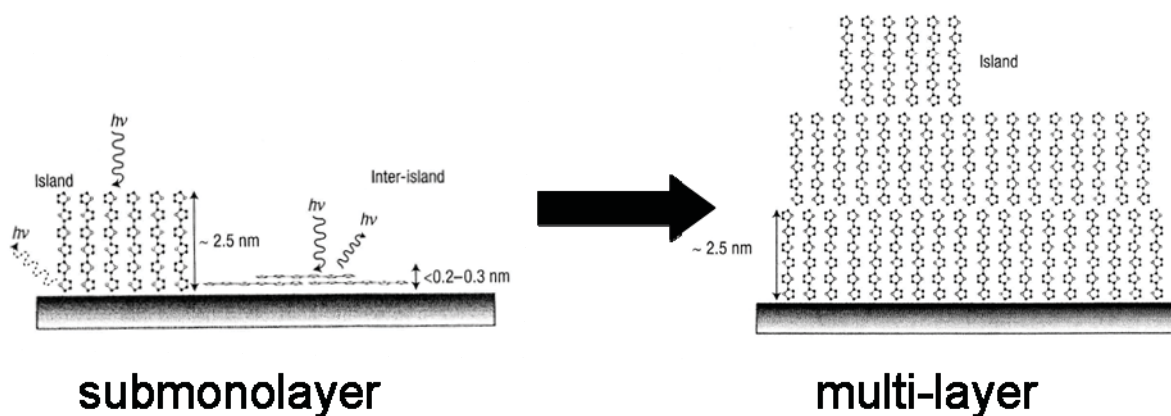


Figure 2.2.3: Schematic representation of the orientational transition of 6T on silicon oxide when increasing the thickness over one monolayer[Courtesy of E. Da Como].

Standing adsorption has further been observed on organic wetting layers and inert substrates.

However the adsorption of organic molecules on metal substrates is a well-studied subject, there are to date many publications that are in evident contradiction.

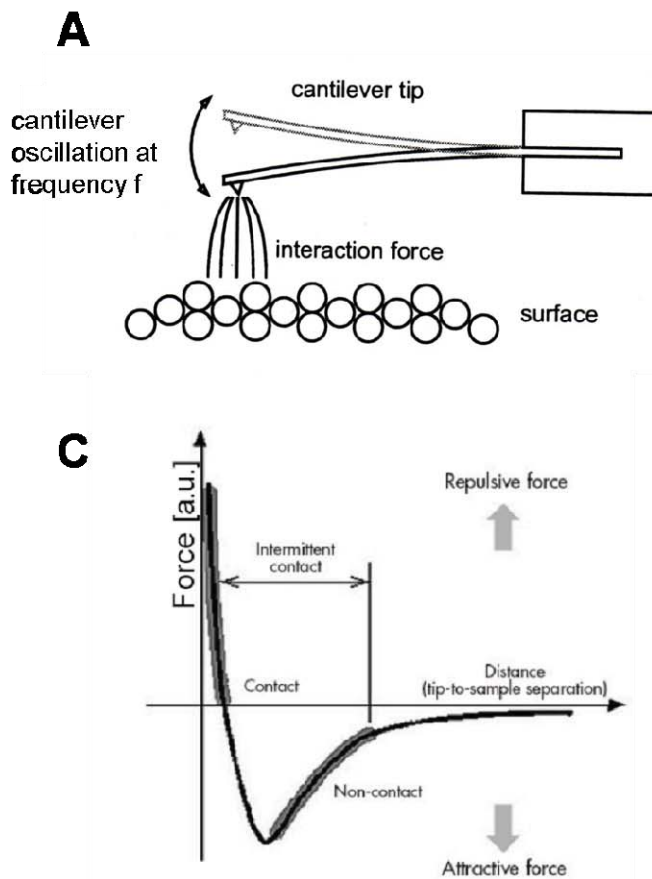
In a recent study (2007) complementary techniques (UPS, NEXAFS, STM, AFM) were used to compare the adsorption of pentacene on gold and silver substrates. Their conclusion brings earlier controversial results on a common point of view, stating that pentacene exhibits a coexistence of both an all flat-lying phase and a standing thin-film phase that nucleates on a first flat-lying wetting layer²⁰.

2.3. Scanning Probe Microscopy techniques

In this subchapter a brief introduction into the fundamentals of the Scanning Probe Microscopy (SPM) techniques employed in the present study is given, namely Non-contact Atomic Force Microscopy (NC-AFM) and Scanning Tunneling Microscopy (STM).

2.3.1. Non-contact AFM

In NC-AFM an at a frequency f oscillating cantilever is scanned across a surface at a close distance tracing the surface contour (Figure 2.3.1A) . Interatomic forces repel the tip which is mounted to a flexible cantilever. In NC-AFM the feedback signal is derived from the force induced shift in resonance frequency of the vibrating cantilever. The resulting deflection of the cantilever can in turn be used to produce an image of the surface by generating lines of equal resonance frequency shift. The deflection of the cantilever is measured by detecting the deflection of a laser beam reflected from the coated back of the cantilever onto position sensitive photodiode detector (PSD).The technique becomes very sensitive in UHV due to high Q-values. The formulas for the minimal detectable force gradient and the resonance frequency shift are shown in Figure 2.3.1B. The force that induces the shift in resonance frequency is the Van-der-Waals force typically represented by a Lennard-Jones potential shown in Figure 2.3.1D together with labels for the corresponding AFM modes.



B NC-AFM feedback signal is derived from the force induced shift in resonance frequency of the vibrating cantilever

$$\frac{\Delta f}{f} = \sqrt{1 + \frac{1}{C} \cdot \frac{\partial F}{\partial z}} - 1 \approx \frac{1}{2C} \cdot \frac{\partial F}{\partial z}$$

NC-AFM is particularly interesting for vacuum due to the high Q-value of the resonator.

The minimal detectable force gradient is:

$$F'_{\min} = \left. \frac{\partial F}{\partial z} \right|_{\min} = \sqrt{\frac{4 \cdot C \cdot kT \cdot B}{2\pi \cdot f_0 \cdot Q \cdot A^2}}$$

C = cantilever spring constant

kT = thermal energy

B = FM detector bandwidth (≈ 2 kHz)

f_0 = cantilever resonance frequency

Q = cantilever Q-value

A = cantilever vibration amplitude.

Figure 2.3.1: (A) Schematic representation of the NC-AFM technique with an at a fixed frequency driven cantilever oscillation. (B) The shift in resonance frequency Δf of the vibrating cantilever is used as feedback signal and the minimum detectable force can be calculated. (C) Lennard Jones potential of the van der Waals forces with respective AFM modes.

2.3.2. Scanning tunnelling microscopy

STM was invented in 1982 [21, 22] by later Nobel Prize awarded Binnig and Rohrer and is the oldest member of the family of scanning probe microscopies.

Figure 2.3.2 shows the basic operation principles of an ideally mono atomic tip apex, the tunnelling current amplifier and the piezo driven distance control system. The polarization of the tunnel junction by application of a tunnelling or gap voltage between tip and surface leads to a distance proportional tunnelling current from hundreds of nA down to few pA. The quantum mechanical exponential relationship between current and distance is at the base for its high sensibility and atomic resolution capability.

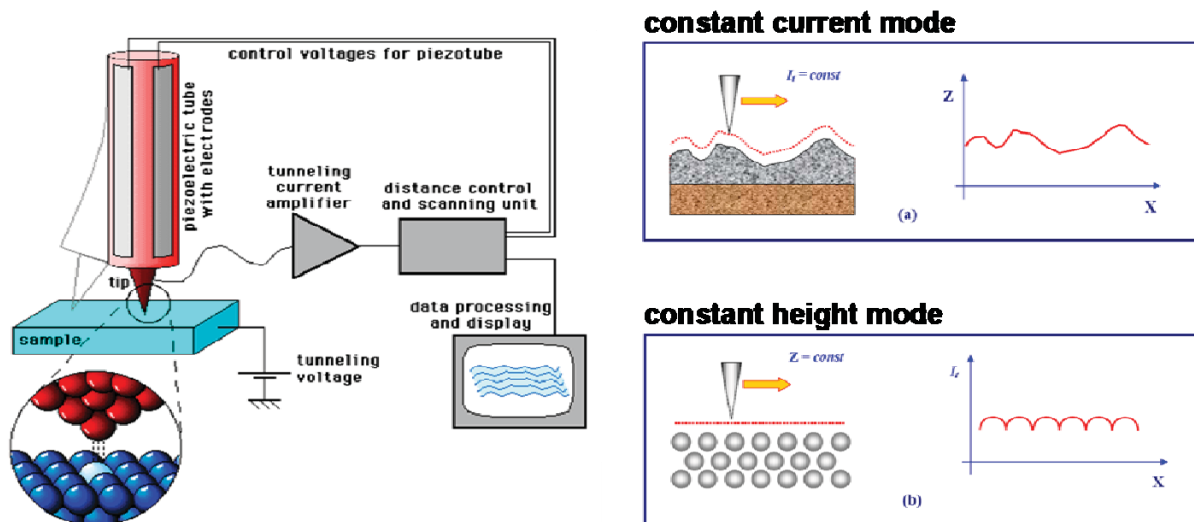


Figure 2.3.2: Operation principle of STM and the two STM modes constant current and constant height.

Figure 2.3.3A shows the unpolarized tunnel junction with empty tip and sample states above the Fermi energy E_F . No tunnel current is detected. When the tunnel junction is polarized like shown in Figure 2.3.3B a tunnelling current is possible at $V_{\text{Bias}} > 0$ when filled tip states tunnel into empty tip states. Varying the applied voltage we can access and visualize different tip and sample states.

Figure 2.3.3C is an example of opposite polarized tunnel junction that image different local charge densities unravelling the atomic structure. Figure 2.3.3D shows the quantum mechanical representation of a polarized tunnelling junction with transmitted and reflected waves. In theoretical physics this quantum mechanical problem can be solved using the WKB approximation.

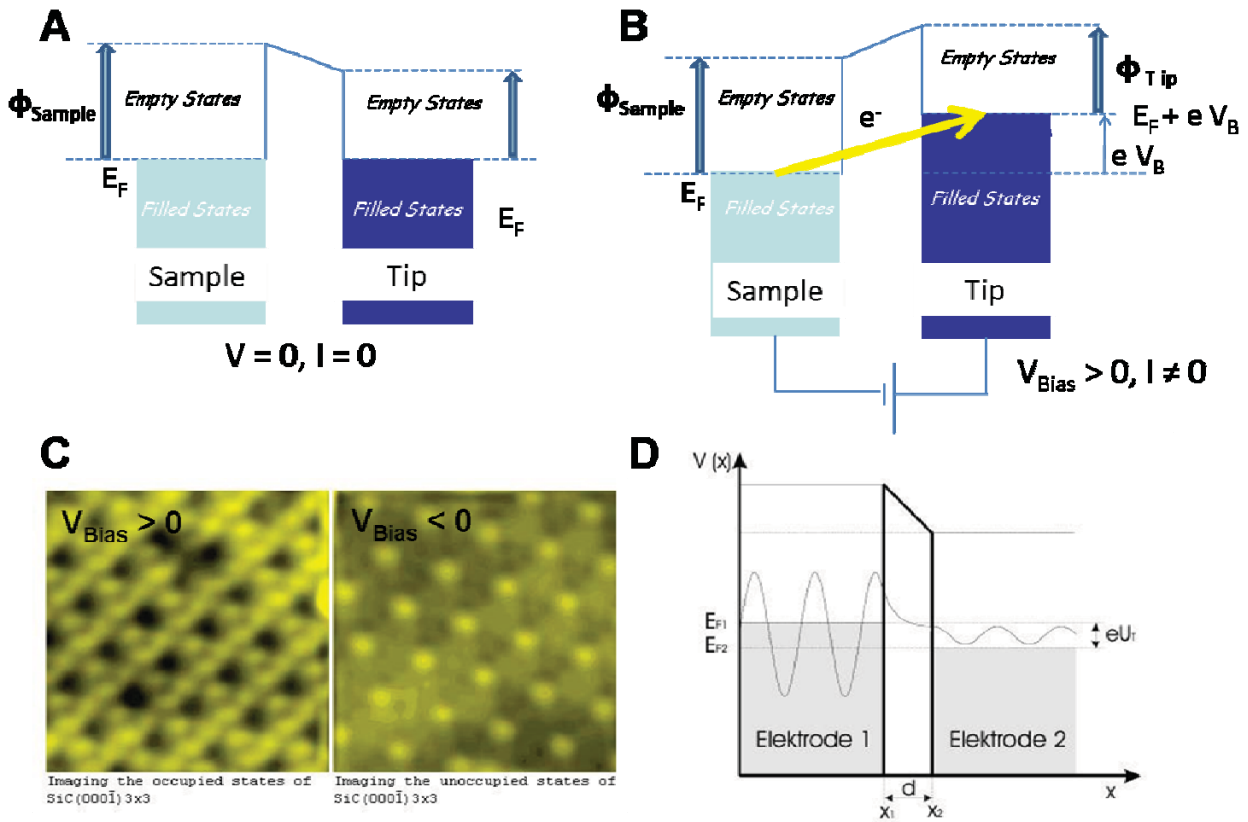


Figure 2.3.3: (A) Energy diagram of the not polarized tunnel junction. (B) $V_{\text{Bias}} > 0$ polarized tunnel junction. Filled sample states tunnel into the empty tip states. (C) Example for opposite polarized tunnel junctions that image different types of molecular orbitals. (D) Schematic representation of the tunnelling junction with applied bias. The electron wave can tunnel through the potential barrier.

3. Materials and experimental setup

3.1. Molecules

All studies in this thesis focus on three different types of organic semiconductor molecules, all deposited by vacuum sublimation, namely Sexithiophene (also known as sexithienyl or 6T), Pentacene (P5) and Perylene (PDI8CN2).

Sexithiophene is a well-known and extensively studied first generation rigid rod organic semiconductor. However the 6T charge mobility in organic devices is intrinsically limited, it is still an excellent rigid rod model system that is exemplary for a series of rodlike conjugated organic semiconductors. In particular, from comparison with previously published material and our new experimental in-situ technique it is possible to unravel basic dynamic growth phenomena of layered materials.

The 6T model system was employed both for AFM / STM calibration and verification of the expected adsorption orientation on dielectric and metal substrates in our system. Further detailed quasi real-time growth measurements at variable temperature from submonolayer to several MLs coverage allow to gain a deeper understanding of nucleation and interlayer transfer of molecules and relevant adsorption, redesorption and interlayer transfer energies (Ehrlich Schwoebel barrier).

3.1.1. Sexithiophene 6T

Sexithiophene also known as α -hexathiophene, α -hexathiényl or α -sexithiényl has the chemical formula $C_{24}H_{14}S_6$. and a melting temperature of 290°C at normal condition. It belongs to the class of p-type organic semiconductors. Its crystalline structure in the solid state is characterized by the occurrence of a low temperature (LT) and a high temperature (HT) polymorph named after their preparation method [23]. Both have a monoclinic unit cell but with $Z=4$ (LT, bcc) and $Z=2$ (HT, sc) molecules per unit cell. The in Figure 3.1.2 represented LT phase is most studied and experimentally easier to obtain. The LT crystal unit cell parameters like shown in Figure 3.1.2 are $a = 44.708 \text{ \AA}$, $b = 7.851 \text{ \AA}$, $c = 6.029 \text{ \AA}$ with an angle between a and b of 90.76° and an angle of 23.5° between a and the long molecular axis determined by x-ray measurements [24].

More generally speaking 6T belongs to the class of oligothiophenes: conjugated organic molecules of different chainlength with a five membered sulphur containing aromatic compound as smallest unit (see Figure 3.1.1). Oligomers of this monomer unit bonded by σ bonds via its α -carbons are termed α -nT where n stands for the number of subunits of the respective oligothiophene.

Thiophene rings have various energetically close gas phase conformations that differ by a 180° torsion angle between the neighboring subunits. If all sulphur atoms are on the same side the conformation is termed all-cis whether an alternating conformation is called all-trans. When the molecules adsorb at a gas/solid interface, carbon and sulphur atoms are involved in the surface bonding and therefore the nature of the substrate together with the intermolecular interactions crucially determine the orientation of the seeding monolayers. Both at gold step edges and in charge transfer complexes, the intrinsic rotational degrees of freedom of 6T in the gas phase have been shown to translate into various types of adsorbed 6T rotamers on solid substrates (REF Jaeckel, FB+FZ, Koch). For flat adsorbing 6T (molecular axis parallel to the surface) this rotameric flexibility enables the single molecules to perfectly trace a surface step edge of arbitrary shape. In the case of charge transfer complexes the intermolecular interactions between donor and acceptor species are made responsible for the conformational change in 6T as for example so-called "banana-shaped" (all-cis) molecules have to our knowledge never been found on pure 6T submonolayers far from step edges.

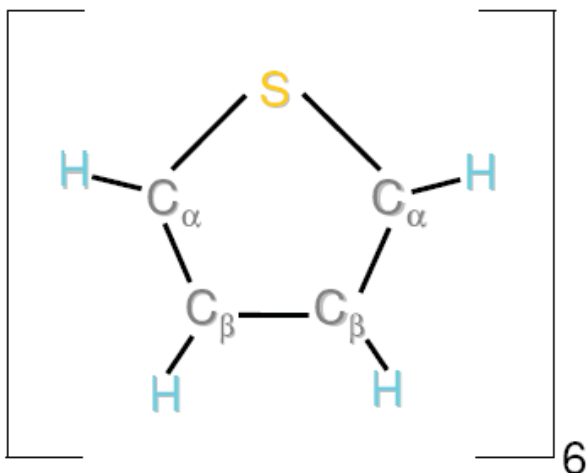


Figure 3.1.1: Thiophene monomer with the atomic nomenclature for the carbon atoms. Sexithiophene consists of six conjugated rings. The alternative name α -6T underlines the linking of the monomer subunits through the C_α atoms.

In the solid state and thin films 6T molecules are almost planar, belong to the point group symmetry C_{2h} and crystallize usually in a herringbone structure. This molecular organization within a 6T crystal is common to planar molecules and shown in Figure 3.1.2 with respective unit cell and dimension. The herringbone packing structure is characterized by all molecules having the same overall orientation with their long molecular axes being parallel to each other while adjacent 6T molecules are tilted by an angle of 65° with respect to one another in an “edge on plane” configuration. It was shown that orientational disorders of the herringbone lattice strongly affect the optical and electronic properties of the 6T crystal quenching the optical signal and breaking the π electron system ^[25]^[26]. A good control of the arrangement of the molecules not only at the interface means therefore controlling their mutual distance and thus their interactions (exchange integral).

We introduced here the bulk herringbone crystal phase that differs substantially from the so-called thin film phase that is dependent on the growth parameters and early studies by Servet et al. have shown the presence of polymorphism ^[27] with cell parameters different from those of the single crystal. Moulin et al. have studied the crystalline structures of ultrathin film by means of synchrotrone light. They show a change in the molecular packing as a function of the film thickness starting from a monolayer film. The structure is slightly different with respect to that of the crystal, confirming the existence of thin film phases ^[28].

Unlike the bulk phase, the thin film phase depends crucially on the underlying substrate but is technologically more relevant. On crystalline metal surfaces 6T adsorbs in a so-called flat lying orientation with its long molecular axis parallel to the surface, at least in the first overlayer that however acts as a template for further growth to a certain extent depending on the selected deposition parameters. On dielectric surfaces (like e.g. silicon oxide, indium tin oxide (ITO) and others) the 6T molecules adsorb in a so-called standing orientation with its long molecular axis perpendicular or close to perpendicular to the surface. However depending also on the substrate roughness, the growth parameters and the number of monolayers the question on the molecular orientation can get quite complex. For example on submonolayer 6T films on thermal silicon oxide (t-SiO_x) 6T has been found to assume an initially flat lying configuration and to undergo a change in orientation throughout the deposition of further monolayers. On the crystalline Au (111) surface in contrary an orientational transition from flat lying to upright standing 6T molecules has been found already starting from the second monolayer. We will discuss the particularities of molecular orientation and the respective thin film phase together with the presented results in Chapter 4.

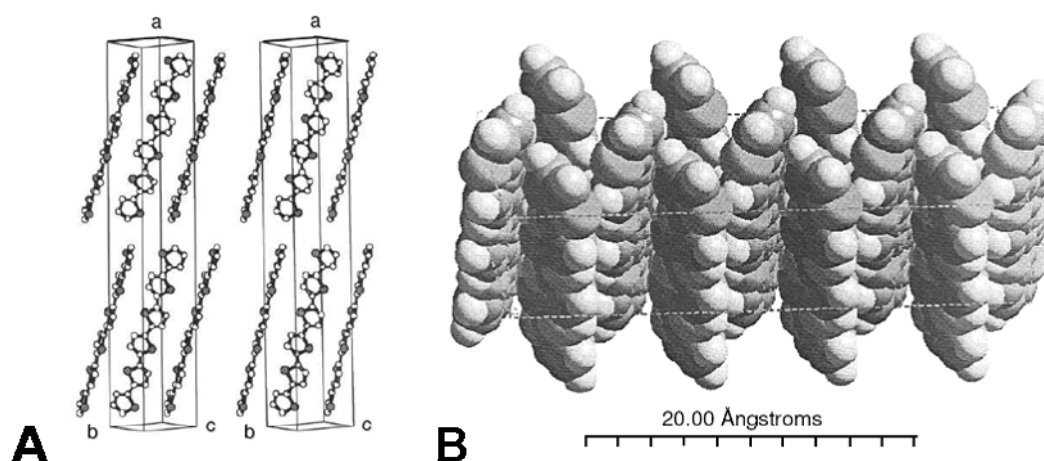


Figure 3.1.2: (A) The herringbone packing structure of 6T (LT) with its unit cell as inferred from X-ray diffraction measurements [29]. (B) Space filling sketch of the 6T herringbone packing [30].

Apart the above named exceptions and the bulk organic crystal structure, 6T is most frequently found to adsorb in the all-trans conformation on homogeneous and flat surfaces. The all-trans conformation is shown in Figure 3.1.3 together with its dimensions calculated from a space-filling model. The particular structure of the alternating all-trans molecular conformation gives rise to left and right handed chiral domains depending on how the molecules adsorb onto the surface.

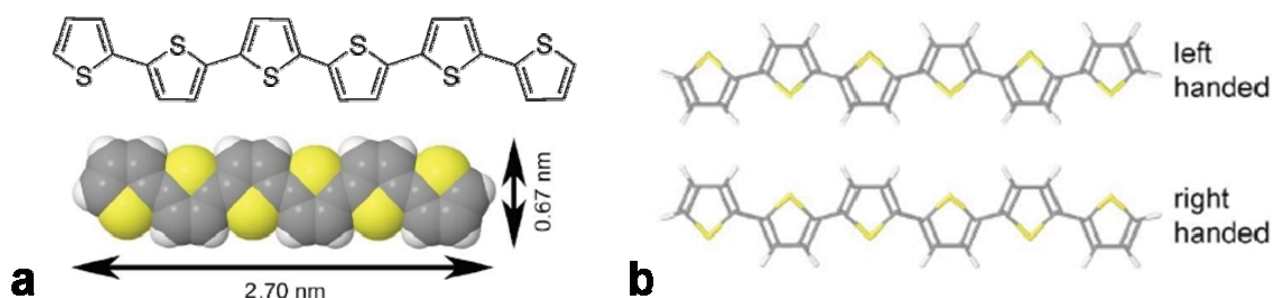


Figure 3.1.3: (a) Sketch of an all-trans conformation of a single 6T molecule and respective dimensions in a space-filling (or calotte) model. (b) If adsorbed flat onto a surface the all-trans conformation gives rise to domains of different chirality – here termed left and right handed.

In molecular assemblies finding a suitable balance between the surface bonding mechanism and the intermolecular bonding is the key to obtain the desired orientation of the seeding monolayers and the formation of long range ordered multilayers. As we explained in Chapter 2, high molecular order is crucial for the formation of delocalized π -orbitals and hence energy bands that allow for charge transport in organic devices. However most studies on the molecular organization of 6T consider almost exclusively ideal crystalline metallic substrates that provide considerable covalent interactions [31], and act as template for the lateral ordering (at least in the monolayer regime). Specifically on Au, Cu, Ni and Ag single crystals surfaces 6T tends to adsorb in a coplanar geometry, that is with the aromatic rings parallel to the surface. This general feature of π bonding of aromatic molecules to metallic surfaces is also called π stabilization and can be experimentally identified by peak shifts of the π orbital features in photoemission. The sulphur electrons have been shown to play no important role in the surface bonding on Ag(111) [32]. However chemical interactions and other bonding mechanisms are still under debate even for submonolayer films on ideal surfaces (e.g. theory and experiment on bonding mechanisms (π bonding vs electrostatic interactions) in 6T/Au(110) are to date in disagreement [33] [34]). Multilayer systems on technological and far from ideal metallic surfaces such as polycrystalline Au and native or thermal Silicon oxide must be understood in order to improve device performance. Further there is an particular interest in understanding the film formation dynamics and determine the role of the template effect of the first overlayer which has been shown to extend up to five monolayers in the 6T/Au(110) system [35].

Therefore in this work the main focus is on submonolayer and ultrathin films (< 3ML) on different technologically relevant substrates that are often far from ideal single crystal surfaces. Beyond the first overlayer a screening effect is expected with growing film thickness as molecule-surface interactions become less relevant and in-plane intermolecular forces and interactions between two adjacent monolayers prevail. However also the altered surface energy beyond the first overlayer is supposed to change surface diffusion and aggregation dynamics of subsequently beam deposited molecules.

The electronic structure of the π orbitals of 6T that play an important role in surface chemical bonding consist in a pair (bonding and antibonding) of localized and delocalized molecular orbitals for each thiophene ring while the valence orbitals develop gradually from molecular orbitals into broad bands in the large length limit [36]. In Figure 3.1.4 the aromatic and quinoid orbitals that are dictated by the particular pattern of the double and single carbon bonds are depicted. When the carbon double bonds connect C_α and C_β , the molecule gets an aromatic character and the π electron system extends between the thiophene rings. When the sulphur orbital participates in the molecular orbital, it remains separate from the delocalized carbon bonds and the electrons are localized to one thiophene unit (quinoid).

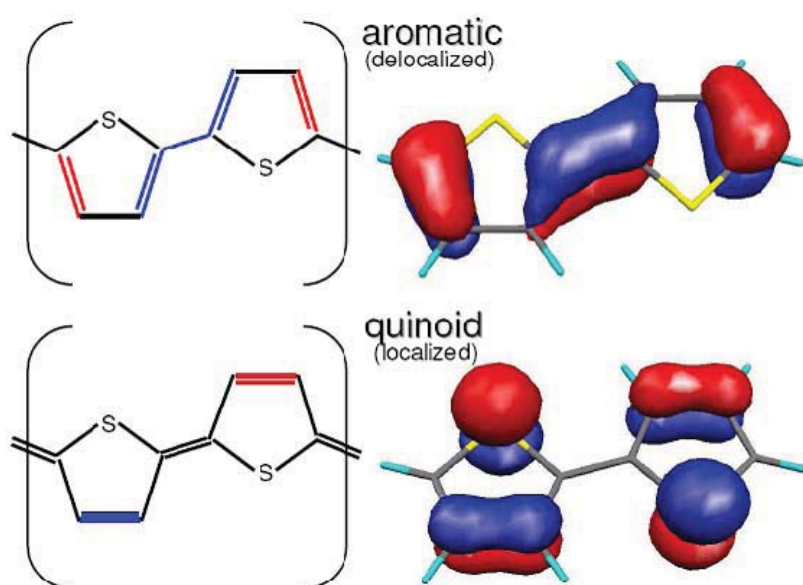


Figure 3.1.4: Two types of molecular orbitals for thiophenes where a participation of the sulphur orbitals breaks the π delocalization [37].

The electronic gap between the highest occupied molecular orbital (HOMO) and the lowest unoccupied molecular orbital (LUMO) was experimentally determined to $E_{\text{gap}} \sim 2.3 \text{ eV}$ [38].

3.1.2. Pentacene

Pentacene (P5)

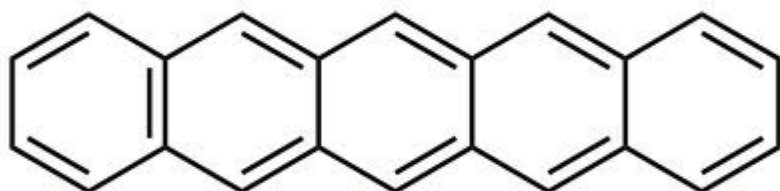


Figure 3.1.5: Sketch of the 5 units long polyacen pentacene P5.

3.1.3. Perylene PDI8CN2

Perylene is a new generation n-type semiconductor with a rigid core in contrast to the rodlike shape of Sexithiophene and Pentacene.

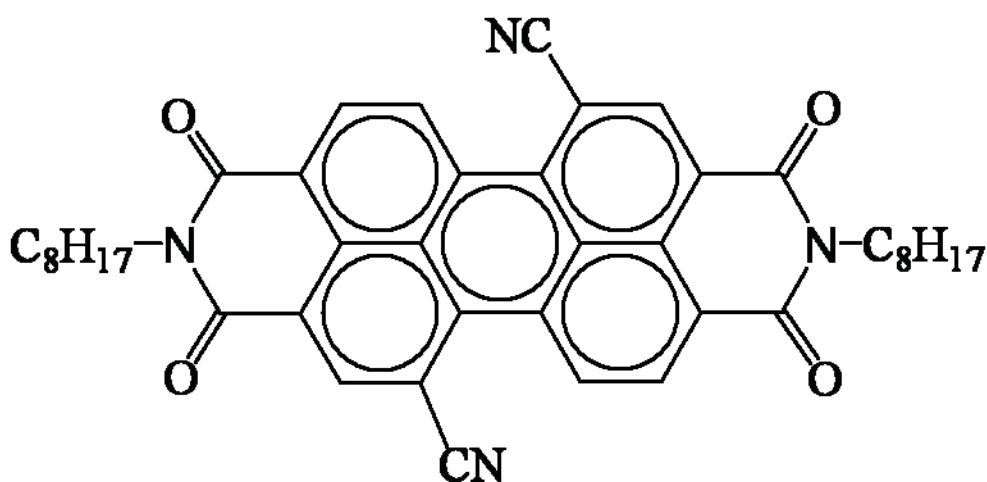


Figure 3.1.6: Sketch of the molecule Perylene PDI8CN2. The circles inside the five core hexagons indicate conjugated bonds with delocalized π orbitals.

3.2. Substrates and preparation techniques

In the following the different substrates that have been used in this work are introduced in detail. Further their role in the frame of advanced SPM studies on growth of organic semiconductors is discussed and references to the experimental section of this work are given.

3.2.1. Graphite (HOPG)

Highly oriented pyrolytic graphite (HOPG) is a layered polycrystalline material that consists of sheets of sp² hybridised graphene layers that are held together by weak van der Waals forces. The micrometer size crystalline grains exhibit a high degree of preferred crystallographic orientation of the c-axes perpendicular to the surface (0001) what confers HOPG similar physical properties to a graphite crystal.

The covalently bound carbon atoms within a single graphene layer arrange in a hexagonal lattice with a side length of 1.42 Å while adjacent layers are stacked in a ABAB fashion at an interlayer distance of $c/2 = 3.35$ Å. This alternate stacking gives rise to A-site and B-site carbon atoms. A-site carbons lie directly above each other in adjacent layers while B-site atoms sit over a void or better the center of a hexagon of the neighboring layers.

HOPG is an excellent substrate for scanning probe microscopy as substrate or calibration standard at atomic levels of resolution that is chemically inert and easily renewable by cleaving off some graphene layers with an adhesive tape.

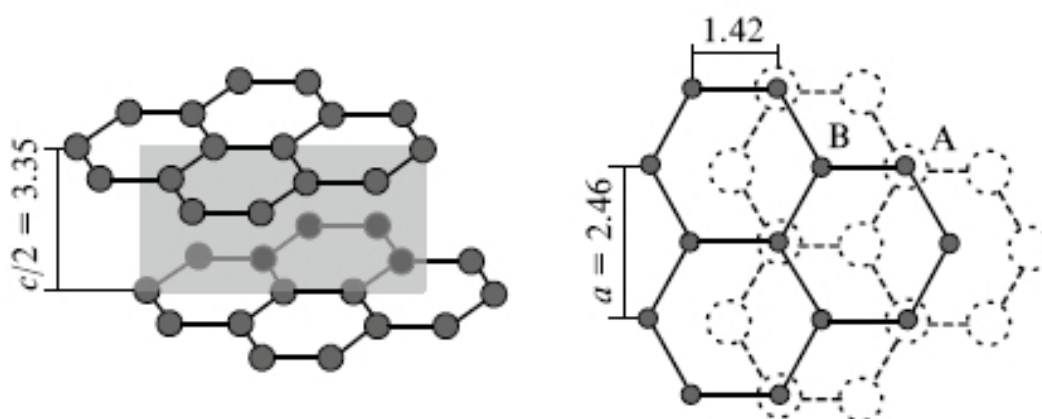


Figure 3.2.1: Schematic representation of the bulk hexagonal graphite crystal structure (ABAB stacking) with A-site and B-site carbon atoms and interatomic distances in Å.

In atomic resolution SPM images a honeycomb structure with 2.4 \AA spacing observed that originates from the imaging of only B-site atoms is usually observed.

As it can be seen in Figure 3.2.2 we observed a hexagonal structure with an average side length of $1.43 \pm 0.1 \text{ \AA}$ as extracted from the profiles along the two marked directions. This value is in excellent agreement with the hexagonal graphite crystal structure shown in Figure 3.2.1. We deduct that in our case we were able not only to image both A-site and B-site atoms but also the atoms in the center of the hexagonal structure. These carbon atoms can be identified as B-site atoms from the underlying graphene sheet and explain the reduced spacing.

The HOPG sample has been used for calibration and testing of the tip quality prior to measuring the more complex organic adsorbates on different substrates.

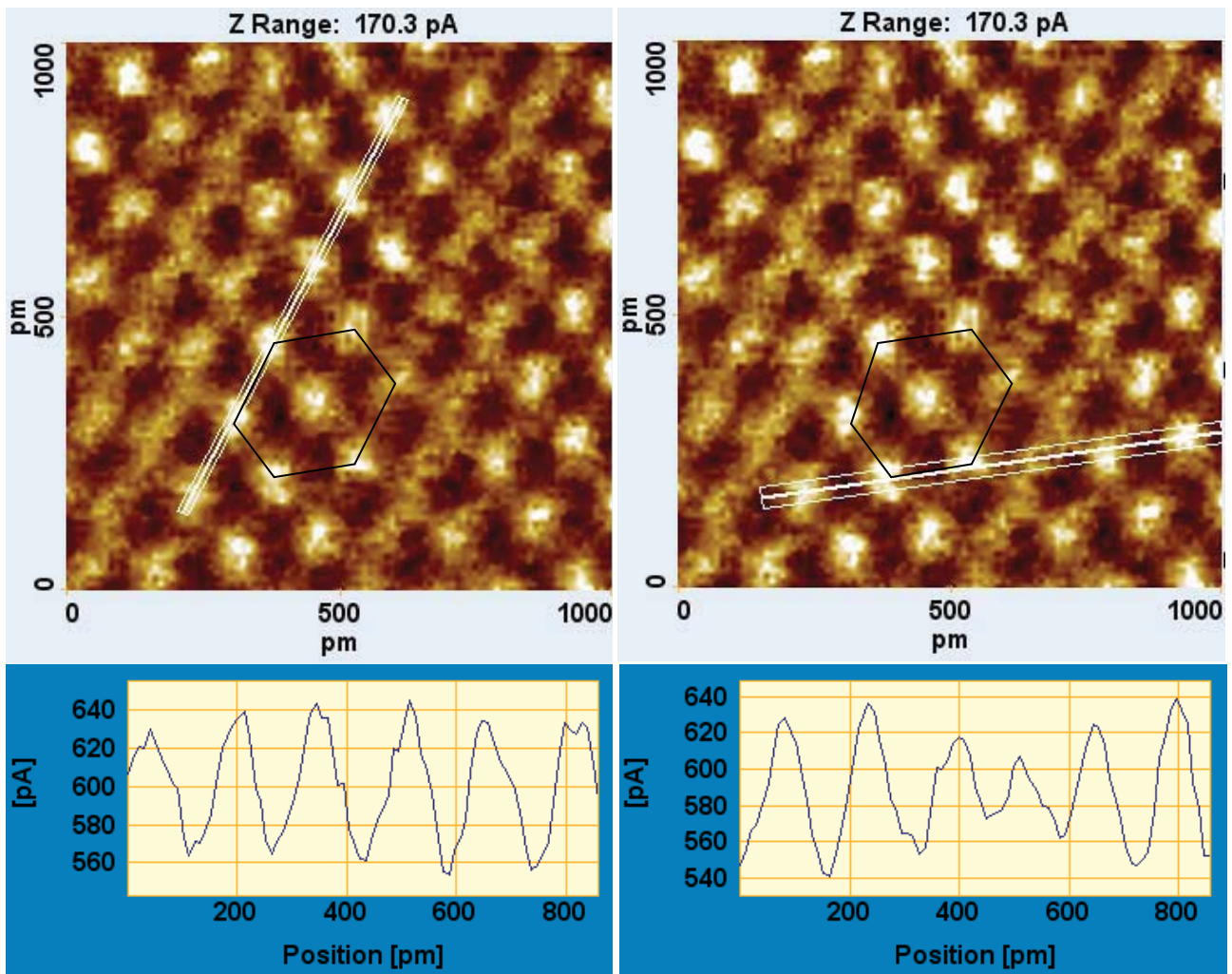


Figure 3.2.2: STM current image (0.35V, 0.5nA) of the first 2 hexagonal graphite surface layers at room temperature and respective profiles along two directions. In both cases the average distance is $1.43 \pm 0.1 \text{ \AA}$.

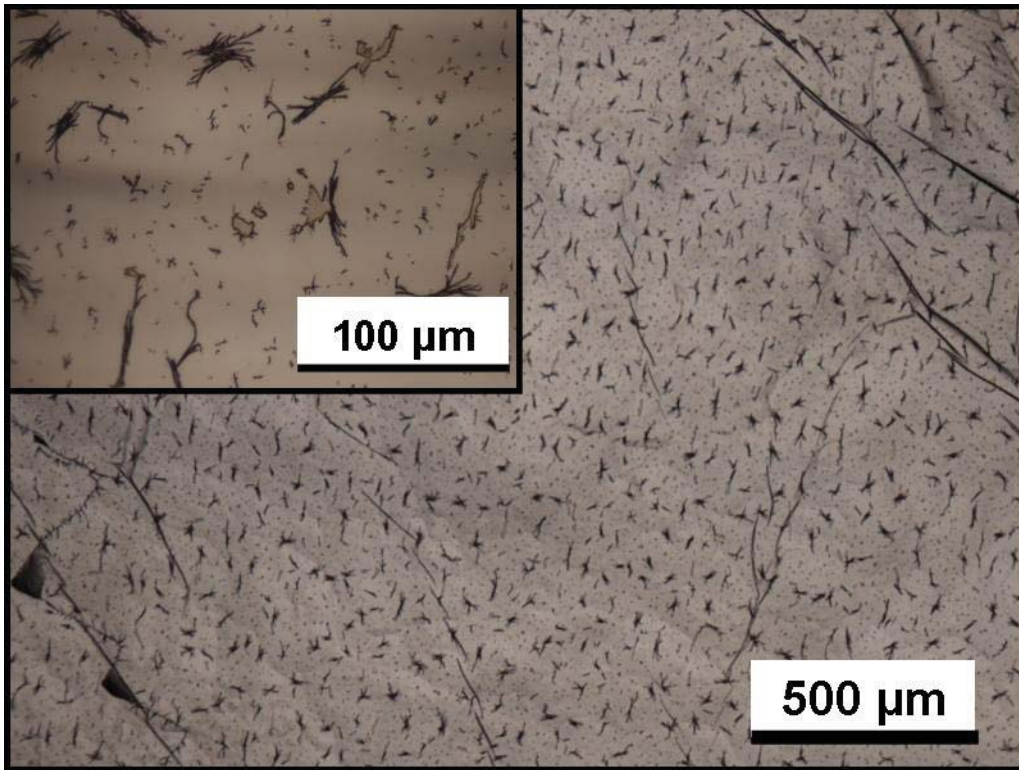


Figure 3.2.3: Optical micrographs of the needle-like crystallites that grow on HOPG after about 100nm thickness.

3.2.2. Native silicon oxide (Si/SiO_x 2 nm)

Silicon oxide is an amorphous material in which silicon binds four oxygens with a tetrahedral geometry. At the surface however two different kind of bonds are present: silanols (Si-OH) and siloxanes (Si-O-Si).

Native silicon oxide is further suitable for STM studies. The naturally forming oxide layer in contact with air is only about 2 nm thick and allows for tunnelling at low currents (pA) and high voltages (3 - 5V) into the doped semiconductor.

The imaging of the bare native silicon oxide by STM is highly reproducible and stable. However measuring a combined system of native silicon oxide and an organic semiconductor overlayer is much more tricky. Not only have organic semiconductors been designed to have a π orbital delocalization parallel to the surface as they adsorb in a standing configuration on silicon oxide. Therefore charge injection and transport is best parallel to the surface and not orthogonal like it would be best for STM. Furthermore the extreme scan parameters for weakly adsorbed adlayers lead to desorption, scan-induced reorganization and effects like physical penetration of the tip into the organic film and attachment of molecules to the tip. However adjusting the voltage and current parameters we were able image 6T on native silicon oxide in different configurations. If the sample is prepared in UHV, the possibility to thin out the native oxide by heating (800°C) allows to lower the scan parameters and be therefore less invasive.(REF OEHZELT). However as the oxide thins below 2 nm, the semiconductor properties of the underlying silicon become more influential during the aggregation of the adlayer. In fact it was shown that the reactive crystalline Si surface in UHV leads to a breakup of the molecule upon adsorption [³⁹].

3.2.3. Gold single crystal – Au(111)

Figure 3.2.4A shows flat Au(111) terraces on a single crystal prepared by flame annealing. Figure 3.2.4B shows a magnification that already reveals the herringbone structure. Figure 3.2.4C shows a high resolution STM image of the herringbone reconstruction. A further magnification reveals atomic resolution between two herringbones shown in Figure 3.2.4D.

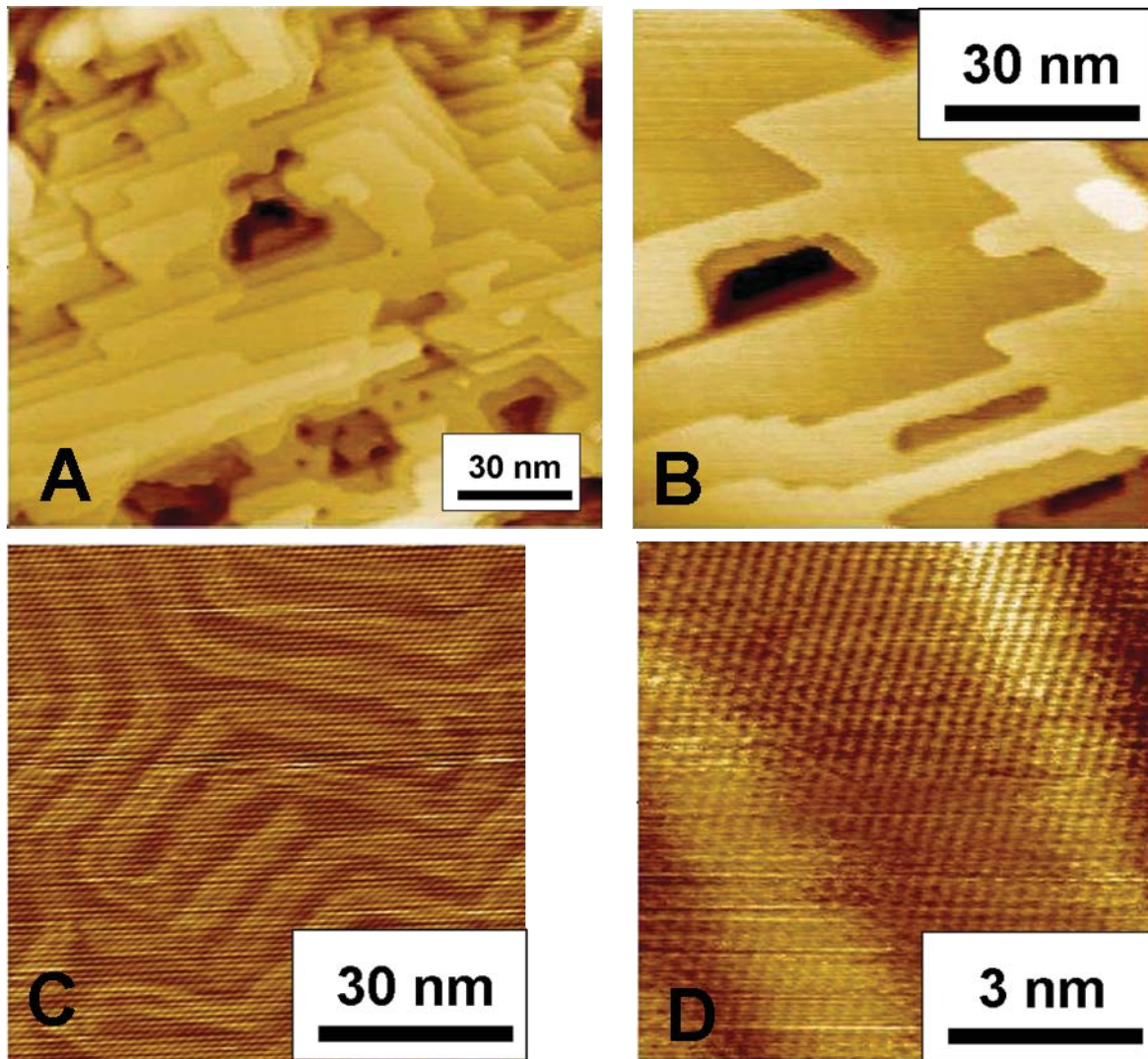


Figure 3.2.4: (A) Gold terraces on a flame-annealed single crystal sample. (B) Herringbone structure emerges on the terraces. (C) In a sample region without terraces the Herringbone structure is resolved better. (D) Atomic resolution on Au (111) with Herringbone reconstruction.

3.2.4. Polycrystalline Au

Polycrystalline gold surfaces usually have a grain-like morphology depending on the employed vacuum evaporation technique. The use of primers to promote the adhesion of gold is wide spread in device applications using thermal SiO_x as dielectric material while on the technologically less relevant mica crystalline gold terraces similar to single crystals have been produced.

We used here about 250 nm thick commercial gold films (Arrandee, Germany) evaporated on borosilicate glass with a 2.5 nm thick chromium layer as primer as shown in Figure 3.2.5. In the same figure, four NC-AFM micrographs of different length scales confirm the grain-like structure with grain sizes ranging from 20 – 100nm. The surface roughness determined by AFM for a $1\mu\text{m}^2$ is 3.2 nm. However, as we see in Figure 3.2.5 NC-AFM cannot resolve the surface structure of the grains.

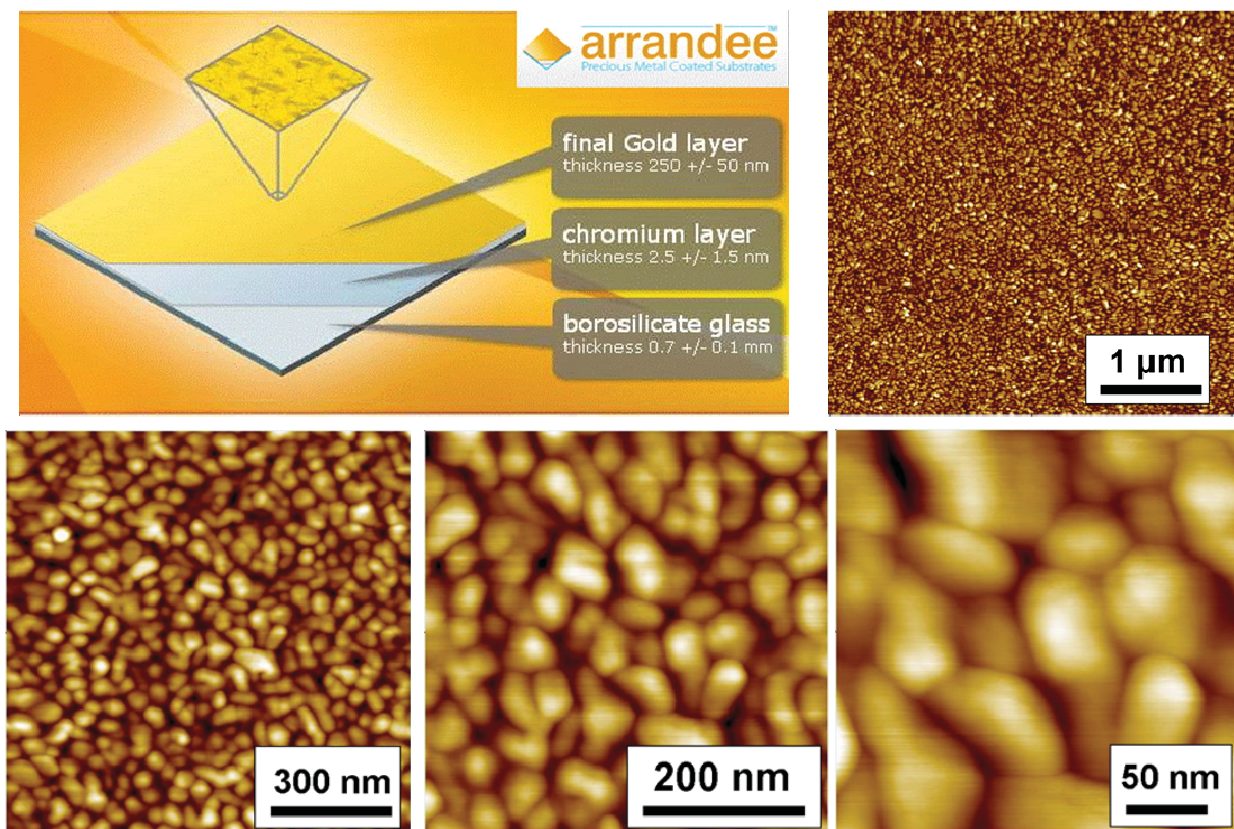


Figure 3.2.5: Arrandee polycrystalline gold substrates as characterized by UHV NC-AFM.

STM on flat grains of untreated polycrystalline Au films reveals a multi terraced morphology with step heights ranging from 50 -160 nm like shown the profile section in Figure 3.2.6. However, the terraces are only few nanometers wide. In order to obtain larger flat Au terraces, the polycrystalline films can be flame annealed.

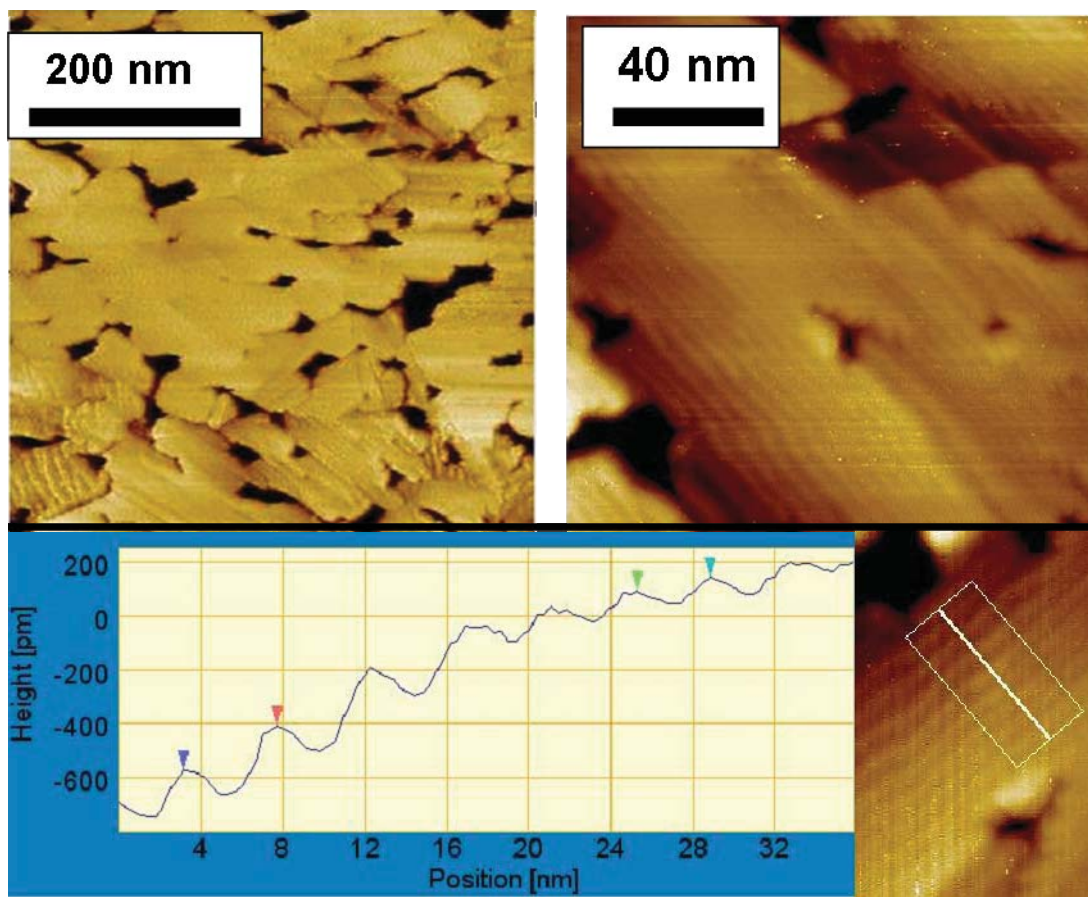


Figure 3.2.6: STM image (0.1V, 100pA) of the Arrandee polycrystalline gold substrates on flat grains and respective profile confirming the presence of terraces of 50-160 pm height.

Polycrystalline gold samples can be flame annealed using a propane gas flame. Herein the sample is passed slowly over a blue propane gas flame until the gold film starts to glow. With each passing over the flame the gold grains shown in Figure 3.2.5 melt and reorganize. Under optimized conditions several hundred nanometer large terraces of Au (111) can be obtained. Their height measured by STM is about 200 pm. The 120/60 degree step edges are typical of good Au(111) surfaces like shown for the two images of flame annealed Arrandee polycrystalline gold in Figure 3.2.7.

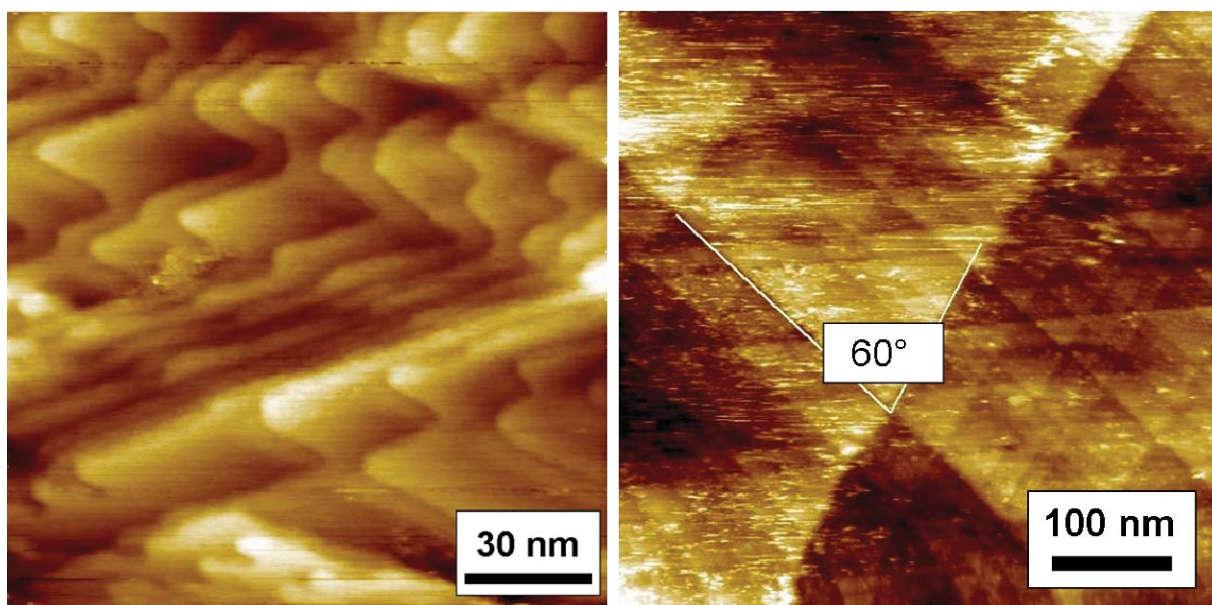


Figure 3.2.7: STM images of flame-annealed Arrandee polycrystalline Au films with flat terraces and triangular steps.

3.2.5. OFET testpattern structures

In the present work we have carried out in-situ real-time growth studies on two types of technological test pattern structures whose specifications are described in this subchapter together with reference and benchmark SPM measurements carried out with our setup.

Figure 3.2.8 shows the Fraunhofer-type OFET testpattern characteristics. In Figure 3.2.8A represents the entire circuit layout divided in four groups of four FET structures with channel width 2.5, 5, 10 and 20 μm . The first magnification shows a single FET with source and drain electrode while the second magnification depicts a optical microscope image of the interdigitated channel region. In between a cross section with the respective thicknesses of the layered structure is shown for a pentacene OFET. The surface morphology of the FET with 2.5 μm channel and respective profile are shown in Figure 3.2.8C. The measured thicknesses and distances are in good agreement with the manufacturer specifications given in Figure 3.2.8B along with other details.

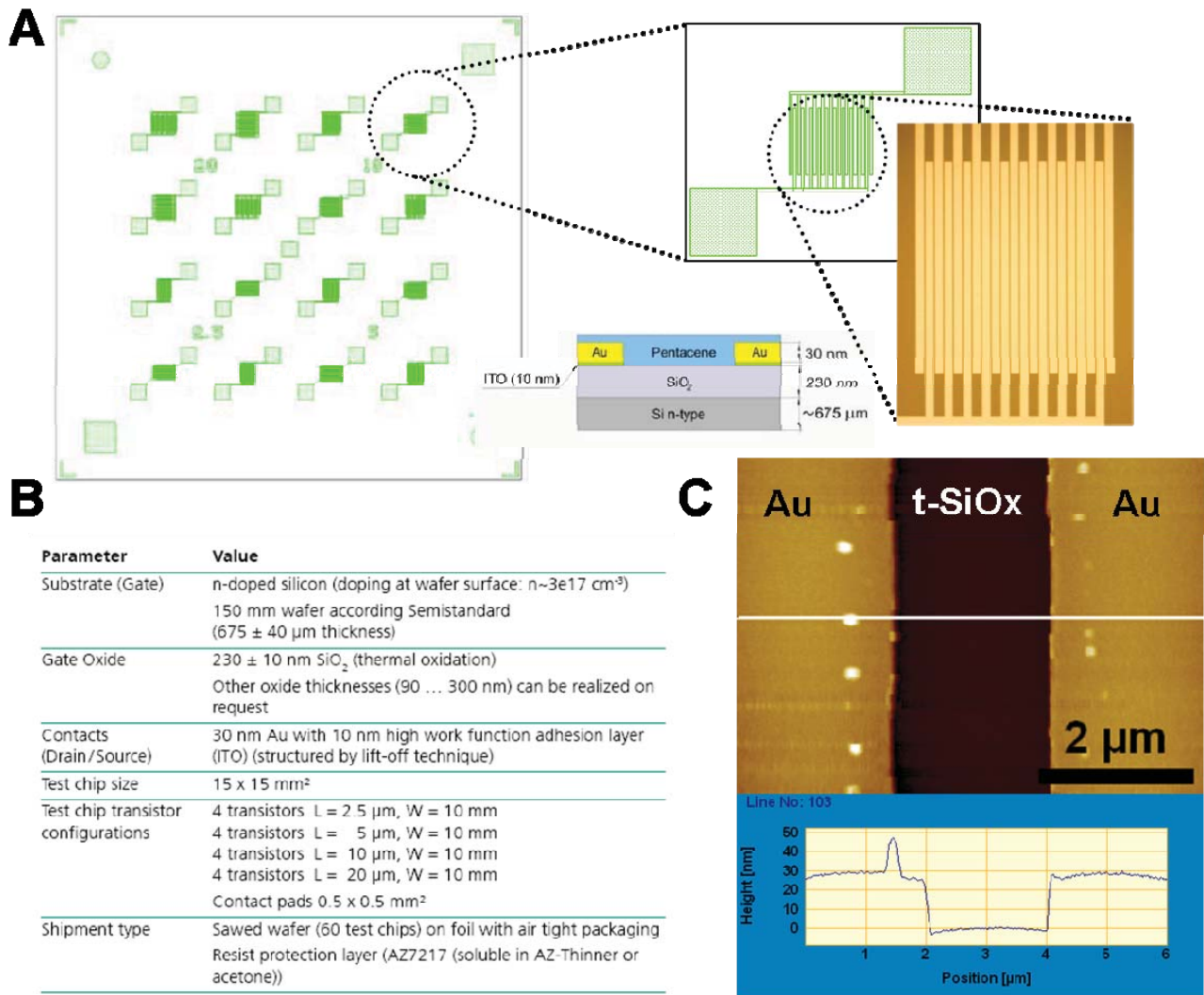


Figure 3.2.8: (A) Fraunhofer test pattern FET structures with channel lengths 2.5, 5, 10, 20 μm , magnifications and cross section scheme. (B) Testpattern details. (C) AFM image and respective profile.

The principal differences between the Fraunhofer-type(FH) and the Trento-type(T) are the thickness of the Au electrodes (FH: 30 nm, T: 150 nm, see Figure 3.2.9). Further the FH-type employs 10 nm of ITO as primer (or adhesive layer) that promotes the attachment of the gold whereas the T-type uses 3-5 nm of chromium.

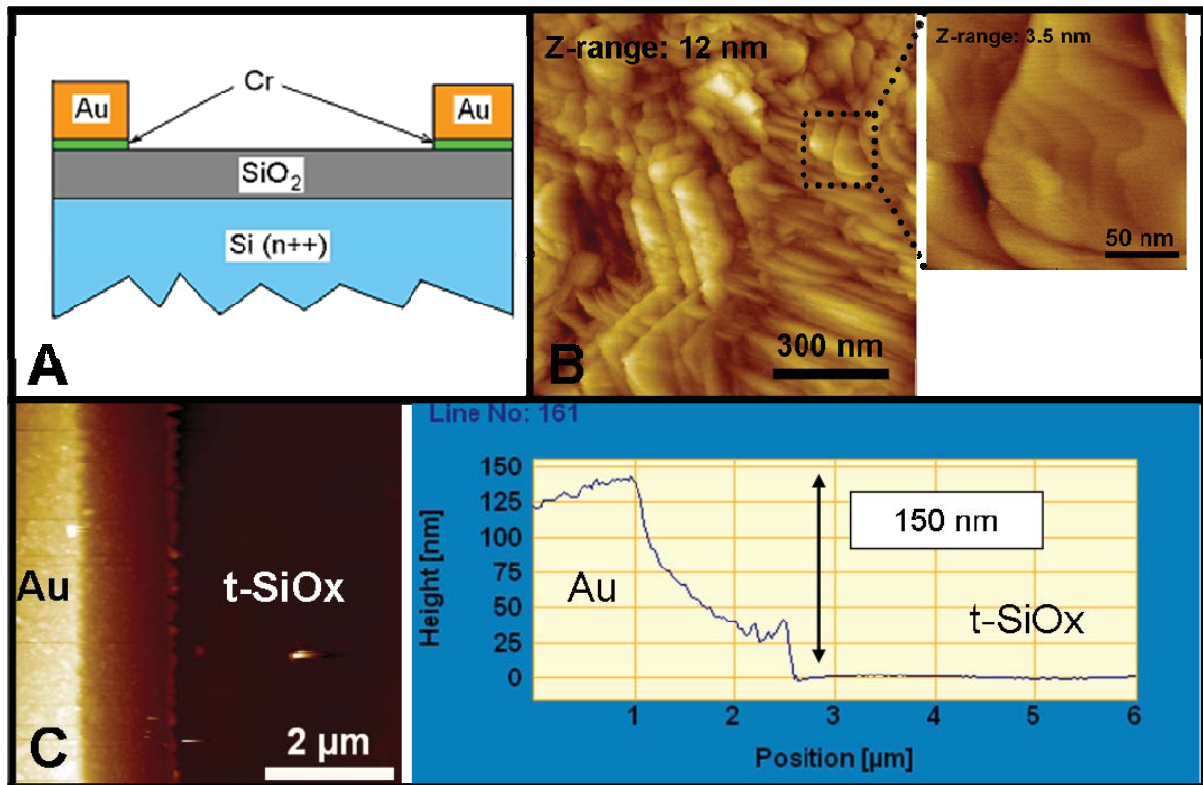


Figure 3.2.9: (A) Cross section of Trento type testpattern. (B) NC-AFM morphology of bare polycrystalline testpattern electrodes. (C) NC-AFM at Au/t-SiOx interface and respective profile.

Figure 3.2.9 summarizes the characteristics of the second type of testpattern used in this work, namely the Trento-type testpattern. The cross section in Figure 3.2.9A shows the use of an about 3-5 nm thick chrome layer to favour the adhesion of the shadow mask deposited gold electrodes and wires. From the AFM image in Figure 3.2.9C and the respective height profile we confirm the electrode height to about 150 nm. To notice is the always present second step of about 40 nm height that is related to the employed shadow mask deposition technique. Figure 3.2.9 shows the AFM morphology of the electrode surface. In the magnification gold terraces on flat grains of about 100 nm can be identified.

The Trento-type testpattern layout consists of 4 FET structures, two with a channel width of 40 μm and two with 20 μm, where transistors with the same channel width share a common source electrode. Figure 3.2.10 shows the Trento-type layout together with a magnification of the interdigitated channel and an AFM image of the thermal oxide structure in between the gold electrodes.

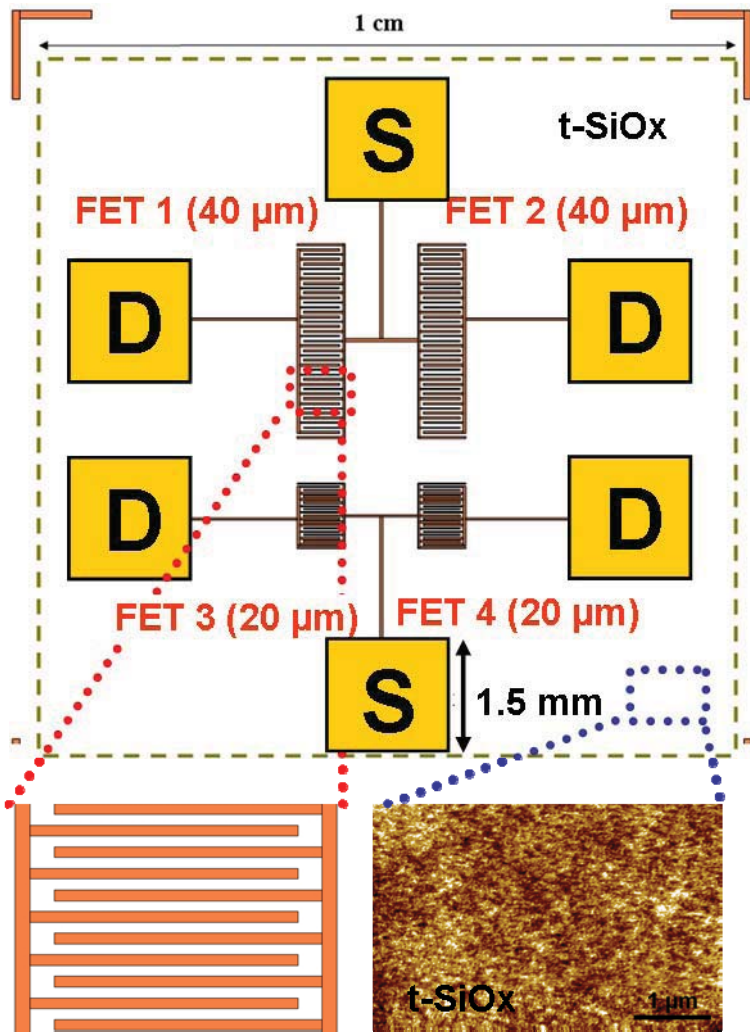


Figure 3.2.10: Trento-type test pattern layout with source (S) and drain (D) gold contacts and magnifications of the interdigitated electrode/channel structure and of the thermal SiOx.

3.3. Experimental setup

In this subchapter main components of the experimental setup are described. The whole system has been assembled, tested and continuously modified until the desired performance was achieved. The assembling and technical development of the experimental setup is considered a substantial outcome of the present PhD thesis. Therefore a particular focus is put on the custom-built improvements that have been developed ad hoc to improve the performance of the system. A further peculiarity of our experimental setup that will be discussed in detail is the addition of an in-situ organic material effusion (OME) cell in combination with the variable temperature UHV SPM system that provided new real space insight into quasi real-time growth phenomena.

3.3.1. UHV system overview

Many sophisticated experimental techniques with molecular or even atomic scale sensibility make use of an ultrahigh vacuum system in order to avoid interaction of molecules present in ambient air with the molecular scale sample structure under investigation. Measuring in UHV means that we have a base pressure of lower than 10^{-9} mbar that translates into a mean free path of a gas molecule of about 40km. These extreme conditions require special UHV compatible materials and devices, sequential pumping (scroll, turbo, ion, TSP), careful sample preparation and a lot of patience. In the following we will give a brief overview on the sequential pumping and some essential UHV strategies.

When setting up a UHV system from scratch like in the present case, a residual gas analyzer (RGA) is used to identify the molecules present in the vacuum system and lower the pressure accordingly step by step following a combination of strategies as there are multiple reasons why UHV is not reached. The last step is usually a so-called bake out of the UHV system at 120-140°C for several days during which the UHV improves as water and other molecules adsorbed to the inner walls of the system are gradually pumped out.

Figure 3.3.1 shows the UHV system during the bake out when it was still connected to the metal and organic growth system and mounted onto a rigid frame. For the bake out at 120°C heatable belts are coiled homogeneously around the UHV system whose power is controlled by a feedback loop to maintain the temperature constant. Three

thermocouples are distributed in key positions along the system and the temperature signal is fed into the feedback loop. The aluminium foil promotes a uniform temperature of the chamber walls as a thermal gradient will cause the molecules desorbed from the hot walls to stick to the coldest part of the system.

The sequential pumping is evidenced by white arrows. The high vacuum part (HV) consists of a scroll pump (also called roughing pump) that lowers the pressure from 10^3 mbar to about 10^{-2} mbar, a turbomolecular pump that is started at 10^{-2} mbar and brings the system to approximately 10^{-7} mbar. In order to further lower the pressure an ion pump is used that can be operated below 10^{-6} mbar. A combination of a titanium sublimation pump that sublimes titanium in defined time intervals into the chamber that coat the walls with a thin film of clean titanium. Since clean titanium is very reactive, residual gas molecules (that can be identified using the installed RGA) colliding with the coated chamber walls react and form a stable solid and the residual gas pressure is further reduced. Another employed technique to lower the vacuum is a cold trap that exploits the increased sticking coefficient of residual gas molecules on cold surfaces. Therefore a water or even liquid nitrogen cooled cold trap also further reduces the residual gas pressure.

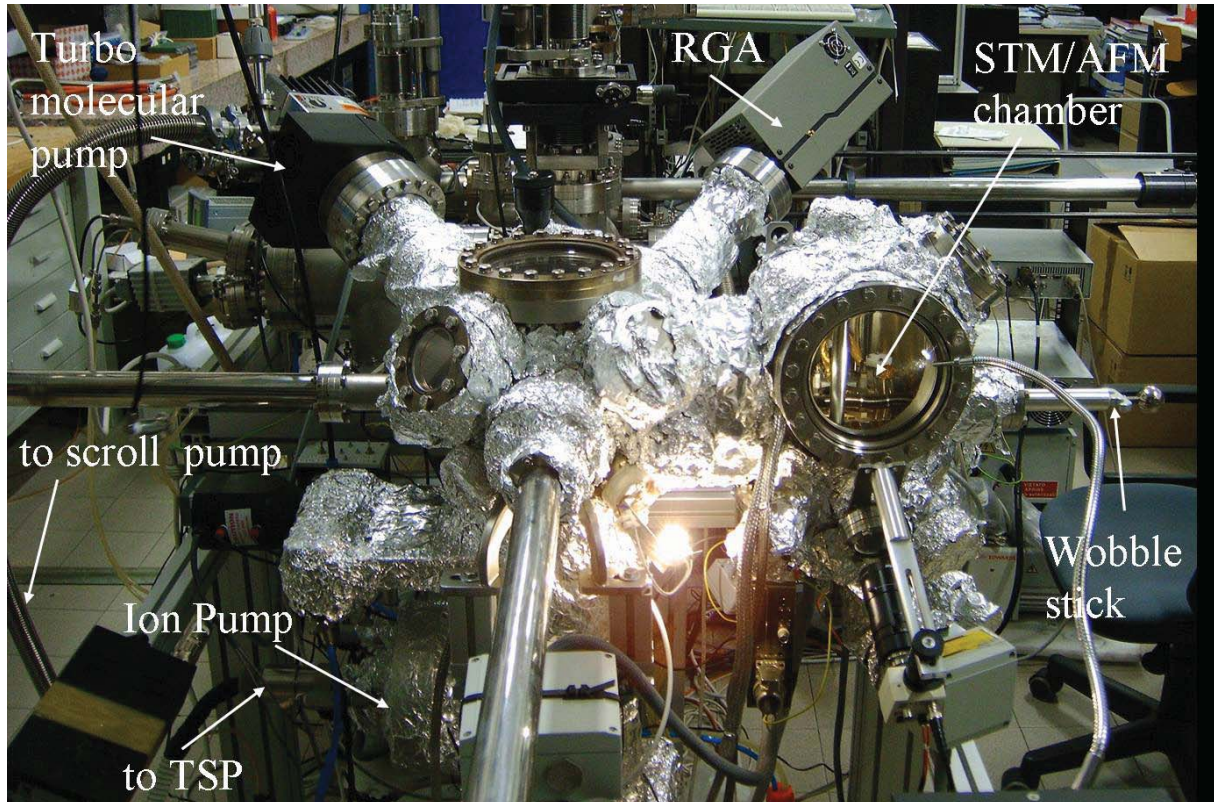


Figure 3.3.1: UHV system overview during bake out showing the sequential pumping, the residual gas analyzer and the SPM chamber with manipulator.

Figure 3.3.2 shows a final overview on the variable temperature UHV SPM system for in-situ deposition of organic materials directly onto the measurement stage. The system was modified frequently to continuously improve it and render it more independent. In this final optimized configuration a Fast Entry Lock (FEL) has been installed to introduce samples directly from air. The black bars represent vacuum gates that can be closed in order to separate different levels of vacuum from each other and allow to switch of the scroll and the turbo pumps which in contrast to the ion pump produce vibration and transmit it directly onto the system.

If a new tip or sample is introduced, the gate between FEL and the HV transfer chamber is closed and the scroll and turbo pumps are switched of. The FEL is at atmospheric pressure while the UHV part is below 10^{-9} mbar being constantly pumped by the ion pump and all other UHV gates are open. Then the FEL is pumped down first by the scroll pump and later also by the turbo pump. When a pressure of about 10^{-8} mbar is reached, the gate between FEL and HV transfer chamber is opened and the tip/sample is transferred into the UHV analysis chamber using the two vacuum manipulators. After the transfer, the FEL gate is closed again and the scroll and turbo pumps (and cooling fans) are switched off to reduce vibrations on the system.

The T-controllers for sample and effusion cell are set to the desired temperatures and the experiment can start. When heating locally in UHV, especially when introducing a tip/sample from air, degassing (thermally induced desorption from hot surfaces) takes place and it is recommendable to respect waiting times monitoring the pressure. The experiment is best started when the pressure reaches its minimum value.

A more detailed description of the VT-SPM and the organic effusion cell can be found in chapters 3.3.3 and 3.3.4.

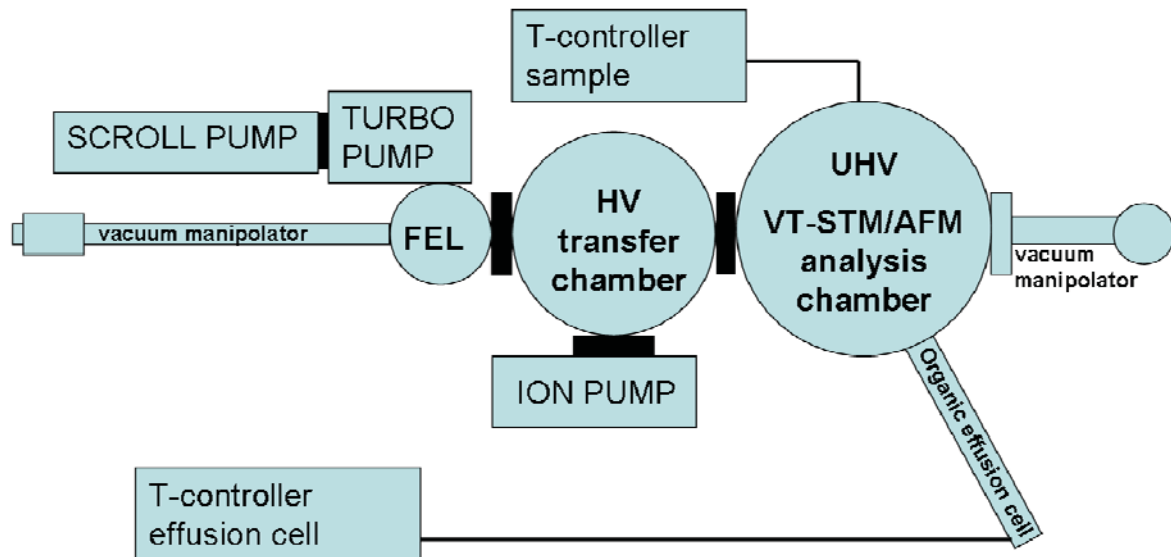


Figure 3.3.2: Schematic representation of the isolated VT UHV SPM in-situ deposition setup in its final independent configuration disposing even of a separate Fast Entry Lock (FEL) for sample introduction.

3.3.2. Custom-built vibration isolation

Vibration isolation is crucial for high resolution STM since the scanned area is in the nanometer range and the molecular surface corrugation is below 1Å. Therefore even very small noise can completely mask the real surface structure and introduce artefacts. Although the Omicron VT SPM XA is equipped both with a spring suspension and an eddy current damping mechanism, we experienced large vibrations during the measurements while the microscope was mounted onto a rigid frame and connected to a metal and organics deposition chamber. The origin of that noise is of multiple nature and despite accurate exploring and step by step exclusion of noise sources it is often not possible to identify precisely how the noise couples to the UHV system that behaves like a giant antenna.

On a rigid frame the most important sources of noise are building vibrations (typically around 20Hz), foot fall sound, cooling fans, scroll and turbomolecular pumps in the same room, people working on the metal and organics deposition chamber, mechanical sample plate or tip instabilities, etc. The type of coupling to the system (e.g. through mechanical connections of cables or water cooling circuits) can change the characteristic frequencies and make it impossible to find the noise source. Further many mechanical connections to the system are important for the respective experiment and can – even if clearly associated to the noise – not be removed.

We can precisely measure periodic noise by STM and associate all contained frequencies. In Figure 3.3.3 the noise analysis method employed to determine the disturbing frequencies is represented. The first row shows an STM image that was taken in the so-called point mode where the tip does not move but stands still while the current signal is sampled at constant time intervals. The resulting image represents an overlay of all disturbing frequencies. The frequencies can be determined by a two dimensional Fourier Transform and the image filtered accordingly like shown in Figure 3.3.3. The disturbing periodic noise displays 3 different contributions: 20Hz (probably building oscillations), 200Hz and 300Hz.

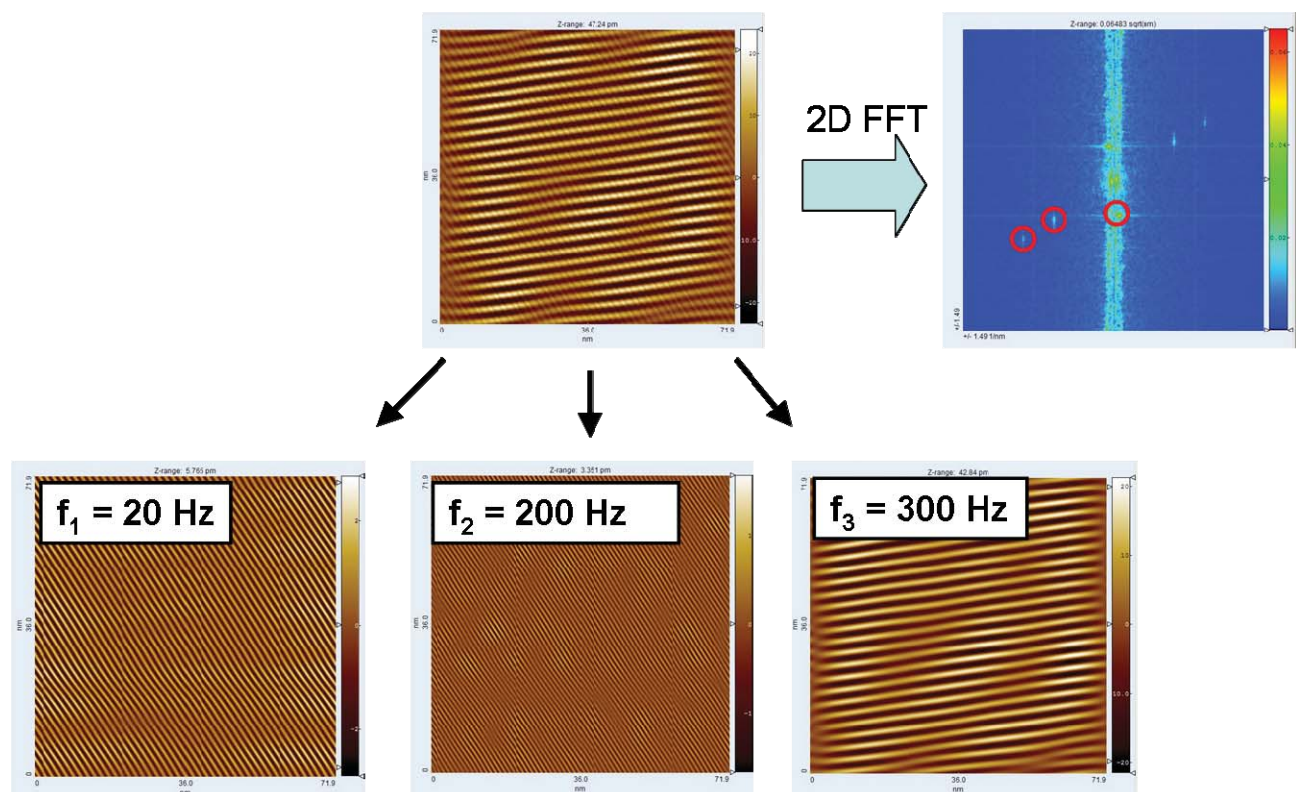


Figure 3.3.3: Noise analysis in STM point mode and 2D Fourier Transform to identify the contributing frequencies.

In order to overcome the experimental limitations associated with the periodic noise, we decided to physically isolate the growth chambers from the SPM chamber and to build a new base implementing a vibration decoupling and additional orientational degrees of freedom. The latter requirement is necessary to fine tune the overall orientation of the UHV chamber so that the spring suspended free hanging plate does neither touch the magnets of the eddy current damping mechanism nor the UHV chamber walls. This is a critical weak point of the microscope as there is little room left in the compact construction and both springs and the UHV system itself are subject to structural relaxations and changes in time, especially when baking the system.

The custom built vibration isolation frame is schematically represented in Figure 3.3.4 where some minor details have been omitted for clarity. A photo of the UHV-SPM system mounted onto the new frame is shown in Figure 3.3.5. In order to make the construction less sensitive to vibrations a two stage air cushion decoupling is employed. Further the hollow Bosch frame elements have been filled by sand to damp acoustic coupling. Sand is an excellent damping materials due to its granular structure. The big black troughs (see Figure 3.3.5) in fact are entirely filled by sand and the vertical frame is threaded through the circular opening at the top of the troughs.

In summary we realized an effective three stage vibrational decoupling and a positional fine tuning system of the overall UHV apparatus orientation through regulation of the air cushion pressures.

The removal of periodic noise from the microscope and UHV system has been verified by point mode STM measurements and noise analysis.

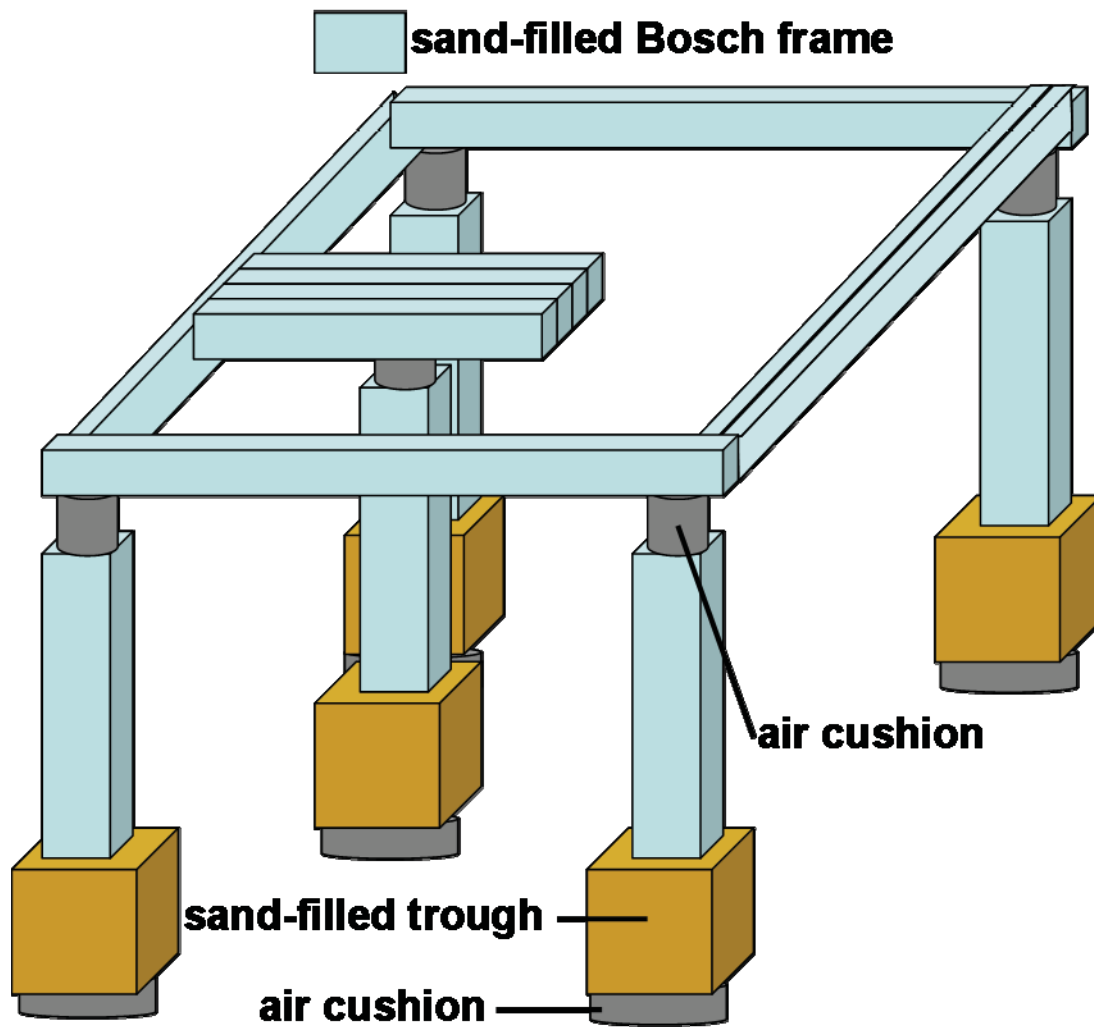


Figure 3.3.4: Schematic drawing of the custom built vibration isolation.

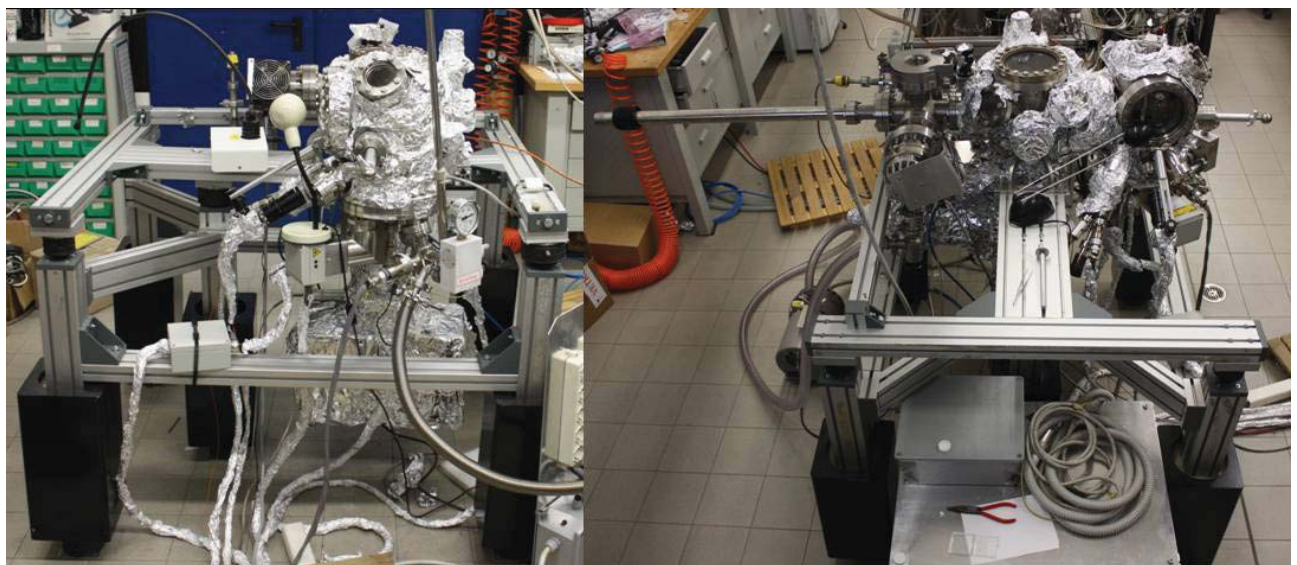


Figure 3.3.5: Side and front view of the UHV system mounted onto the custom built vibration isolation.

3.3.3. VT-UHV SPM

For successful high-resolution scanning probe microscopy a high quality vibration decoupling system is essential. The VT SPM XA base plate is suspended by four soft springs which are protected by surrounding columns. The resonance frequency of the spring suspension system is about 2 Hz. Vibrations of the suspension system are intercepted using a nearly non-periodic eddy current damping mechanism. For this the base plate is surrounded by a ring of copper plates which come down between permanent magnets.

The spring suspension can be blocked to allow tip or sample exchange, adjustments, etc. Blocking is achieved using a push-pull motion feedthrough (PPM).

Figure 3.3.6 shows the internal layout of the microscope with the above discussed two stage spring and magnetic vibration decoupling system. A photograph view of the measurement stage shows the suspension systems and the position of tip and sample in a face down configuration and with the tip mounted on the scanning piezoelectric tube. Further the variable temperature facilities, namely the resistive heating element and the flow cryostat with cold fingers are evidenced together with a schematic representation of the heat distribution in the sample stage in Figure 3.3.6. The compact design of the multitechnique probe stage for STM and AFM techniques requires a special optical pathway for the infrared laser used in AFM as force signal to allow for high precision positioning. The three mirrors Lx, Ly and LPSD can be regulated at any time via motors and especially LPSD can compensate thermal effects when approaching a hot surface. We stress that in UHV heat transfer between tip and sample in non-contact AFM occurs exclusively via radiation that has a strong dependence on the tip-sample distance. Further temperature changes have a pronounced effect on heterostructures with different thermal expansion coefficients like AFM cantilevers with reflective or conductive coating. When cooling the flow cryostat with liquid helium sample temperatures as low as 62K could be reached while the use of liquid nitrogen reaches about 140K. The resistive irradiation heater with a maximal power of 5W (max current 0.5A) can reach temperatures up to 240 °C that have also been used for sample degassing purposes.

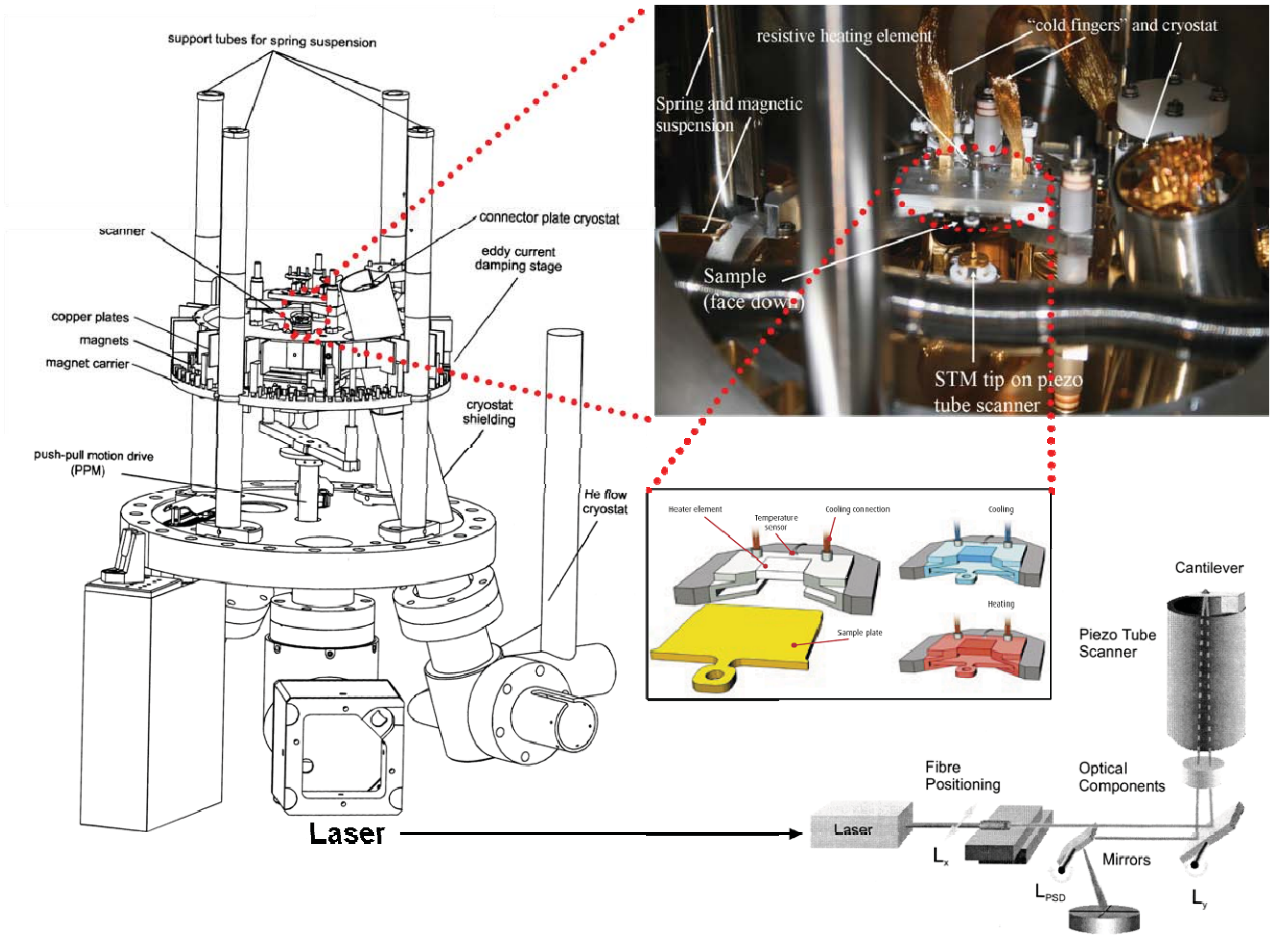


Figure 3.3.6: Internal layout of the VT UHV SPM XA showing the two stage vibration isolation system, a magnification of the measurement stage, heating/cooling facility and optical pathway for the compact AFM design.

3.3.4. In-situ OME cell and real-time SPM

The Organic Material Effusion cell (Dr. Eberl MBE Komponenten GmbH, Germany) was developed for accurate evaporation or sublimation of high vapour pressure materials like organics or polymers. It is therefore optimized for low temperature operation from room temperature up to 250°C. Optional an operation temperature even below room temperature is possible using suitable water cooling parameters.

Conventionally used radiation heated and cooled low temperature effusion cells show a poor cooling efficiency at ambient operation temperatures due to the T^4 dependency of the emitted radiation power according to the Stefan-Boltzmann-Law. This results in a low cell cooling rate and in a high cell cooling time constant which makes a precise temperature control difficult. Further conventional cells use direct mounting of the crucible onto the radiation heater wires can locally overheat the evaporant which may result in fluctuating evaporation rates and even in decomposition of temperature sensitive materials.

In contrast the OME-40 shown in Figure 3.3.7 uses the linearity of the heat transfer between a heated reservoir (B3) and a cooled heat sink (B8) to obtain a high cooling rate even at very low temperatures. Thus rapid cooling down, low thermal time constant and stable temperature control are achieved. The liquid metal (B2) applied as a thermal conductor between the crucible and the heat reservoir provides a direct thermal connection without isolating voids for a uniform temperature distribution within the crucible. The directly contacted thermocouple (B5) situated immediately below the crucible provides a precise temperature measurement [⁴⁰].

Figure 3.3.7 C shows the OME cell connected to a PID control loop for constant source temperature consisting of a DC power supply and a PID controller. The controller permanently reads the actual crucible temperature and sends a controller output signal to the power supply corresponding to the difference of the desired temperature setpoint and the actual temperature.

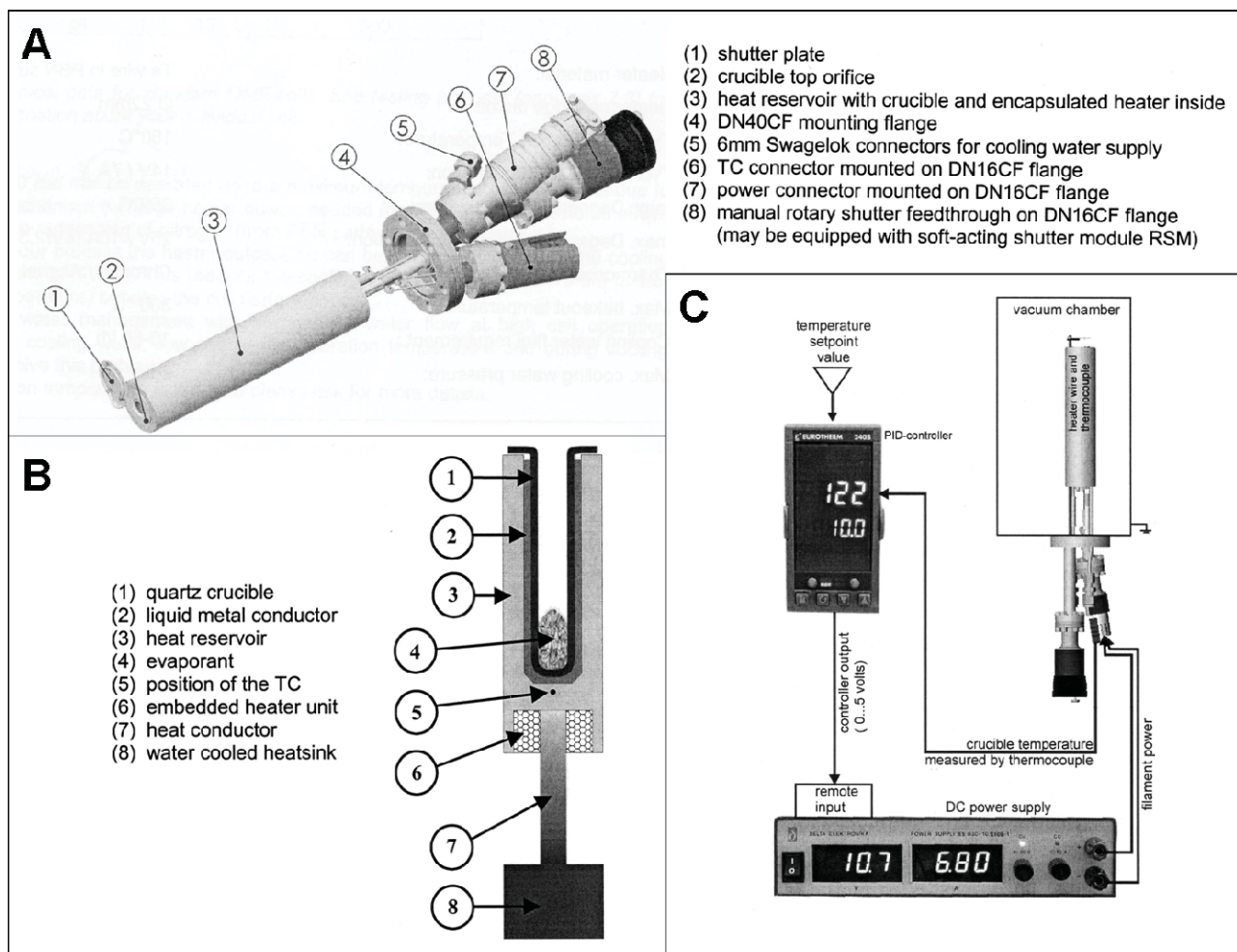


Figure 3.3.7: (A) Organic material effusion cell details. (B) Schematic of internal construction showing loaded crucible. (C) PID control loop for constant source temperature.

Figure 3.3.8A shows a photo of the experimental setup for in-situ real-time SPM investigations during the sublimation of organic semiconductors. It is crucial that the OME cell is precisely aligned in order to avoid accidental coating of tip, piezo and the heatable sample stage. A specially designed nozzle with an opening angle of 5° guarantees a beam spot size of about 13 mm at the sample stage covering hence the entire sample of a maximal size of 11 mm (see Figure 3.3.8B).

A careful alignment according to Figure 3.3.8C using a centering rod and the LCD camera is made possible by the use of a port aligner.

A schematic representation of the final configuration of an in-situ deposition STM experiment is shown in Figure 3.3.8D. Note that Scanning Probe Microscopy is a serial and rather slow technique. If the growth process is faster than the imaging time, the micrograph will not show a stationary surface but an evolving one. It is possible to interrupt the sublimation by closing the shutter in order to capture a stationary film structure. Therefore the technique is not a true real-time measurement but can be

defined quasi real-time since the film evolution with interrupted beam and constant substrate temperature is almost negligible.

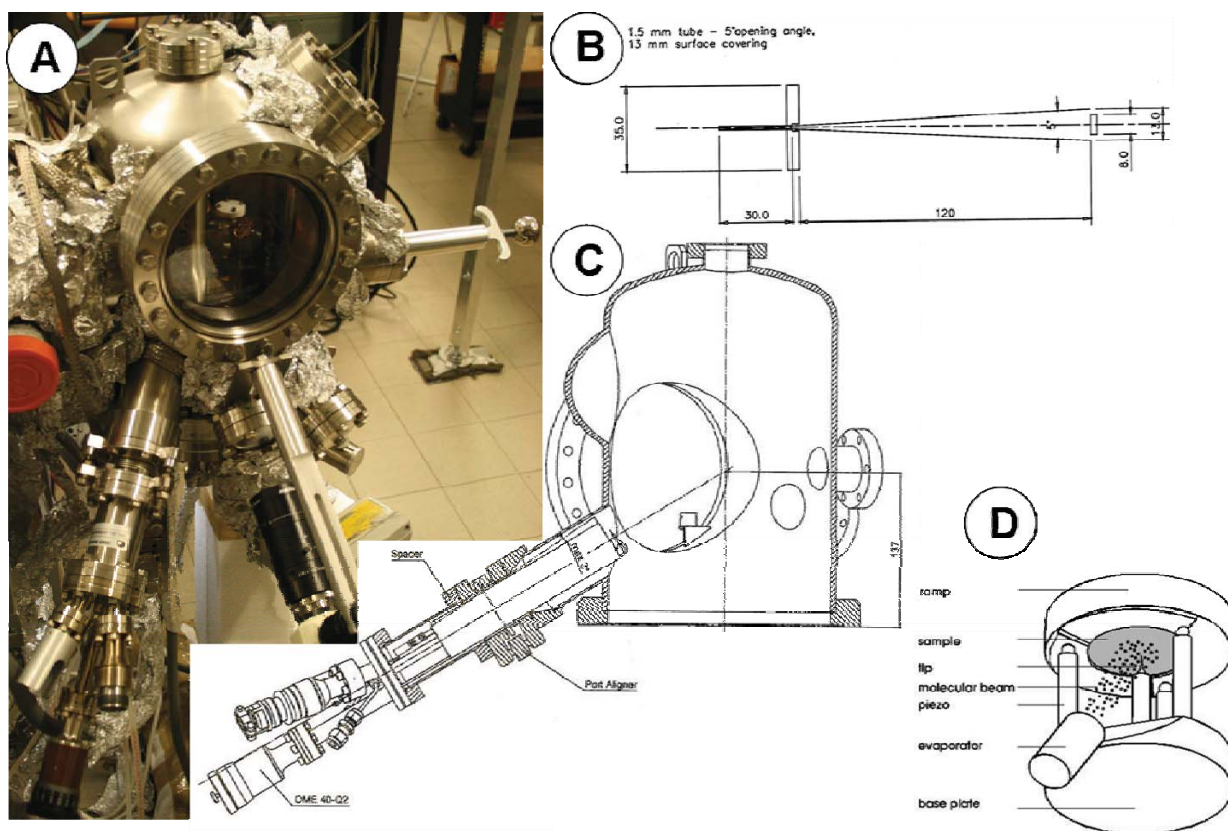


Figure 3.3.8: (A) OME cell mounted on the VT-SPM analysis chamber. (B) Physical OME cell constraints determine a beam surface covering of diameter 13 mm. (C) Technical drawing of the perfectly aligned cell pointing at the sample stage. (D) Schematic drawing of the in-situ real-time deposition experiment .

Unlike in most OMBD setups, in the present configuration there is neither a quartz microbalance nor a flux monitor in order to measure the deposition rate or the overall deposited quantity. However, the availability of a Scanning Probe Microscope allows to monitor the local (max $8\mu\text{m} \times 8\mu\text{m}$) surface coverage at arbitrary intermediate deposition stages and infer on deposition rate and coverage.

The deposition rate in particular is governed by the cell temperature and the pressure. The quantity of evaporant can also influence the deposition rate but is of minor importance in the here presented study since we use very low deposition rates and ultrathin films. Rather this indirect method to determine the deposition rate gives insight in growth processes that traditional techniques are not able to provide. It is known that when depositing materials with low sublimation temperature ($<300^\circ\text{C}$) on hot surfaces (around 100°C), a part of the hot molecules of the beam does not permanently adsorb

onto the sample surface but redesorbes into the vacuum due to the high thermal energy and deposits on a colder surface (e.g. chamber walls, cold trap).

Hence, measuring the coverage evolution at fixed time intervals, corresponding to a fixed deposition time, provides an estimate for the deposition rate that accounts only for the effectively adsorbed molecules why we name it “effective deposition rate”. Given that taking an SPM image takes some minutes and surface shading by the tip can alter the local coverage, the deposition should be interrupted during the SPM measurement by closing the cell shutter for best rate estimates.

As the cell temperature and the substrate temperature are the only two parameters we control at comparable UHV conditions, we performed a test on the reproducibility of the effective deposition rate.

Two deposition sequences at the same cell temperature of 260°C and a substrate temperature of 80°C were carried out on different days. The results are shown in Figure 3.3.9. (A) shows a plot of the integral coverage (viz. total deposited material) versus the deposition time. In the first case (black) 12 depositions of 5 min each were performed and imaged immediately after closing the shutter, in the second case (red) the chosen deposition interval is 20 min and only 5 depositions were carried out. By definition the slope of the graph shown in (A) is the effective deposition rate at 80°C substrate temperature that is 1 Å/min for both 5 min and 20 min deposition intervals.

This fact implies that the effective deposition rate is reproducible and depends on substrate temperature and cell temperature. However the different deposition time intervals have a strong impact on the island shape as the morphology of the evidenced total deposition times at 20, 40 and 60 min in Figure 3.3.9B prove. While the first monolayer (20min) does not display noticeable differences, the shape of the second monolayer islands is much more dendritic for longer deposition intervals. Since the measurement time for an AFM image is about 30 min in the present case, the 5 min deposition interval sequence undergoes about $4 \times 30 \text{ min} = 120 \text{ min}$ of annealing at 80°C and closed cell shutter while the 20 min sequence undergoes only 30 min of annealing.

The increased annealing time promotes diffusion and results therefore in a less dendritic island shape. If we compare the morphology at 60 min close to the completion of the second monolayer we can again see no major differences.

We deduce from this test that the effective deposition rate is reproducible but if we want to compare the spatial film parameters (e.g. the island shape) we must use identical deposition time intervals (annealing times), especially for long imaging times and in the island aggregation regime.

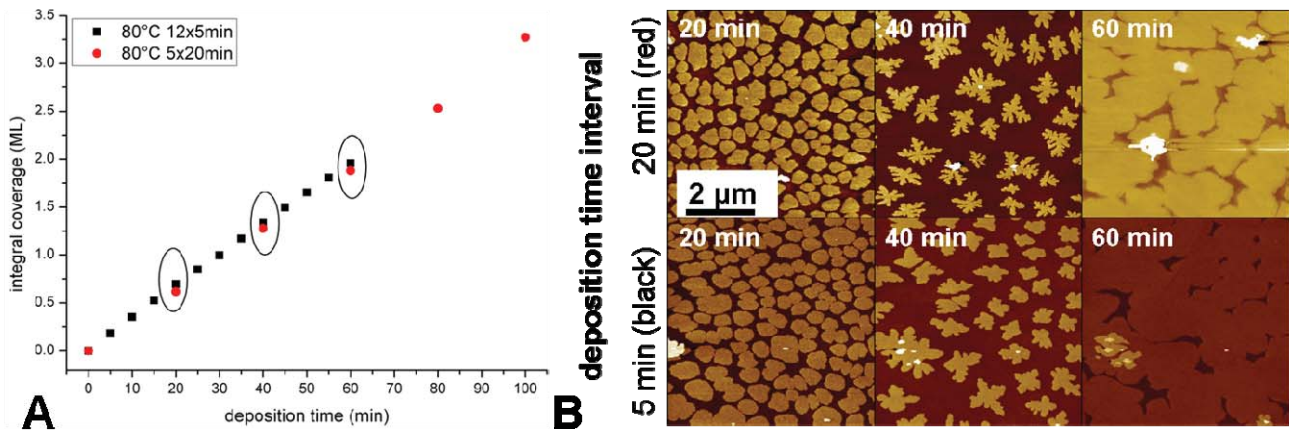


Figure 3.3.9: (A) Integral coverage vs deposition time for two different deposition sequences reproduce the same slope of 1Å/min that is the effective deposition rate at 80°C substrate temperature. (B) Morphology corresponding to the sequences with 5min and 20 min deposition interval that are marked in (A).

3.4. SPM tips, mounting and fabrication

For UHV SPM special techniques are used to prepare, clean and handle probes and samples. Here, like shown in Figure 3.4.1, two types of tip holders are employed: the straight tube STM tip holder and the AFM cantilever holder. Both holders are mechanically and electrically interfaced by three pins to the instrument.

Figure 3.4.1 further shows the VT AFM scanner with radiation shield to prevent scanner artefacts during measurements at high and low temperatures.

We introduce here to the STM tip fabrication methods and to practical issues for mounting and UHV preparation of commercial AFM tips.

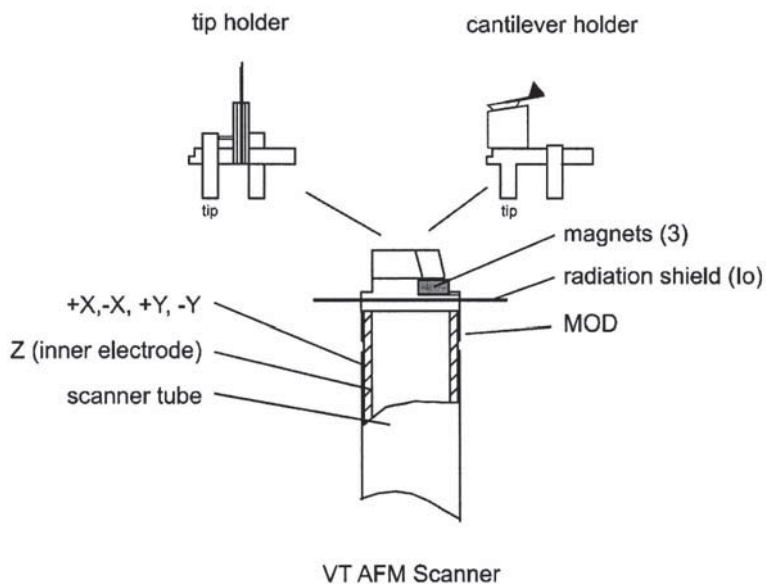


Figure 3.4.1: STM and AFM tip holders for mounting onto the scanner tube.

3.4.1. STM tips

STM tips are commercially available but it is common practise to fabricate them in the lab. The main two approaches to STM tip fabrication are but mechanically cutting Platinum-Iridium wires (80% Pt, 20% Ir) of less than 0.35 mm diameter under tensile load. The “tear-cut “ tip is characterized by a hedgehog microscopic structure where the actual microtip used for tunnelling is not visible by eye and can be altered by in-situ tip conditioning using z-ramps and voltage pulses. The cutting under tensile load method is schematically described in Figure 3.4.2A. The soft metal alloy hedgehog microstructure produced by this method is shown in Figure 3.4.2B. It is not possible to experimentally control or verify the microscopic structure with reasonable techniques. In practice the tip is mounted on known surfaces are imaged to verify the tip quality. The great advantage of PtIr tips is the effective in-situ conditioning that changes the tip microstructure and hence the tunnelling conditions. Figure 3.4.2C underlines again that even an optically bad tip can embody a nanoapex and provide atomic resolution images. This methods is more random than tip etching but is straight forward and leads in practice to remarkable results.

Once the tip is cut it is mechanically blocked inside the cylindrical tube on the tip holder by clamping the tube or by bending the tip in a springlike fashion. Before insertion into UHV the tip holder is baked for 2 hours in an oven at 120°C to remove adsorbed molecules.

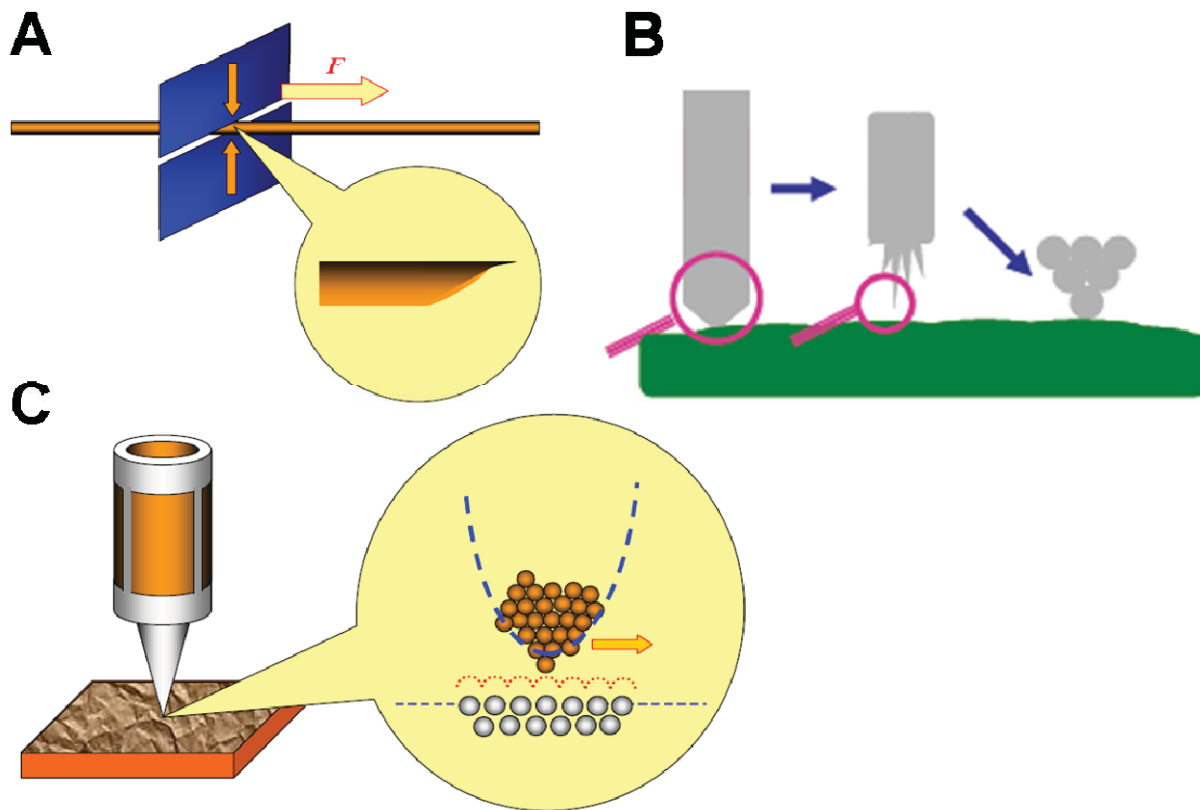


Figure 3.4.2: (A) PtIr wire cutting method applying a tensile load F with the cutter. (B) Microscopic view on mechanically cut PtIr wire and its hedgehog microstructure. (C) For ideal atomic resolution images only the closest atom of the tip is relevant.

The second established tip fabrication method is electrochemical etching. Different variants have been reported using DC or AC voltages, different electrolytes and tip materials and multiple step etching processes.

We used a DC etching setup with a tuneable DC generator at about 5V with a ring shaped platinum anode shown in Figure 3.4.3. The Pt-ring has a diameter of about 10 mm and a meniscus of 2-molar KOH is built up by dipping it into a beaker filled with KOH. Then the tungsten wire that is connected to the positive pole to favour the electrochemical etching reaction. Upper and lower tips have different characteristics due to the force of gravity acting on the lower tip segment throughout the etching process like shown in the inset of Figure 3.4.3. Other important parameters are therefore the length of the lower tip segment and the etching rate that can be shortened by raising the

concentration and/or the voltage. The upper tip is mechanically more stable but empirically less sharp than the lower tip. Both are shown as optical micrographs with a Scanning Electron Micrograph (SEM) inset in Figure 3.4.3.

During the etching reaction a layer of tungsten oxide and alkali residues deposits on the tip apex why the tip is rinsed with distilled water and optionally dipped into 20% HF solution for some seconds to dissolve the tungsten oxide. However, tungsten tips should be further conditioned in situ by annealing, voltage pulses and e.g. z-ramps on gold to pick up gold atoms to improve their resolution. A drawback of electrochemically etched tungsten tips is that, unlike PtIr tips, once they have crashed they can usually not be recovered by in situ conditioning.

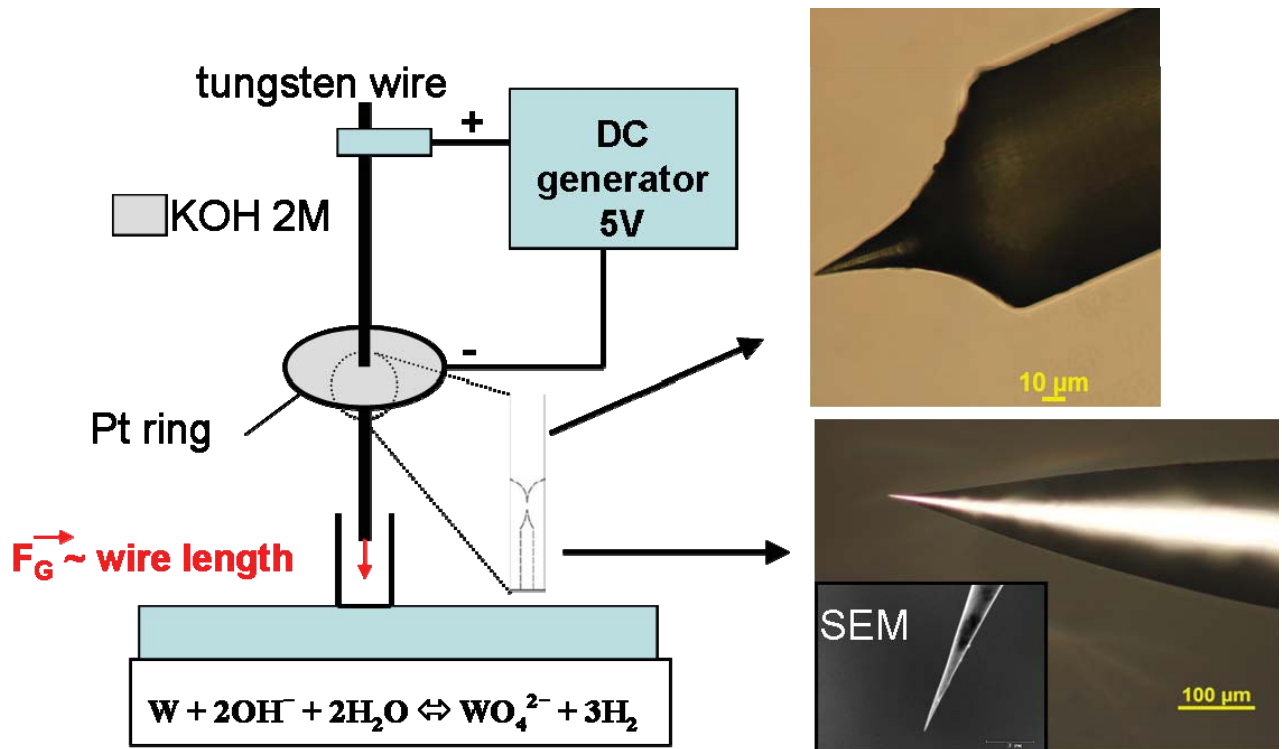


Figure 3.4.3: Direct current W tip etching setup with zoom on etching zone, reaction equation and optical microscope and SEM images of upper and lower tip.

3.4.2. AFM tips

Tips for AFM, also termed cantilevers are microfabricated commercial products like shown in Figure 3.4.4A. In order to use these cantilevers in UHV conditions they must be glued to a Omicron tip holder and positioned using the glueing device shown in Figure 3.4.4B.

The precise positioning procedure using an optical microscope and the crosshair of the glueing device is shown in Figure 3.4.4C. It guarantees that the laser hits properly the reflective backside of the cantilever and that we obtain the maximal detector signal. Figure 3.4.4C further shows the designated grooving on the tip holder to be filled with conducting silver paste or UHV epoxy for conductive AFM experiments. The glueing device and the mounted AFM tip are baked for 2 hours in an oven at 120°C before immediate insertion into UHV. This procedure “cleans” silver paste, cantilever and tip holder as low sublimation temperature organic molecules desorb and are not introduced into UHV.

We used NT-MDT and Nanosensor non-contact cantilevers with spring constants ranging from 5 N/m to 50 N/m. A higher spring constant translates into a smaller oscillation amplitude at the same cantilever excitation voltage and leads to more stable oscillation and scanning conditions in UHV.

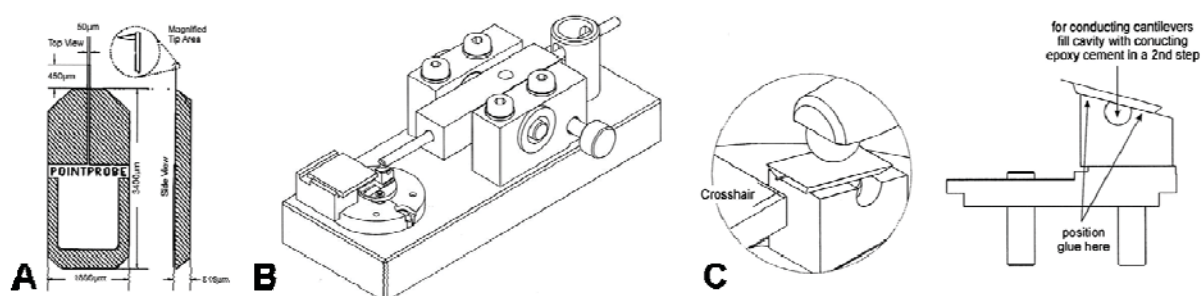


Figure 3.4.4: (A) Schematic drawing of commercial AFM tip. (B) Tip glueing and baking device. (C) Tip positioning and glueing.

4. Organic-metal and organic-dielectric interface

In this chapter, the morphology and electronic structure of ultrathin films of organic semiconductors on ideal and technical metal and dielectric surfaces is characterized and compared. We concentrate here mainly on the study of the organic semiconductor Sexithiophene (T6) and give examples for molecular organization on OFET devices for Pentacene (P5) and Perylene (PDI8CN2).

Competing intermolecular forces and molecule-substrate interactions in the first monolayers lead to a variety of morphologies that determine the electrical properties and the growth of multilayer films. Further, it was shown that charge transport in OFETs is confined to the first few layers at the interface which therefore need to be studied more in detail. The performance of current state of the art devices like Organic Field Effect Transistors (OFET) and Organic Light Emitting Devices (OLED) depends critically on understanding and controlling the organic material's molecular organization at interfaces like gold, silicon dioxide and indium tin oxide.

Two complementary techniques (STM and AFM) are used to study the organic films. While STM can obtain a higher resolution and allows to visualize the organization of organic semiconductors at a molecular scale, it necessitates by definition conducting samples. As a consequence the information it provides is not merely of morphological but also of electrical nature. In STM a voltage is applied between the imaging tip and the sample resulting in a current flow. Once fixed the voltage, the tip-sample distance can be regulated by a current setpoint. For substrates and samples with high resistivities it is necessary to lower the current setpoint in order to prevent the tip from crashing into the sample because the setpoint can not be reached. If this is not sufficient to obtain stable imaging, the absolute value of the voltage must be increased to increase also the flowing current. On ultrathin films that are weakly adsorbed and in an unfavourable orientation for charge transport from tip to sample, STM reaches its limits. The need to increase the voltage often leads to a modification or desorption of the weakly adsorbed ultrathin films.

For electrical characterization using the STM there are additional spectroscopic operation modes available that measure the current passing through the sample as a function of an applied voltage ramp (I-V spectroscopy) or distance ramp (I-z spectroscopy) between tip and sample.

Non-contact AFM is a complementary technique for non destructive morphological measurements that can be performed also on non-conductive samples due to the absence of a current signal and is therefore less invasive than STM. In Non-contact AFM a vibrating tip is scanned across the sample without touching the surface making it possible to trace the profile even of weakly bound ultrathin films.

4.1. T6 on Au(111) single crystal

The measurements were carried out with a UHV STM/AFM (Omicron Nanotechnology) at a base pressure of 10^{-9} mbar. Both STM and Non-contact AFM measurements have been performed to characterize the films. For the STM measurements electrochemically etched tips from 0.25mm tungsten wire were used. For the NC-AFM measurements commercial cantilevers (NT-MDT) were glued to the Omicron tip holder. The single crystal Au(111) surface was prepared ex-situ by chemical cleaning in piranha solution, boiling in distilled water and flame-annealing over a butane flame before fixing it with silver paste to a sample plate that was inserted after less than 20 minutes into the vacuum chamber.

The measurement chamber is equipped with an in-situ organic effusion cell (Dr. Eberl MBE-Komponenten GmbH) from which the T6 molecules were evaporated at a cell temperature of 258°C onto the Au(111) surface that was kept at room temperature in the measurement stage. From calibration measurements of T6 on native silicon oxide it is known that the cell temperature corresponds to a rate of approximately 1Å/min. The employed deposition time is 10min resulting in a nominal film thickness of about 1nm. The coverage of the adsorbed T6 molecules was determined by Non-Contact AFM after deposition. The combination of STM and NC-AFM measurements suggests that the molecules initially adsorb in a flat lying configuration, followed by an upright standing configuration on the completed flat lying monolayer.

In the following the observation of two different orientations are described and discussed.

The typical organization of T6 molecules found by STM on flat Au(111) terraces is shown for the image sizes 200 nm and 50 nm in Figure 4.1.1. The scan parameters are similar to those used for imaging the uncovered Au (111) surface. The T6 molecules form a closely

packed monolayer of parallel rows that follow mainly the same direction. However, especially in the 50 nm image a domain of tilted row direction emerges clearly. The two directly bordering domains are rotated about 120° with respect to each other. In the bottom left corner of the 200nm image the rotation angles of the rows are evidently smaller. The single rows are composed of T6 molecules that are stacked facing each other with their long molecule axis.

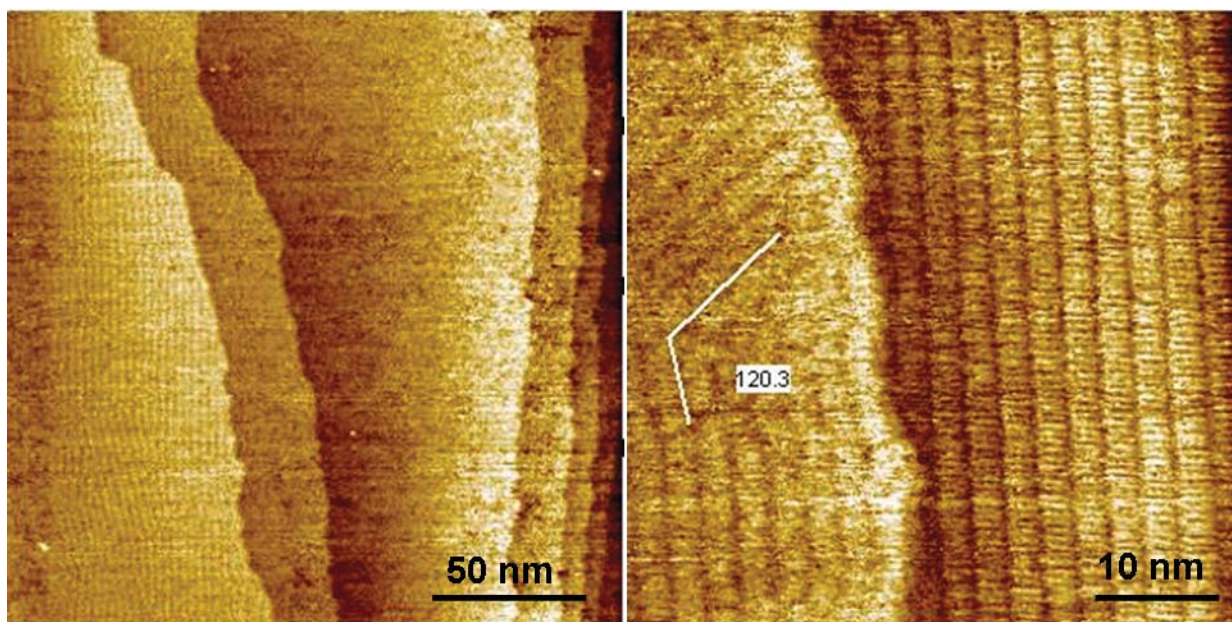


Figure 4.1.1: STM images (0.1V, 1nA) of flat lying rows of T6 adsorbed on Au(111).

The packing parameters and molecule dimensions are obtained from STM images using analysis of average profiles along and perpendicular to the molecular rows followed by a Fast Fourier Transform (FFT) on the profile to determine the dominant periodicity. The analysis and respective STM images are shown in Figure 4.1.2. The obtained value for the intermolecular packing within a single row is 0.58 nm and the value for the distance of adjacent rows is 2.75 nm. These values are in good agreement with the van der Waals dimensions of T6 and confirm that the molecules lie flat on the Au(111) with their Pi system parallel to the surface normal.

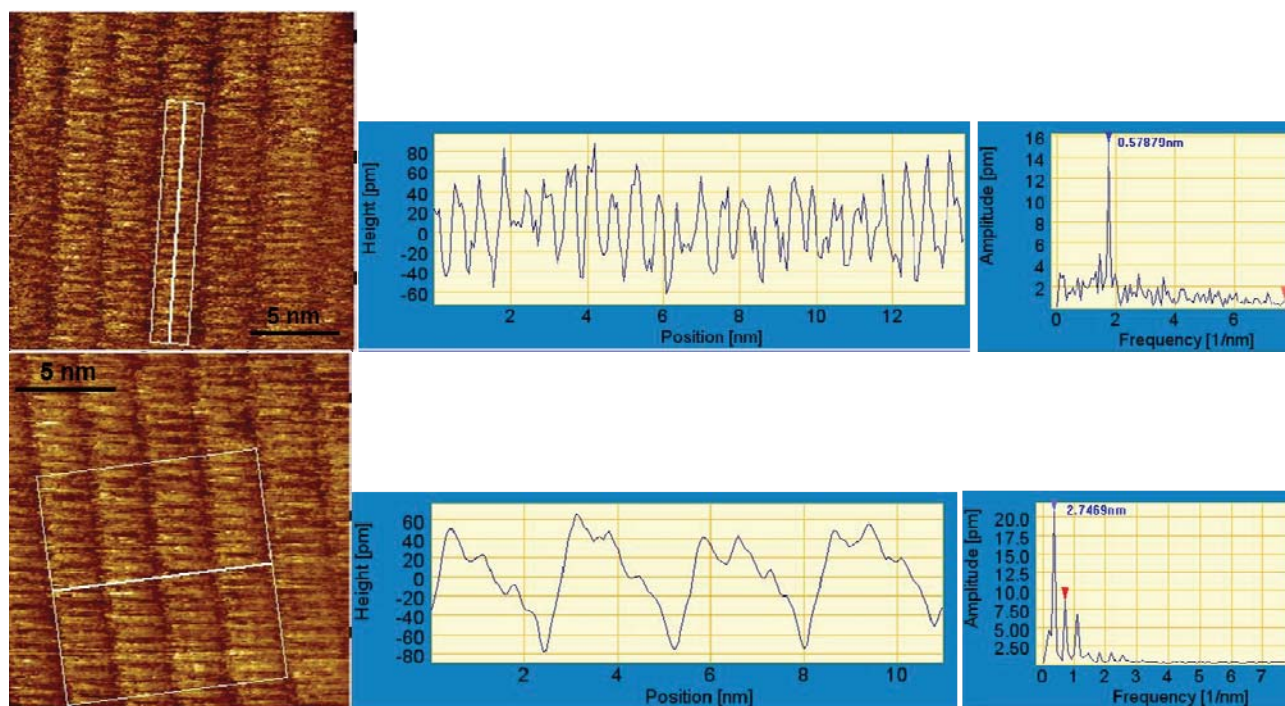


Figure 4.1.2: Average profiles and FFT for determination of the spatial parameters.

The STM scan sequence shown in Figure 4.1.3 makes clear that the standing islands adsorbed onto the flat lying monolayer are rather unstable upon STM imaging. Already in the first scan we can observe a modification of the islands leading to removal upon further scanning. It should be noted that the regions of the brighter regions of the islands where a second standing layer has started to form a nucleus are more stable. Probably the second standing layer leads to a stabilization that prevents tip induced desorption. In fact in the last scan the regions covered by a second layer are the only remaining structures, stabilizing even the standing layer underneath. Molecular resolution of the flat lying molecules in between the islands could not be resolved together with the islands in STM using common scan parameters. At scan parameters that are suitable for molecular resolution imaging (0.1V, 1nA) standing islands could never be observed. This suggests the electronic properties change for the standing islands on the lying monolayer. It is expected that the electrical transport through a stack of lying and standing T6 is worse than through a stack of lying molecules. In the latter case all Pi orbitals of the thiophene rings are parallel what provides a better overlap of the P_z orbitals than for orbitals that are oriented perpendicular to each other at the lying/standing interface.

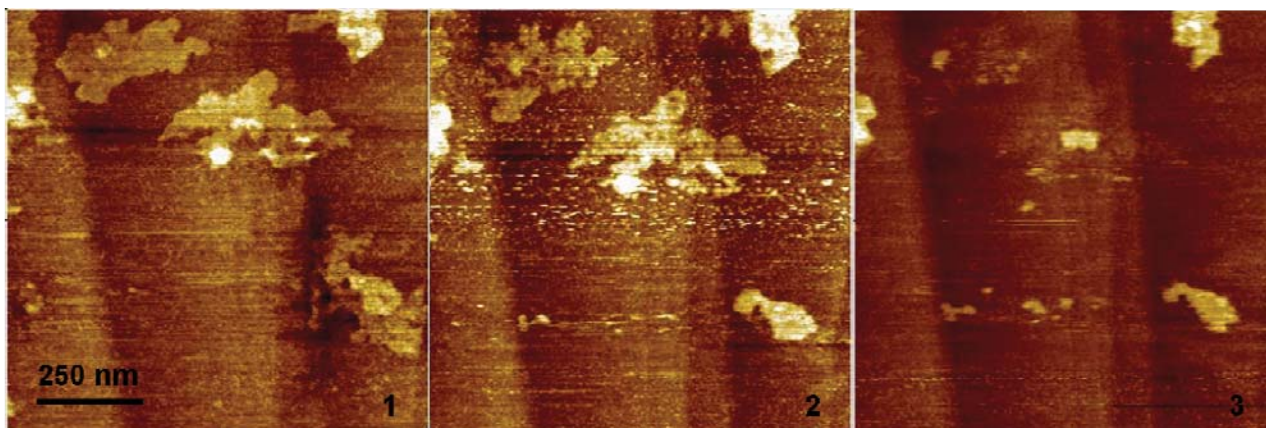


Figure 4.1.3: Consecutive STM scans (-1.3V, 100pA) show the desorption of the weakly bound standing islands.

Figure 4.1.4 shows a Non-Contact AFM image on a larger scale taken after the deposition. Although Sexithiophene has been found to grow on single crystal metal substrates with its long molecular axis parallel to the substrate surface up to a film thickness of several hundred layers [flat T6 au110][flat T6 Ag110 Ag111], here we find a coverage of 28% in a standing configuration with a mean height of 2.4 nm. Both values have been extracted from the corresponding height histogram depicted in Figure 4.1.5.

A standing configuration coverage of 28% or 0.28ML together with a mean height of 2.4nm translates into a thickness of 0.67nm. Assuming a complete coverage of the flat lying layer underneath the standing islands, the subtraction of the standing layer thickness from the nominal coverage of about 1nm gives an estimate of 0.33nm for the height of the flat lying monolayer, like shown in the model in the inset of Figure 4.1.5 . This value is half the size of the in-plane dimension of the molecule's van der Waals dimension perpendicular to the long molecule axis and confirms therefore that the flat lying molecules adsorb with their thiophene rings parallel to the surface, giving rise to two different adsorbed species with opposite chirality.

Further we can give an estimate for the orientation of the molecules of the standing layer by comparing the measured height to the theoretical. The van der Waals dimension of T6 along the long molecule axis is 2.7nm but we measure only 2.4nm. Excluding an effect of compression by the vibrating cantilever in Non-contact AFM, we can deduce that the reduced measured height is due to a tilt of the molecules with respect to the surface normal. In that assumption, simple trigonometrics suggest the tilting of the molecular axis of about 27° from the surface normal.

Most islands shown in Figure 4.1.4 nucleate as single standing layers extending across neighboring gold terraces without having their growth hampered by the vertical mismatch as depicted in the model in Figure 4.1.5. Further, on top of the islands we can identify small islands of a second standing layer. This pyramidal or 3D nucleation on top of standing islands suggests the presence of an energy barrier for interlayer (downward) diffusion greater than the thermal energy provided to the molecules at room temperature. Another possible explanation for this phenomenon that is observed on only about 20% of the islands in Figure 4.1.4 could be the presence of preferred nucleation centers in form of small defects or contaminations on the gold surface. Larger defects or adsorbants can be made responsible for the few bright 3D nucleations of a height of up to 30nm that do not resemble the dominating island shape. They can most likely be associated with polycrystalline T6 nucleations.

The more detailed image in Figure 3 confirms the nucleation of standing layers. We can find three different types of nucleations beyond the first standing layer along the profile: on the left the profile traces a bulk island of the height 7.2nm corresponding to three standing layers of 2.4nm and without any terraces to lower layers. Also its shape determined entirely by straight borders is different from that of the islands that present straight segments but are in general more dendritic. It is therefore likely that this triple layer island grew in a lateral fashion and constant height starting from a 3 ML height nucleation in defect more than layer after layer. The island in the center of the height profile lacks of a second standing layer but shows a seed of three and more standing layers at the island border. Most likely also this growth phenomenon is related to the interaction with a defect in proximity. We deduce that defects can induce both undefined polycrystalline nucleations and defined crystalline nucleations acting as seeds.

The third type of nucleation is represented by the very right profile and corresponding island. The second standing layer nucleates far from the island border and has a height of 2.4 nm. First layer islands exhibit structural defects in form of small holes that can be found also in the second standing layer. These vacancies incorporate into the islands during their growth and disrupt the intermolecular packing probably due to the influence of the substrate. Further we can say that protrusion-like defects form prevalently at gold step edges and not every defect is necessarily seeding the formation of an island or 3D structure.

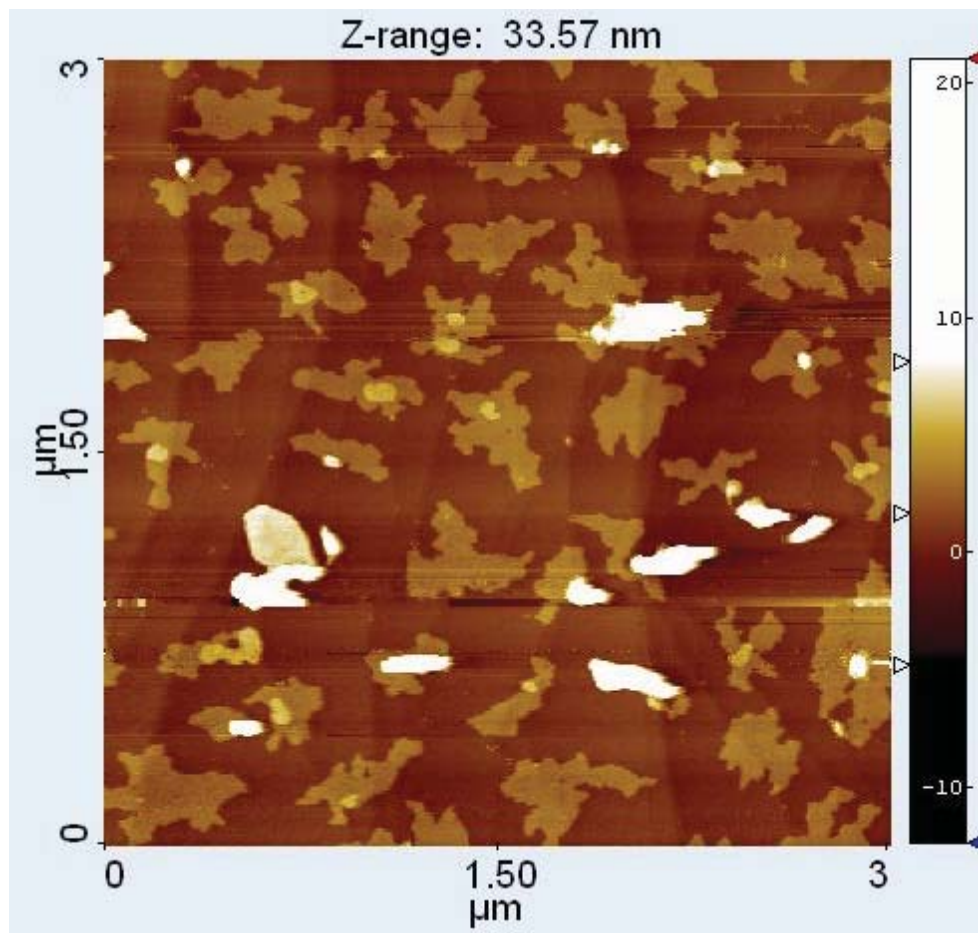


Figure 4.1.4: : Non-contact AFM image 3um x 3um shows standing T6 islands

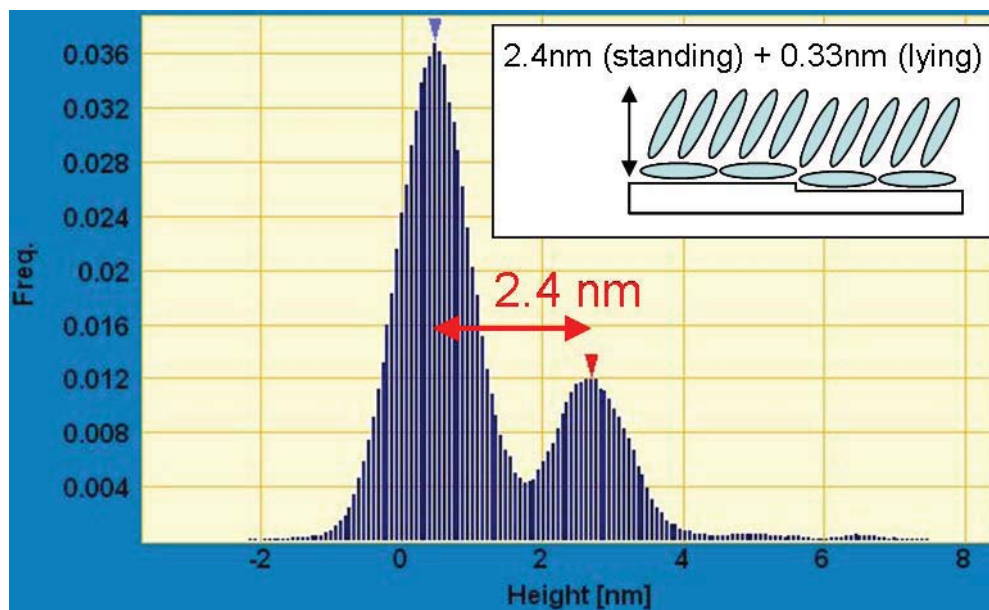


Figure 4.1.5: The height histogram shows an average island height of 2.4nm corresponding to standing molecules. The inset shows a model of the 2 different orientations and estimated dimensions.

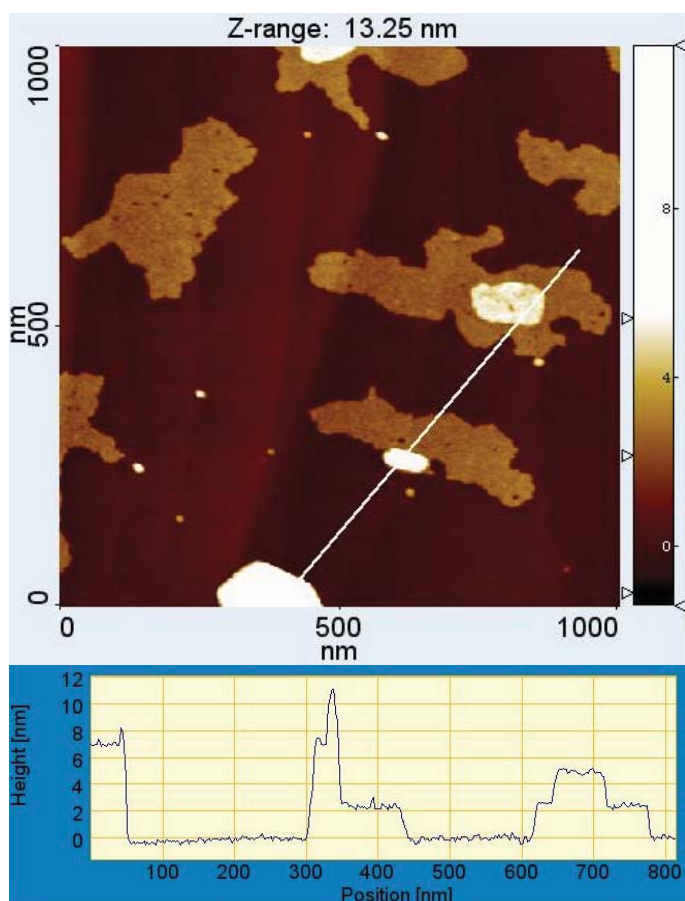


Figure 4.1.6: Different types of standing island nucleations and height profile along the white line.

4.2. T6 on polycrystalline gold surfaces

The single crystal substrate used in chapter 4.1 is an ideal surface exposing flat terraces of the (111) crystal orientation. It is an excellent substrate to study the interaction between T6 and gold in an ideal case and under UHV conditions. For technical applications however single crystal surfaces are far too expensive and unpractical. Typically, technical gold surfaces such as electrodes and wires in testpatterns and devices are made of polycrystalline gold. In the case of thin film devices in a bottom contact configuration, the electrodes and wires are evaporated onto the dielectric silicon oxide prior to deposition of the organic material. To improve the adhesion of gold on silicon oxide a thin layer of chromium, typically in the range of a few nanometers, is vacuum deposited prior to the gold forming an intermediate layer between the silicon oxide and the gold.

We use here a commercial gold substrate (Arrandee, Germany) that has the same characteristics as a technical gold electrode. In these samples a chromium layer of about 2.5 nm has been deposited onto a borosilicate glass to promote adhesion, followed by a layer of about 250nm of gold.

At first we examine here ultrathin films of T6 on solvent cleaned commercial gold substrates. The detailed cleaning procedure can be found in chapter ???.

The same deposition parameters as for the Au(111) crystal sample in chapter 4.1 were used in order to compare the effect on the organic semiconductor morphology of the less perfect polycrystalline surface. The sample was kept at room temperature and the deposition time was 10min at a cell temperature of about 260°C what results in a nominal coverage of about 1nm.

A Non-contact AFM image after the deposition is shown in Figure 4.2.1. The surface roughness is about 3 nm and therefore of the same order of magnitude as the polycrystalline gold film before the deposition of T6. No significant three dimensional aggregates can be found on the organic-metal interface. Also the standing islands found for the single crystal Au (111) are not present on the polycrystalline surface. Instead the morphology resembles very much the granular structure of the pristine polycrystalline film before deposition.

This suggests that the granular surface motif hinders the diffusion and aggregation of sexithiophene into regular structures like observed for the single crystal surface. It is

likely that the rather strong interaction of T6 with the gold surface that forces the first layer on the crystal surface to lie down leads to molecular disorder on the polycrystalline grains. At least for ultrathin films of about 1nm, the molecule-molecule interaction is not sufficient to induce a standing island order that extends over the grains and overcoming the rough morphology.

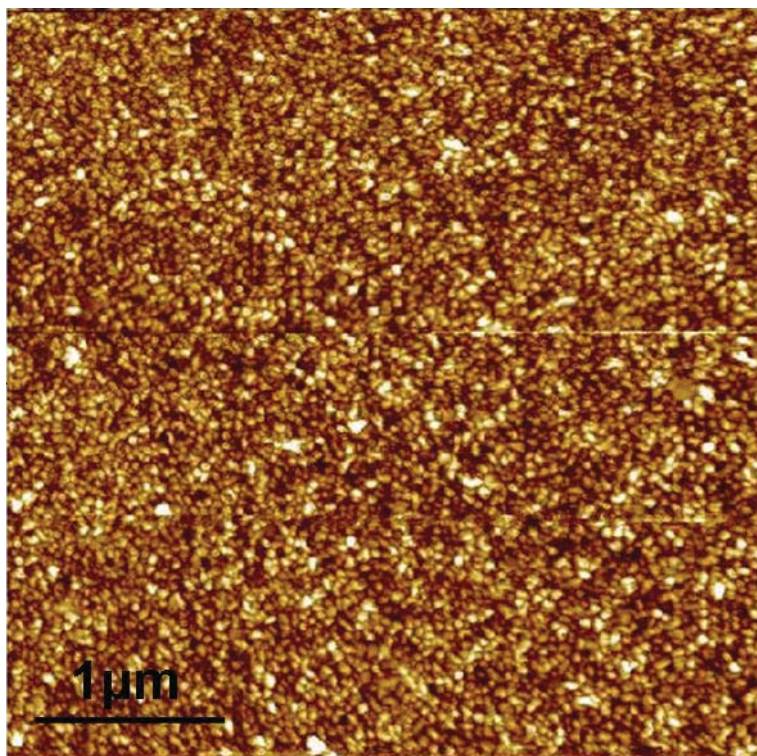


Figure 4.2.1: NC-AFM image of polycrystalline gold after the deposition of about 1nm of T6.

STM with its higher resolution allows to take a closer look to the local organization of T6. In Figure 4.2.2 a stepwise zoom in the same region is shown. There are no signs of desorption or scan induced modification indicating a strong interaction of the molecules with the surface. With increasing magnification a substructure of the single grains emerges. It is characterized by subgranular and lamellar structures. It is likely that the lamellar structures represent crystallites of T6.

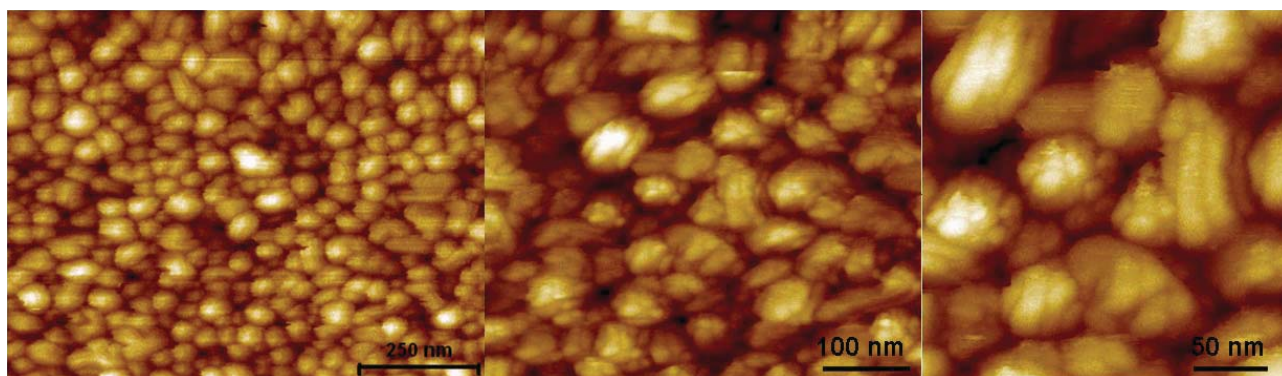


Figure 4.2.2: STM images (0.6V, 1nA) of 1nm T6 on polycrystalline gold.

While diffusion and aggregation on flat crystal terraces leads to the formation of a flat lying monolayer and standing islands (see chapter 4.1), the morphology of T6 on polycrystalline grains does not exhibit flat islands but granular and lamellar structures. The huge differences in morphology between the single crystal and the polycrystalline gold surfaces can most likely be attributed to the local flatness of the substrate. To confirm this assumption, we examine a flame-annealed polycrystalline sample that represents a compromise between the pure single crystal and the pure polycrystalline surface. Flame-annealing (see chapter ???) is a preparation technique in which the polycrystalline gold surface is repeatedly exposed to a flame. During this procedure the polycrystalline grains melt and the surface reconstructs forming in general much larger and flatter grains than before annealing and locally exposes the crystalline Au(111) surface. After flame-annealing the sample has been washed in double distilled water and the introduced into the UHV chamber.

For the deposition onto the flame-annealed gold film we used the same deposition parameters as for the single crystal and the polycrystalline film (cell $T=260^{\circ}\text{C}$, sample $T=\text{RT}$, deposition time $t=10\text{min}$) that result in a nominal film thickness of about 1 nm.

The morphology formed by the sexithiophene on the flame-annealed gold (Figure 4.2.3) is very different from the morphology obtained on a polycrystalline film (Figure 4.2.1). Since both substrates are identical apart for the flame-annealing treatment the different organization can be attributed to the flame-induced surface reconstruction.

The flame-annealed sample in Figure 4.2.3 shows a series of 3D aggregates, crystallites and standing islands of T6. The details of crystallites and islands are shown as magnifications for the regions A and B on the right. Figure 4.2.3A shows a set of aligned crystallites. The sharp angles and lamellar substructure are clearly visible. Figure 4.2.3B instead shows dendritic islands of standing T6. at the center of the islands we can identify

protrusions that are due to a second standing layer that starts to nucleate and 3D structures that may have nucleated before the island acting as a nucleation center for the upright standing molecules.

Most of the 3D agglomerates nucleate close to and along the grain boundaries of the annealed gold while the islands are found on the flat regions of the gold grains. This observation can be explained by the assumed diffusion and aggregation mechanism: The molecules that arrive in the vapour phase on the surface start to diffuse until they meet an adsorption site that immobilizes them. The grain boundaries are more reactive than the flat surface exposing two surfaces to the molecules that land or diffuse in the gap. Therefore it is expected that the 3D aggregates in grain boundaries form at an earlier stage than the standing islands. The nucleation of the standing islands might be facilitated by defects, contaminations and 3D aggregates.

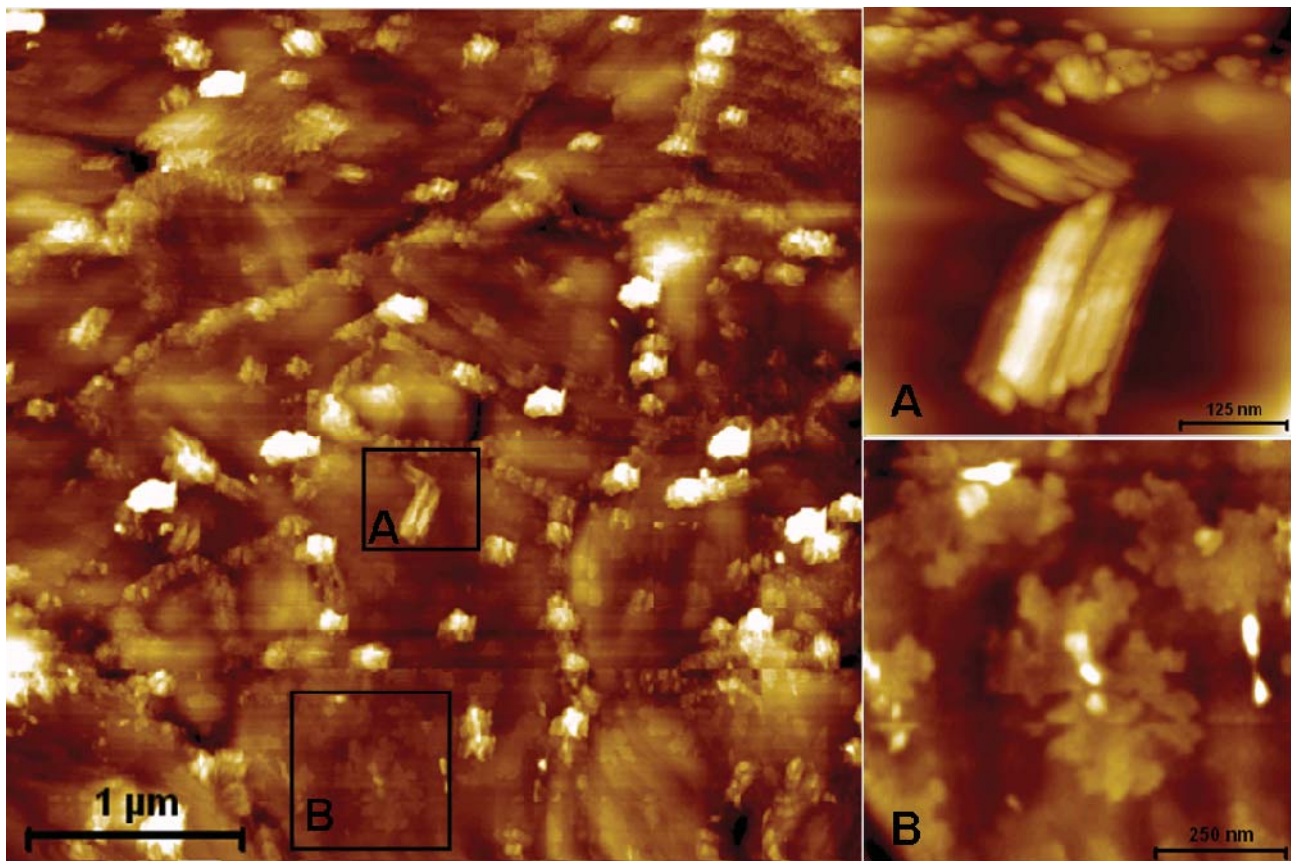


Figure 4.2.3: NC-AFM image of flame-annealed polycrystalline gold with about 1 nm of T6. Zoom on crystallite and standing islands.

The morphology of T6 in the flat regions of the grains reminds of the molecular organization found for T6 on a single crystal Au (111) surface (see chapter 4.1). We remind that the upright standing sexithiophene molecules revealed in STM a flat lying layer below them. Therefore we can expect that also the standing islands on flame-annealed polycrystalline gold have a flat lying layer below.

In Figure 4.2.4 a detailed Non-contact AFM image shows indeed a granular surface structure between the standing islands that confirms the idea of a flat lying layer below. The height profile depicted in the same figure clearly demonstrates the island height of 2.4 nm corresponding to standing molecules and shows a height of about 12 nm of the lamellar crystallite at the center of the island.

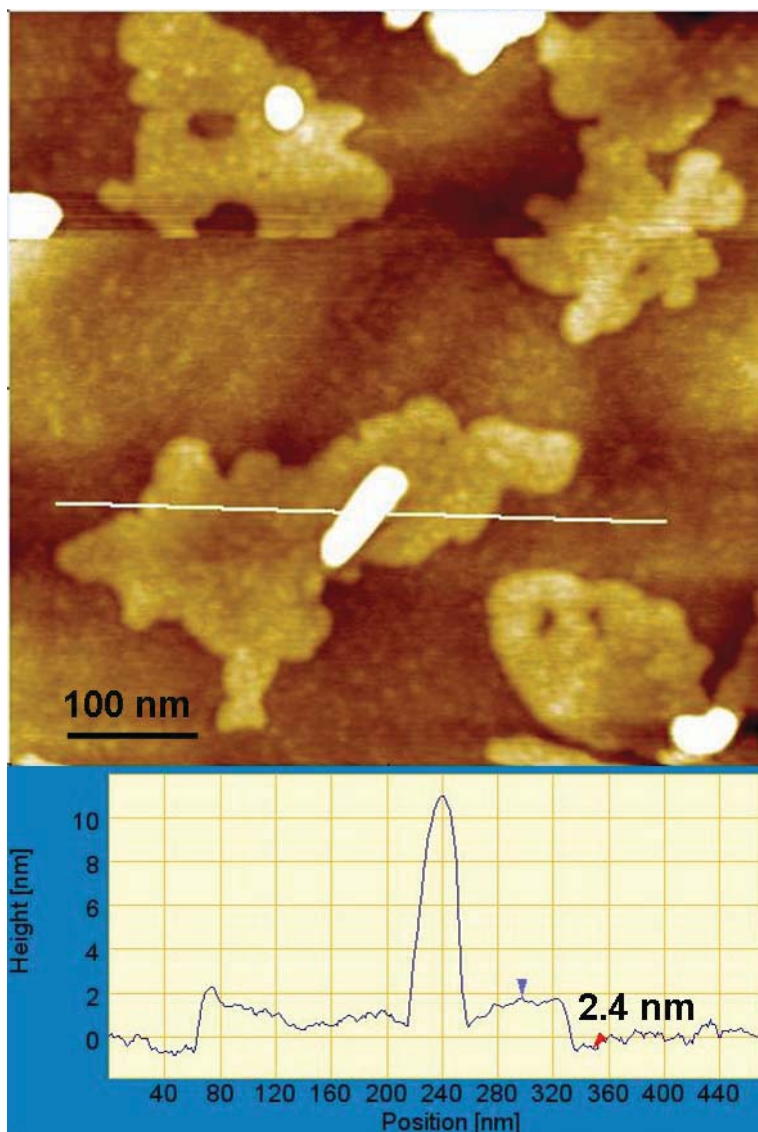


Figure 4.2.4: Upright standing T6 islands and crystallites on flame annealed gold (NC-AFM).

4.3. T6 on native silicon oxide

4.4. T6 on indium tin oxide

Indium tin oxide (ITO, $\text{In}_2\text{O}_3:\text{Sn}$) is one of the most widely used transparent conducting oxides because of its two chief properties, namely electrical conductivity and optical transparency. ITO is a heavily doped, n-type semiconductor with an optical band gap of 3-4 eV.

Commercially available ITO is normally deposited by sputtering techniques which, however, produce a relative high roughness typically in the range of 10-20 nm. Such a high rms roughness poses problems for an effective deposition of the active layers⁴¹.

Even though the organic semiconductor/ITO interface is of interest for technological applications (cite AL/T6/ITO devices), thin organic films of T6 have to our knowledge never been studied by AFM or STM.

One reason for the missing investigation might be the quality of ITO surfaces and especially their high roughness. However, using other deposition techniques than sputtering, the surface roughness could be reduced. Matino et al. reported rms roughness values as low as 5.7 nm for ITO films deposited on Corning glass by reactive electron-beam evaporation⁴².

We used extremely flat ITO substrates manufactured by VisionTek Systems Ltd., UK exhibiting an even lower surface roughness of about 0.2 nm, measured by AFM on an area of $5\mu\text{m} \times 5\mu\text{m}$ shown in Figure 4.4.1.

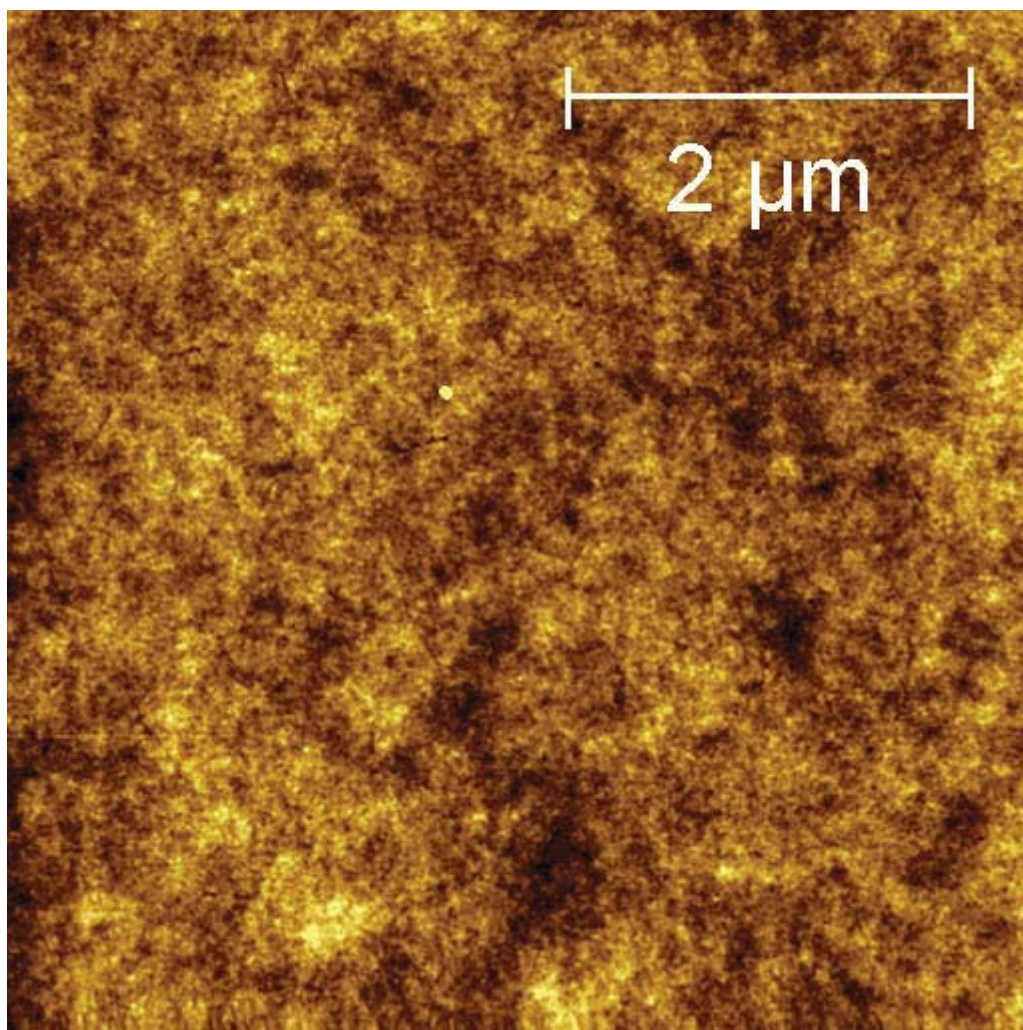


Figure 4.4.1: AFM image of the bare ITO surface before deposition exhibits a very low surface roughness of about 0.2 nm.

The deposition of T6 on ITO was carried out at room temperature in a high vacuum chamber equipped with a quartz microbalance. For AFM and STM investigation the sample was extracted from the deposition chamber and introduced into the UHV measurement chamber exposing it to atmospheric pressure and air for some hours.

As measured by the quartz balance, an amount of 66 ng was deposited in 12.5 min onto the sample kept at room temperature. The Non-contact AFM images show a submonolayer film consisting of flat islands. The first layer islands exhibit a coverage of 50% or 0.5ML (see Figure 4.4.2a+b) while second layer nucleations are rare covering only about 0.1% of the surface indicating a good downward transfer of molecules that land on the islands (low Schwoebel barrier at room temperature). The average island height is 2.2 nm, determined from the height distribution histogram shown in Figure 4.4.2c. This value is smaller than the height typically found for islands that nucleate on

silicon dioxide (2.4 -2.5 nm) what suggests that the molecules still nucleate in a standing configuration but have their long molecular axis tilted more towards the surface resulting in a lower average height. Again we use simple trigonometry and the Van-der-Waals dimension of Sexithiophene (2.7 nm) to estimate a tilting angle of about 35° from the surface normal. Using the deposition time, the coverage and the average island height, we can calculate the deposition rate as 0.88 Å/min. Given that the substrate is kept at room temperature we do not expect thermally induced reevaporation.

Figure 4.4.2a and b show the morphology of a submonolayer film of T6 on ITO with an area of about 50% covered by islands. The white line in Figure 4.4.2b traces a height profile shown in Figure 4.4.2d. It confirms the approximate height of 2.2 nm for the first and also for the second layer nucleations. The measured RMS roughness is about 1.1 nm and has reached its maximum for the first monolayer corresponding to the half monolayer height at a coverage of 50% in agreement with theoretical relationship between coverage and roughness (ref..formula or paper).

In order to line out the differences of the nucleation on ITO with respect to silicon dioxide we calculate some morphological and statistical parameters. It should be noted that parameters like for example island density and island size are affected by the area that is considered for their calculation, as well as by border effects induced by islands that are not entirely shown because they lie on the border of the scan area. Furthermore at a coverage of 50% coalescence of neighbouring islands is present. Coalesced islands can be distinguished by their shape from non coalesced islands as shown in Figure 4.4.3 by the labels I, II and III. We consider here a total quadratic scan area of 6µm x 6µm (Figure 4.4.2a). A grain detection based on a height threshold counts 88 elements excluding the image border. Among these we can identify 24 islands that are a result of the coalescence between two neighbouring islands making up about 27% of the detected elements. Doubling the number of coalesced islands in the total island count, it is possible to obtain an improved estimate for the nucleation density $n = 3.1 \mu\text{m}^{-2}$.

The shape of the islands is connected to the diffusion of molecules on the substrate. The compactness of an island can be quantified by using a form factor⁴³ $f = \frac{4\Pi \langle A \rangle}{\langle P \rangle^2}$.

The form factor in the case of 50% coverage of T6 on ITO at room temperature deposited at a rate of 0.88 Å/min is $f = 0.28$. Islands on the image border and coalesced islands have been excluded.

The fractal dimension as calculated from the slope of the linear fit of a log-log plot of island perimeter vs island area (ref) yields 1.34 ± 0.06 .

Figure 4.4.3 shows three growth phenomena that can be observed in a film of 50% coverage labelled by roman numbers I, II and III. In region I the nucleation of a second layer was energetically more favourable than a downward transfer of the molecules landing on to of the island. Note that the second layer in its early stage of nucleation is much more dendritic than the islands of the first layer. We conclude that the diffusion on the organic layer is reduced with respect to the ITO substrate.

In general we can assume that all islands of the first layer nucleate at the same time at an early stage and grow subsequently by diffusion and incorporation of molecules from the constant vapour flux. In this so-called aggregation regime, nucleation centers lying close to one another can grow into islands that coalesce like it happens for the regions labelled II. It can be seen clearly in their shape that despite the obtained connection they seem to grow preferably at the side opposite the junction. The reason for this preferred growth is that as islands get closer their so-called capture zones from which they feed start to overlap reducing so the amount of new arriving molecules to incorporate what consequently slows down the growth. The same phenomenon can also lead to confinement of single islands like the one labelled III in the same figure. The size of the confined island is much smaller than that of the surrounding islands. Apart the overlapping of the capture zones also the diffusion towards the smaller island is limited by the confinement. We conclude that even for a homogeneous nucleation in the early stages, big differences in island size can develop during later stages of aggregation due to competing growth and confinement.

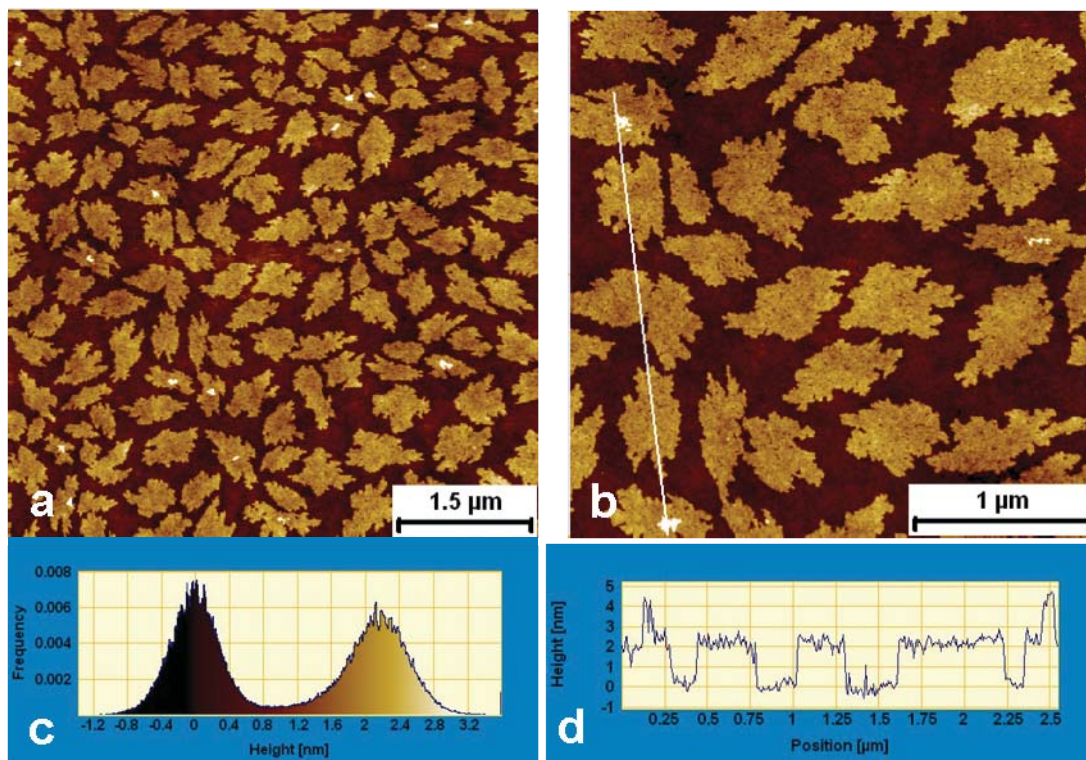


Figure 4.4.2: Non-contact AFM island morphology found on flat ITO (a,b), corresponding height distribution histogram (c) and height profile (d) across first and second layer nucleations in b.

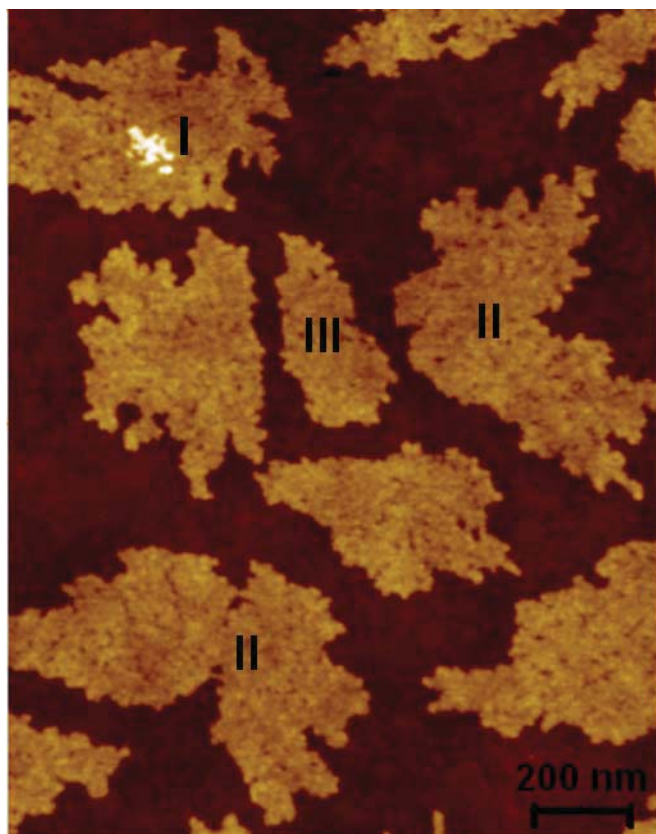


Figure 4.4.3: Three growth phenomena occurring during aggregation in submonolayer films: second layer nucleation (I), coalescence (II) and confinement (III).

In Figure 4.4.4 a detailed view on a single island and the ITO substrate is displayed. We note that both substrate and island exhibit a granular substructure. Taking a closer look at the island substructure we can see point-shaped and more extended vacancy defects. They indicate a reduced packing density that might be caused by the intrinsic surface roughness, defects on the substrate or stress during the growth. It is unlikely that these vacancy defects that reach down to the substrate close during further growth, in contrary they could seed further defects in higher layers. Vacancy defects represent a disruption of the packing order and could therefore cause transport limitations in device applications.

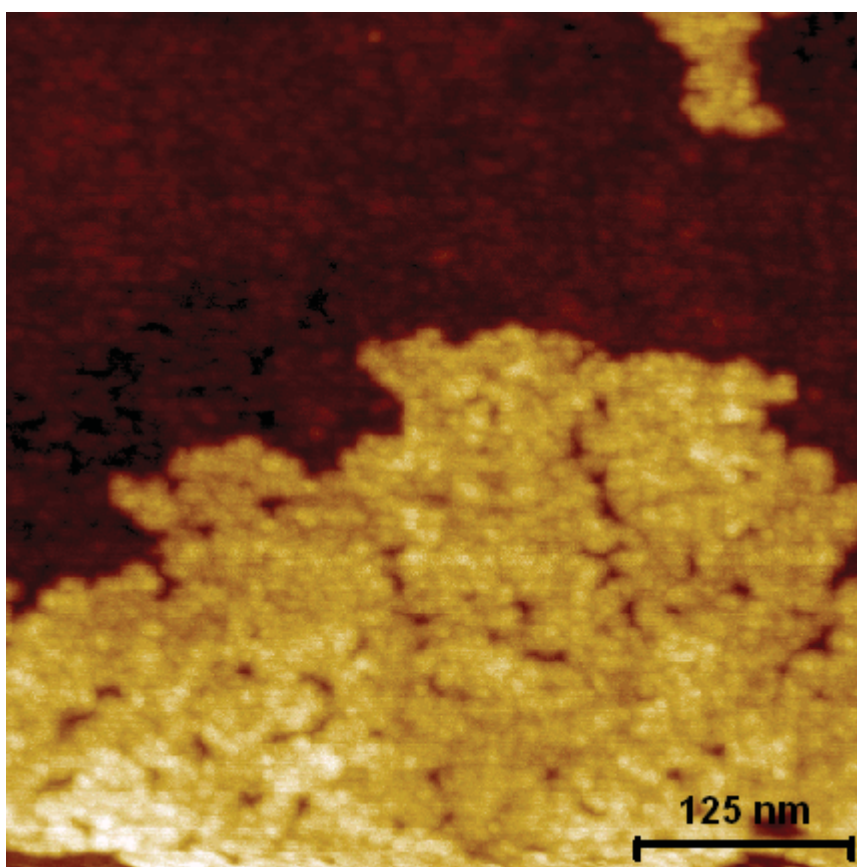


Figure 4.4.4: Island substructure is granular and incorporates many vacancy defect sites.

Besides the importance of investigating T6 on transparent ITO for optical applications, the original idea was to increase the stability of submonolayer organic films for STM measurements. Since ITO is an oxide, sexithiophene molecules form standing islands, similar to what happens on native silicon oxide. Most likely the problem of desorbing molecules in submonolayer films when trying to image the samples in STM is the relative high voltage ($>3V$) applied between tip and sample. This voltage is needed to obtain

tunnelling through the insulating oxide and avoid the tip from penetrating into the organic layer when it approaches to reach the chosen setpoint.

ITO has oxide properties but is conductive, allowing to use lower voltages in STM imaging and being hence less invasive to the weakly adsorbed organic islands. In fact, it is possible to obtain a stable image of the ITO surface covered by T6 islands at STM scan parameters as low as 1.3V with a current setpoint of 20pA. Repeated scanning of the same scan window at these parameters does not alter the morphology what is a clear evidence for non-destructive imaging. Figure 4.4.5a shows an STM micrograph of scan size $6\mu\text{m} \times 6\mu\text{m}$ with rms roughness of 1.25nm, in good agreement with the AFM rms roughness of 1.1nm as determined above. However, the morphology found by STM is very different from the morphology found in the case of NC-AFM imaging, shown for comparison in Figure 4.4.5b. The STM image exhibits a coverage of approximately 70% of mainly interconnected flat islands with clear borders revealing a granular structure of variable height below. Some of the dark pits have an apparent depth of up to 12 nm. When we use the term “apparent height”, we want to stress that the STM height in constant current mode is a combination of the local electronic structure and changes in the real topography. The entire apparent height histogram of the STM image is shown in Figure 4.4.5c. The unimodal distribution is sharp around 0nm which is approximately the height level of the flat islands but there is no sharp distribution for the substrate level as it was the case for the NC-AFM measurement exhibiting a bimodal height distribution (Figure 4.1.5a and c). Consequently we can not determine a reasonable island height from the STM image.

We remember that the AFM image of the same sample showed a coverage of only 50% instead and a homogeneous background. Further the coalesced islands in Figure 4.4.5a display round shapes in contrast to the dendritic islands in Figure 4.4.5b.

At first glance, it is surprising to find such a distinct morphology on the same sample for STM and NC-AFM. In order to justify this discrepancy, it has to be kept in mind that STM does not show the real topography of a sample, especially for organic adsorbates on conducting substrates⁴⁴. By keeping the conductance constant as performed during constant current tunneling mode, the STM image displays the local density of states (LDOS) of the sample. Interpretation of the resulting image as a real topographical

representation is only possible if the LDOS is uniform over the entire sample surface which is here obviously not the case.

The apparent net increase in coverage from 50% to 70% of a $36\mu\text{m}^2$ area on the same sample could be connected to T6 molecules that adsorb in a flat lying configuration in between the standing islands on submonolayer films like found in the case of silicon oxide⁴⁵. Further investigation is needed to fully explain the mechanism responsible for the contrast between islands and surface.

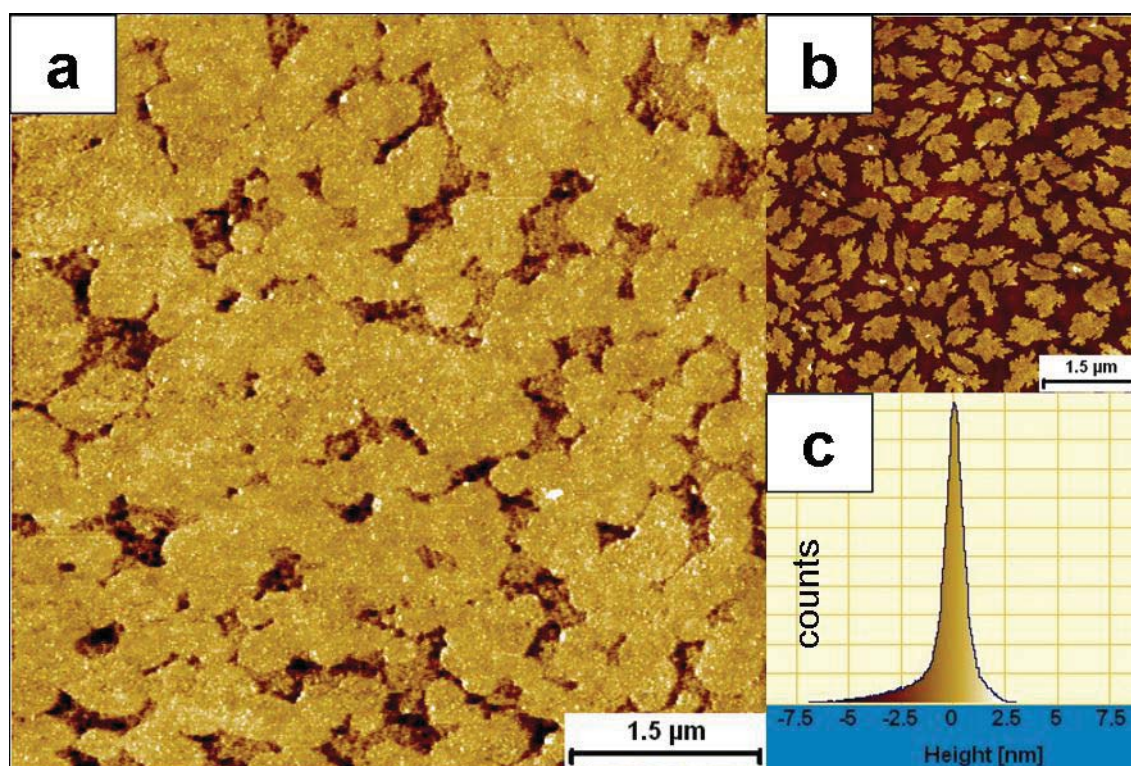


Figure 4.4.5: T6 on ITO imaged by STM (a) at parameters 1.3V, 20pA and the respective height histogram (c). For comparison also the NC-AFM image of the same sample is shown (b).

The coalesced islands exhibit a more homogeneous and flat height structure than the area between them. In Figure 4.4.6 the island substructure is resolved at a lateral scale ranging from 500nm down to 50nm at scan parameters 1.2V and 170pA. The measured rms surface roughness is about 0.48nm and the images clearly show a grain structure with an average grain size of about 10nm. On the 500nm scale we observe a tendency towards directional long range ordering of the grains in domains of close to parallel ripple structures. However these structures are less evident at smaller scan sizes and might therefore be considered scan artefacts. A comparison with the Non-Contact AFM image of

a single island and the substrate in Figure 4.4.4 suggests that the grain structure is likely to be induced by the substrate morphology that despite the lower roughness consists of grains of comparable size. It should be noticed that the structural vacancy defect sides are less evident in the STM measurements than in AFM measurements.

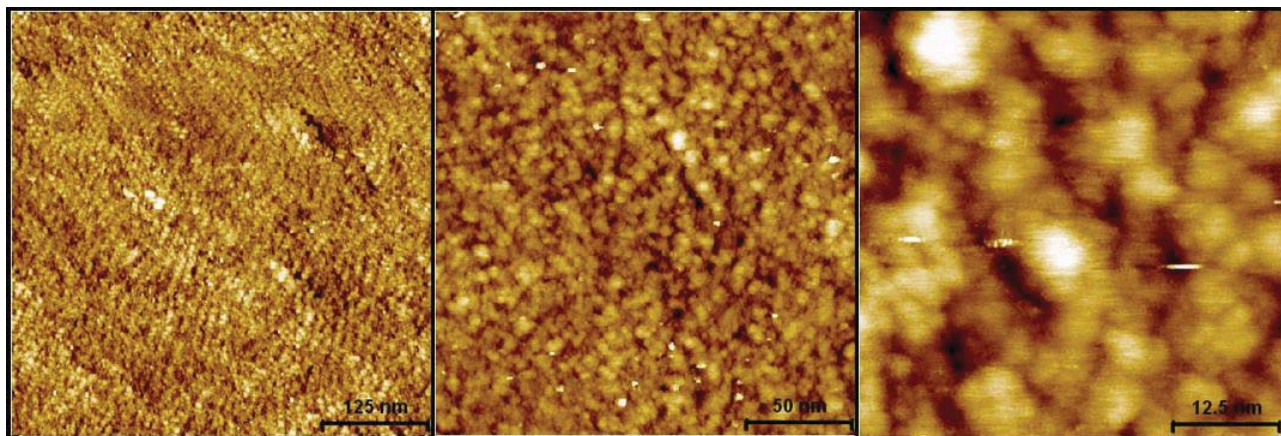


Figure 4.4.6: STM images (1.2V, 170pA) reveal the grain substructure of the coalesced islands.

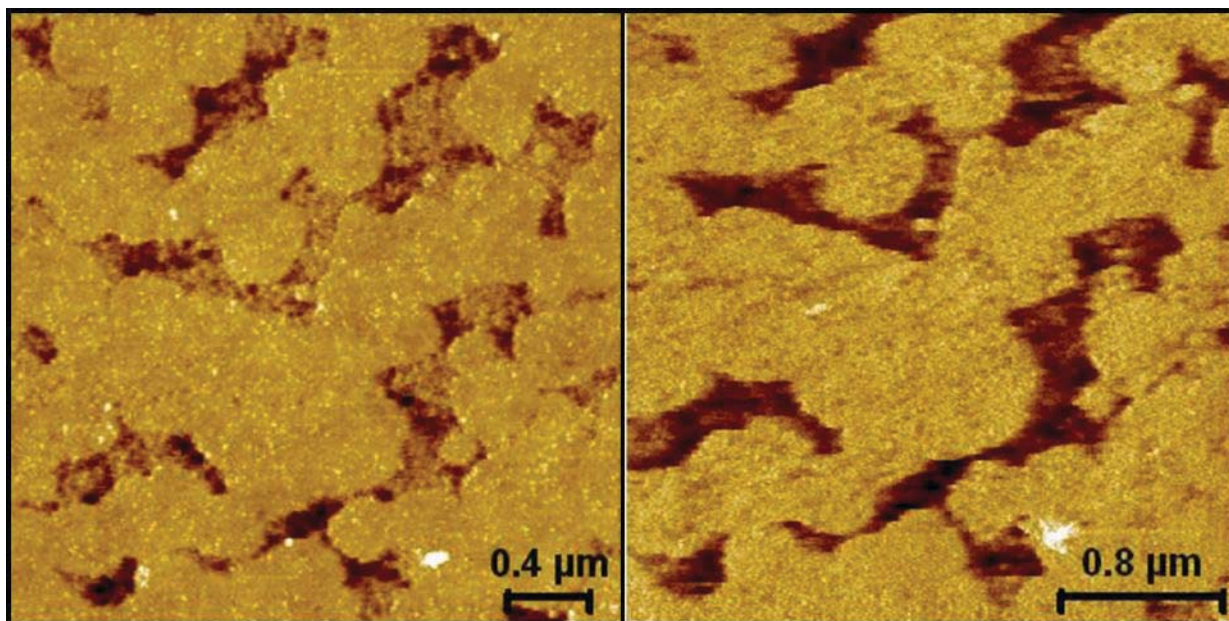


Figure 4.4.7: Comparison between the first STM scan (1.5V, 20pA, left) and a scan (1V, 400pA) after at least 20 measurements and zooms on the image center (right). The island structure is not modified by STM scanning.

As discussed before, AFM and STM reveal a very dissimilar response to submolecular films of sexithiophene on ITO most likely due to inhomogeneous conductivity that leads to a contrast in STM images that does not merely reflect the sample topography. On the more isolating native silicon oxide we observed that the high voltage parameters lead to a modification of the soft and weakly adsorbed organic semiconductor films. Even on

conductive oxides such as ITO islands of standing T6 molecules are formed having their long molecular axis almost perpendicular to the surface. This is characteristic for a dominating molecule-molecule interaction being stronger than the molecule-substrate interaction and resulting in weakly adsorbed films. But on the conductive ITO substrate, STM imaging is less invasive as illustrated in Figure 4.4.7. The left image shows the first STM scan of the pristine film with its structure of coalesced roundish apparent islands taken at scan parameters 1.5V and 20pA. On the right side of Figure 4.4.7 the same area of the film is shown at scan parameters 1V and 400pA after at least 20 scan frames of different size down to the nanometer range, in particular the images shown in Figure 4.4.6 were taken on the large island in the center. No scan-induced desorption or reorganization of the coalesced islands in Figure 4.4.7 is noticeable and the shapes of the islands is not altered. Merely, the contrast between apparent islands and substrate is enhanced and more homogeneous in the right image, giving a value of about 6nm as an estimate for the apparent island height. This value can not be associated directly with a real world morphological feature since it refers only to the apparent height of a heterogeneous sample. Moreover the molecule dimension (2.7nm) and the coverage determined by AFM (50%) can not explain such an apparent height at high coverage. It is important to notice that the obviously improved contrast emerges at lower applied voltage and higher current setpoint. Both changes in the parameters favour the tip to get closer to the sample searching for a higher current at a lower bias voltage. We can infer from this observation that the area between the coalesced islands must exhibit a lower conductivity with respect to the coalesced islands leading to an increase of the apparent height.

4.5. Pentacene and perylene on device testpatterns

Organic semiconductors have been extensively studied on both oxides and metal surfaces. In fact, it is essential for future applications to understand their structure on both dielectric and conductive substrates since in real world electronic devices the organic semiconductors are employed as functional layer deposited on or sandwiched between metal electrodes and potentially separated by dielectric regions depending on the functionality of the device.

In fundamental research one of the main targets is to elucidate the principal mechanisms that control the order at interfaces and consequently the electronic properties. Ideal samples and complex surface preparation techniques are frequently used such as single crystals of metal, prepared by various cycles of sputtering and annealing in UHV.

However these perfect metal surfaces are rather expensive, unpractical and unsuitable for device applications. Therefore it is important to concentrate more effort on the investigation of the far less ideal organic devices. The gold electrodes employed in devices usually consist of high vacuum evaporated polycrystalline gold films of several hundred nanometers. To favour a better adhesion the gold deposition is commonly preceded by precursors like chromium or indium tin oxide.

In this chapter, two model organic semiconductors, namely pentacene and perylene (PDI 8CN2) have been deposited on bottom contact OFET testpatterns. A schematic representation of the OFET testpatterns is shown in Figure 4.5.1. The testpatterns were fabricated by the Fondazione Bruno Kessler in Trento, Italy and consist of a highly n-doped silicon substrate with 200 nm of thermally grown silicon oxide on top. The polycrystalline gold electrodes and wires are about 100-150 nm thick and are defined by a lift-off technique on top of the oxide. A thin layer of chrome (3-5 nm) is used as adhesion layer for the Au structures. The top view of the test pattern (Figure 4.5.1b) identifies the layout geometry showing four interdigitated FET electrodes. Pentacene and perylene were evaporated in high vacuum directly onto the test patterns up to a nominal thickness of the organic films of about 10 nm, monitored by a quartz balance. After being exposed to air, the gold electrodes have been short circuited and contacted to the sample plate using silver paste in order to allow for STM measurements on the interdigitated gold structures. The measurements were carried out in UHV.

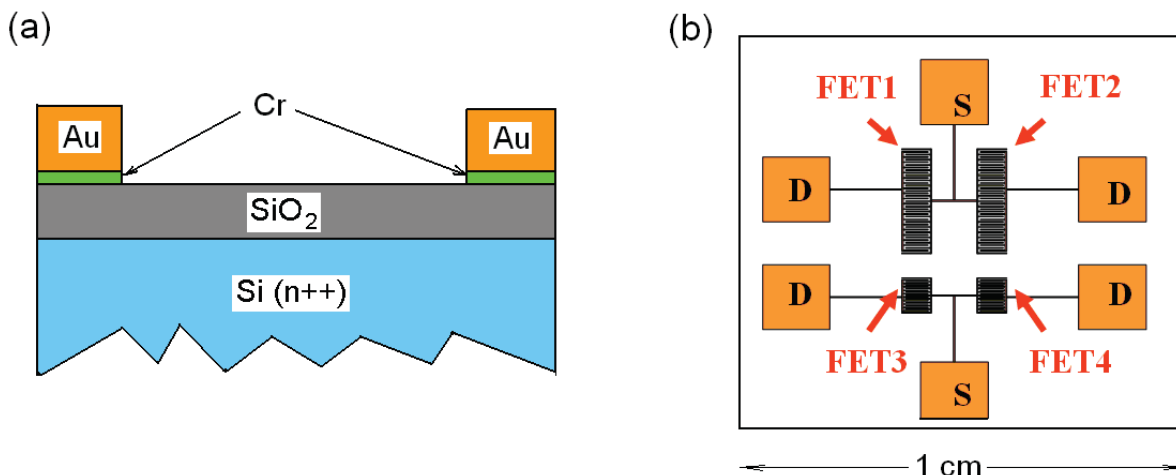


Figure 4.5.1: (a) Schematic representation of the cross section of the OFET test pattern; (b) Top view of the test pattern layout showing four interdigitated FET structures with corresponding source (S) and drain (D) pads (courtesy of Dr. Arian Shehu).

In Figure 4.5.2 we show exemplarily four distinct morphologies of pentacene films found on the testpattern gold structures using STM in constant current mode. About 7.5ML of pentacene have been deposited on the testpattern. The region chosen for the STM measurements were the interdigitated FET structures in which gold and oxide zones alter in stripes of 40 μm (FET1, FET2) and 20 μm (FET3, FET4).

On the thermal oxide regions even at high voltages and low setpoint currents (10V, 10pA), no STM imaging was possible. As a consequence of low conduction for the current path from the electrodes to the tip, it penetrated into the organic film in search for the setpoint on the highly isolating 200 nm oxide.

On the polycrystalline gold stripes instead imaging was possible at rather low voltages and currents (1V, <100pA). Figure 4.5.2A and B show structures found at a image size of several microns but still of very distinct type. Figure 4.5.2A shows mainly grains of micrometer extension with some straight borders reminiscent of crystalline organization but in general rather faint substructures in the grains. Further we can identify some smaller islands at the image bottom. This suggests a coverage by organic material in the imaged area.

Figure 4.5.2B instead shows a dense network of roundish apparently flat grains and elongated step structures. It should be noted that the grains are much smaller and more defined than in Figure 4.5.2B. Only at the top of the image the traced structures become fainter and less defined. The morphology remains the same during several consecutive upward and downward scans what excludes an attribution of the top image inarticulation due to tip induced artefacts for example by picking up organic molecules. On this scale is

appears that pentacene adsorption on the polycrystalline gold electrodes of the testpattern is not homogeneous at the given nominal coverage of 7.5ML.

Figure 4.5.2C and D show STM morphologies in the submicron range in different zones on the polycrystalline FET contacts. Figure 4.5.2D shows similar terrace structures as in Figure 4.5.2B at higher magnification. However, an important difference in the magnified image is the presence of nanometer-sized droplets on and between the terraces some of which appear coalesced into larger droplets. It is unlikely that these structures form during the fabrication of the polycrystalline gold contacts and therefore we suggest they consist of pentacene. Further it is conspicuous that some of the gold terraces exhibit noisy substructures that is likely to originate from adsorbed pentacene molecules.

Figure 4.5.2C is probably the most evident observation of a selective adsorption of pentacene on the submicron scale. While at the image bottom we identify elongated grains with undefined borders, the upper half of the image shows nicely defined flat gold grains in layers revealing even lower level layers between the grains. These lower level gold layers are not visible in the lower image half that further exhibits streaking noise which is a clear evidence for mobile molecular species. Repeated scans on the same area show always the same morphology as shown in the figure. The evident height difference between the upper and the lower image half could be associated to the decrease in tunnelling current when the tip passes over the zone with adsorbed pentacene molecules. In order to keep the current setpoint constant, the tip-sample distance is smaller over the region with adsorbed pentacene than over the gold grains what could contribute to an increase of the apparent height.

The above reasoning based on the different morphologies found by STM investigations on the testpattern contacts leads to the assumption that on the so far examined scale the adsorption of pentacene in multilayers is not homogeneous.

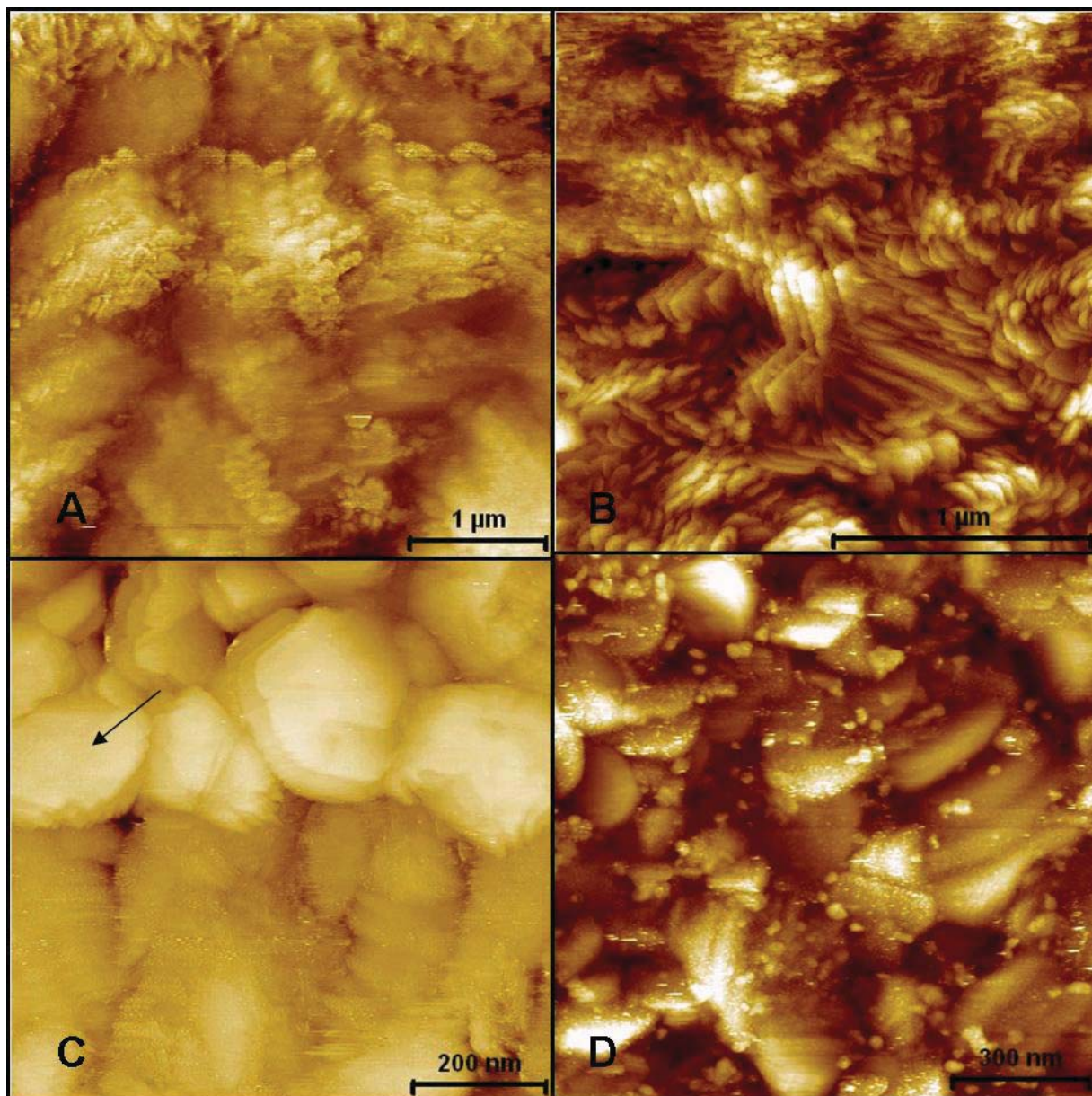


Figure 4.5.2: Examples for different morphologies found on test pattern gold contacts with 7.5ML of pentacene. The flat grain in (C) marked by an arrow will be investigated more in detail later.

In the following we will focus on the detailed structure of a single flat grain. The investigated zone is evidenced by a black arrow in Figure 4.5.2. The flat large gold grain on the testpattern electrode shown in Figure 4.5.3 allows high resolution STM of the flat adsorbed pentacene adlayers on the Au (111) terraces. Figure 4.5.3C shows parallel rows of flat lying pentacene.

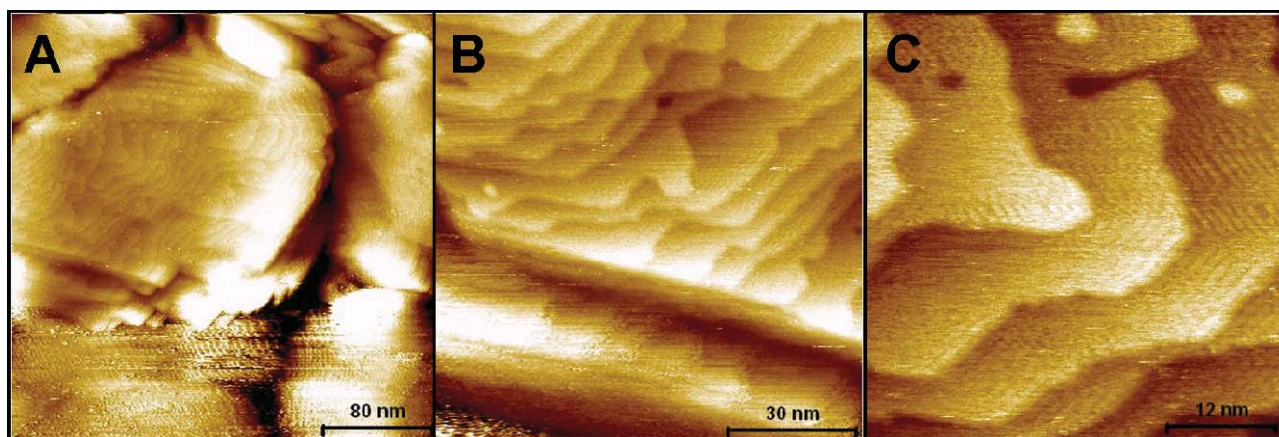


Figure 4.5.3: (A) Several hundred nanometers large gold grain of Trento-type TP electrode with terraces in STM. (B) Magnification of stepped surface structure revealing parallel rows. (C) Molecular rows of flat lying 6T molecules adsorbed to the flat gold terraces.

Figure 4.5.4 shows a high resolution STM image obtained on a 10 nm thick film of the organic semiconductor perylene PDI8CN2 deposited onto a testpattern (Trento-type) and later introduced into the UHV STM. The micrographs display parallel molecular rows with structural vacancy defects.

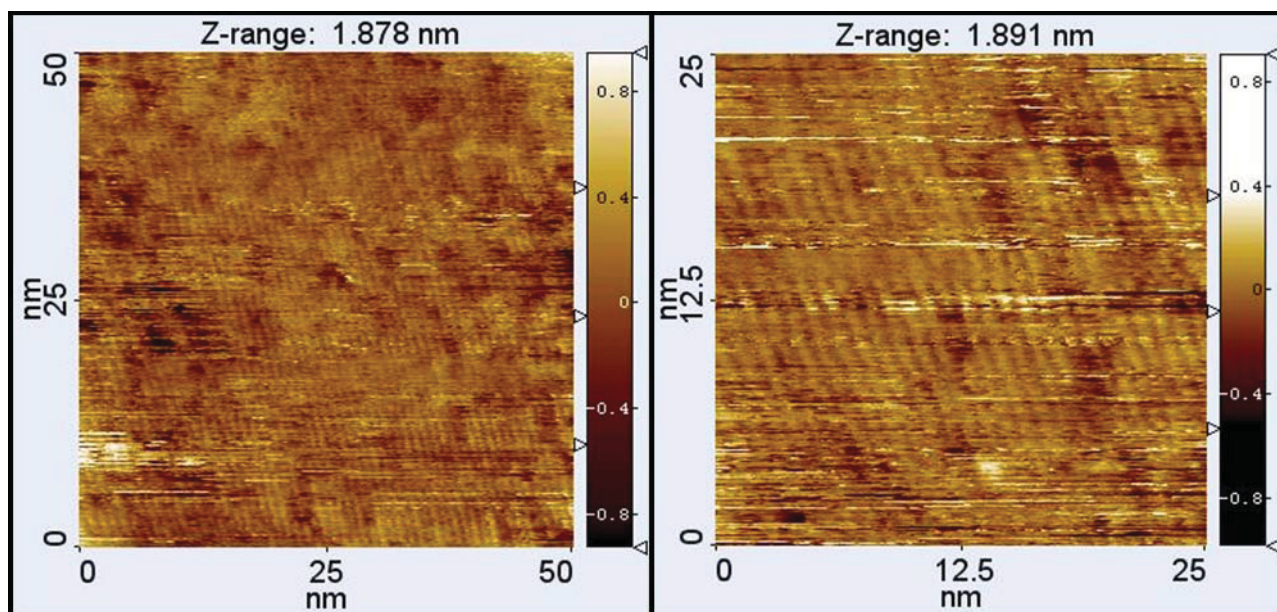


Figure 4.5.4: Molecular row structure found on 10 nm thick perylene PDI 8CN2 films on polycrystalline gold electrodes of the Trento-type test pattern. Structural defects like vacancies and protrusions are evident. The row distance has been determined to 0.95 nm by FFT image analysis.

5. In-situ real-time morphology evolution of 6T on native silicon oxide at variable temperature

5.1. Motivation

In-situ and real-time investigation techniques are increasingly getting accessible to the scientific community and allow unprecedented insights into complex dynamic physical, chemical and biological processes that can not simply be unravelled by common ex-situ measurements that employ the same investigation techniques. Many technically relevant molecular scale systems, like for example the growth of organic semiconductors by Organic Material Beam Deposition (OMBD) in Ultra High Vacuum (UHV), are out-of-equilibrium processes that need to be better understood in order to achieve a reproducible and reliable downscaling of micro- and nanoelectronic devices.

The present work is to our knowledge the first real-time in-situ AFM study of the growth process of organic semiconductors during deposition. Other real-time in-situ investigation methods that have so far been reported and were applied to investigate dynamic processes involve X-ray scattering, AFM in liquid, photoelectron spectroscopy, X-ray adsorption spectroscopy and electrical characterization of OFETs [46].

Scanning probe techniques applied to in-situ real-time experiments are of particular interest since they provide a real space insight into dynamic processes at surfaces in localized areas down to the nanometer scale. Further are SPM techniques complementary to above mentioned implemented in-situ real-time techniques that average the measurement observable over larger areas. The only SPM technique that has so far been applied to elucidate the dynamics of growth phenomena in UHV uses a custom-built STM [47] combined with Molecular Beam Epitaxy (MBE), however the group's investigations concentrate to date on the growth of inorganic semiconductors.

The most prominent example of a real space real-time in-situ investigation of the growth evolution of organic semiconductors employed photoelectron emission spectroscopy to study the growth of pentacene on silicon oxide. [48].

5.2. Experimental

The experiments were carried out using a VT-UHV AFM/STM XA series (Omicron Nanotechnology GmbH, Germany) equipped with an organic effusion cell (Dr. Eberl, Germany) that has been designed for OMBD directly on the sample during the SPM measurement. In this study we used exclusively Non-contact AFM to monitor the film evolution. Some of the key features of the experimental setup include a reliable, low thermal drift tip positioning system, a variable temperature sample stage (50-500K) connected to an external feedback loop and a high thermal inertia with precise temperature control of the water cooled effusion cell to guarantee for stable and reproducible deposition rates. The thoroughly outgassed effusion cell was loaded with Sexithiophene (6T) purchased from Sigma Aldrich which was then purified by several depositions in UHV prior to data acquisition. The UHV system's base pressure at room temperature is in the range of 10^{-9} mbar and rises about one order of magnitude to 10^{-8} mbar during deposition.

All native silicon oxide substrates were manually cut from the same wafer (n-type, phosphorus doped, resistivity $\sim 10\Omega\text{cm}$, IMM Bologna), glued to the sample plate using silver paste and introduced into the vacuum chamber without further cleaning. Prior to deposition the samples were kept for several hours at their respective target temperature to assure a homogeneous sample temperature and degas silver paste and substrate. As sample temperatures during deposition we used five different values ranging from room temperature to 120°C , namely 25°C , 50°C , 80°C , 100°C and 120°C .

In order to capture the dynamics of local growth of sexithiophene in ultrathin organic films at different substrate temperatures, an unprecedented quasi real-time AFM measurement during growth is employed. In this approach a deposition interval of 5 min at an approximate deposition rate of $1 \text{ \AA}/\text{min}$ is immediately proceeded by an AFM measurement interval of about 30 min. During the AFM measurement, the molecular beam is blocked by a cell shutter what allows us to visualize a static image of the submonolayer growth process after the first deposition. When the static image is acquired, the tip is retracted to a sufficient distance in order to prevent shading of the molecular beam and the second deposition interval begins. The iteration of this process up to a thickness of several monolayers is a powerful investigation tool. It yields a detailed step-by-step sequence of

the local growth process in quasi real-time for the SiOx/6T and the 6T/6T interfaces and elucidates the dynamics at different substrate temperatures in real space.

Both deposition rate and substrate temperature have been widely proven to be the crucial parameters that determine growth phenomena of organic semiconductors (cite Pratontep). The flux of the molecular beam is kept constant and reproducible by fixing the effusion cell temperature in all experiments to 260°C⁴⁹. Unlike in conventional organic growth systems, the deposition rate is not monitored by a (cooled) quartz microbalance in our setup but is determined more precisely by measuring the effective coverage at the respective substrate temperature by Non contact AFM after each deposition. The effective deposition rate usually stated in Å/min is calculated from the coverage using the known layer thickness of about 2.4 Å corresponding to the upright standing molecular configuration found on silicon oxide (cite) . This indirect measure of the effective deposition rate takes into account the real adsorption that depends on the surface properties, a temperature dependent sticking coefficient and possible reevaporation from the hot sample surface.

5.3. Results

We show here as an example two selected growth sequences, the detailed $1\mu\text{m} \times 1\mu\text{m}$ evolution at 50°C substrate temperature in Figure 5.3.1 and the $6\mu\text{m} \times 6\mu\text{m}$ sequence at 100°C in Figure 5.3.2.

The sequences for further temperatures and the respective sequence images mounted into AFM growth movies can be found as supporting online material.

[\http://dl.dropbox.com/u/4320018/sequence.zip

<http://dl.dropbox.com/u/4320018/movies.zip>].

Figure 5.3.1 shows 12 consecutive AFM scans starting with an overview of the pristine native silicon oxide surface (top left) where the white square evidences the area monitored during the following deposition process. The sequential AFM micrographs are chronologically ordered from left to right and from top to bottom showing the stepwise film evolution up to 2.24 ML (bottom right). After each image 5 min of 6T deposition is carried out corresponding to a coverage increase of about 0.2 ML.

We notice a pronounced drop of the nucleation density from the first layer nucleation to the second and third layer nucleation that is ascribed to the different nature of the nucleation substrate. While the first ML aggregates on a silicon oxide surface, higher layers nucleate on an organic adlayer of standing 6T molecules and increasing thickness. Further we notice a shape transition towards more dendritic island borders for islands that nucleate on 6T. In earlier studies on organic semiconductor growth, a shape transition from roundish to dendritic has been associated with a reduced diffusion time and diffusion length. A change of the molecular dynamics is reasonable since the silicon oxide interface is increasingly screened by the organic monolayers.

However the history of preceding nucleation substrate is not completely lost. We can clearly see how the early 2nd layer nucleations that emerge in early stages of deposition at 50°C (see Figure 5.3.1, first row) favour the incorporation of new arriving molecules into second layer islands (see Figure 5.3.1, second row) although the first monolayer is not completely closed yet. The trend towards a so-called 3D growth mode where islands of higher layers nucleate before the completion of the underlying layer gets even more pronounced for the nucleation of the 3rd, 4th and 5th layer. The 3D growth mode is Stranski-Krastanov-like (layer-plus-island) and is in contrast to a perfect layer-by-layer growth (also known as Frank-van-der-Merwe growth mode).

Obtaining a perfect layer-by-layer growth especially for the first few monolayers at the dielectric interface is considered a basic requirement for good OFET device performance since it provides the best island interconnection.

The here presented localized tracing of organic semiconductor growth allows new insights in the origin and evolution of defects in the single molecular layers and the effect of substrate temperature on the growth mode. The scan sequence shows clearly that the occurrence of 2nd layer nucleations at submonolayer coverages favours a premature evolution of the 2nd layer islands and avoids the complete closing of the first ML even at a final coverage of 2.24ML. Further is the presence of multiple nucleations of higher layers (2-5) in the vicinity of the early 2nd layer nucleations conspicuous and might originate from defects on the silicon oxide. However, the overall dominating Stranski-Krastanov pyramidal pile-up at 50°C substrate temperature suggests that (a fraction of) the molecules that land on top of the highest islands do not have enough energy to overcome the Ehrlich-Schwoebel barrier [50, 51] and consequently descend to incorporate into uncompleted lower layers.

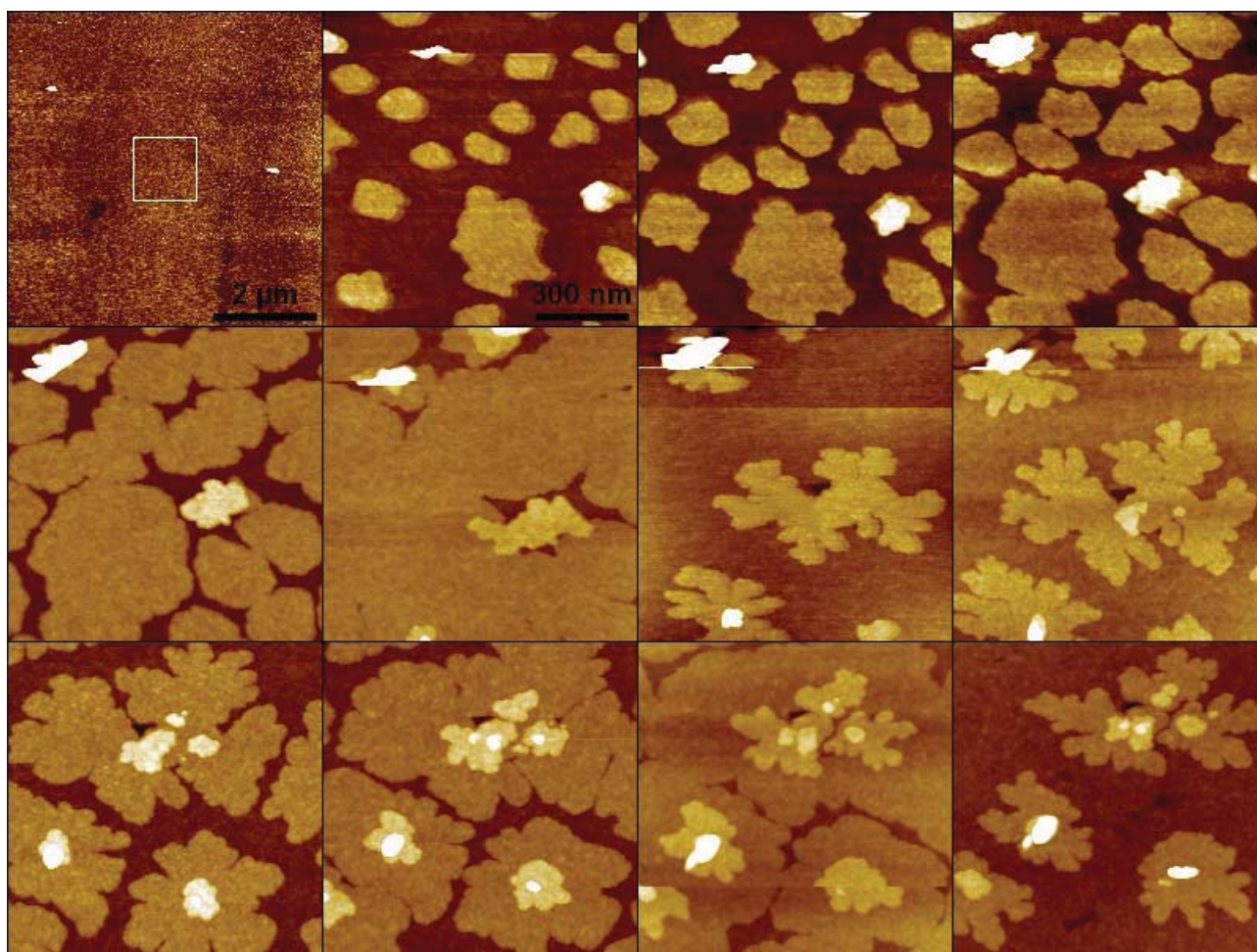


Figure 5.3.1: Each micrograph is part of the stepwise evolution of the first 2.5 ML of 6T islands at 50°C. The order of the sequence is from left to right and up row after row.

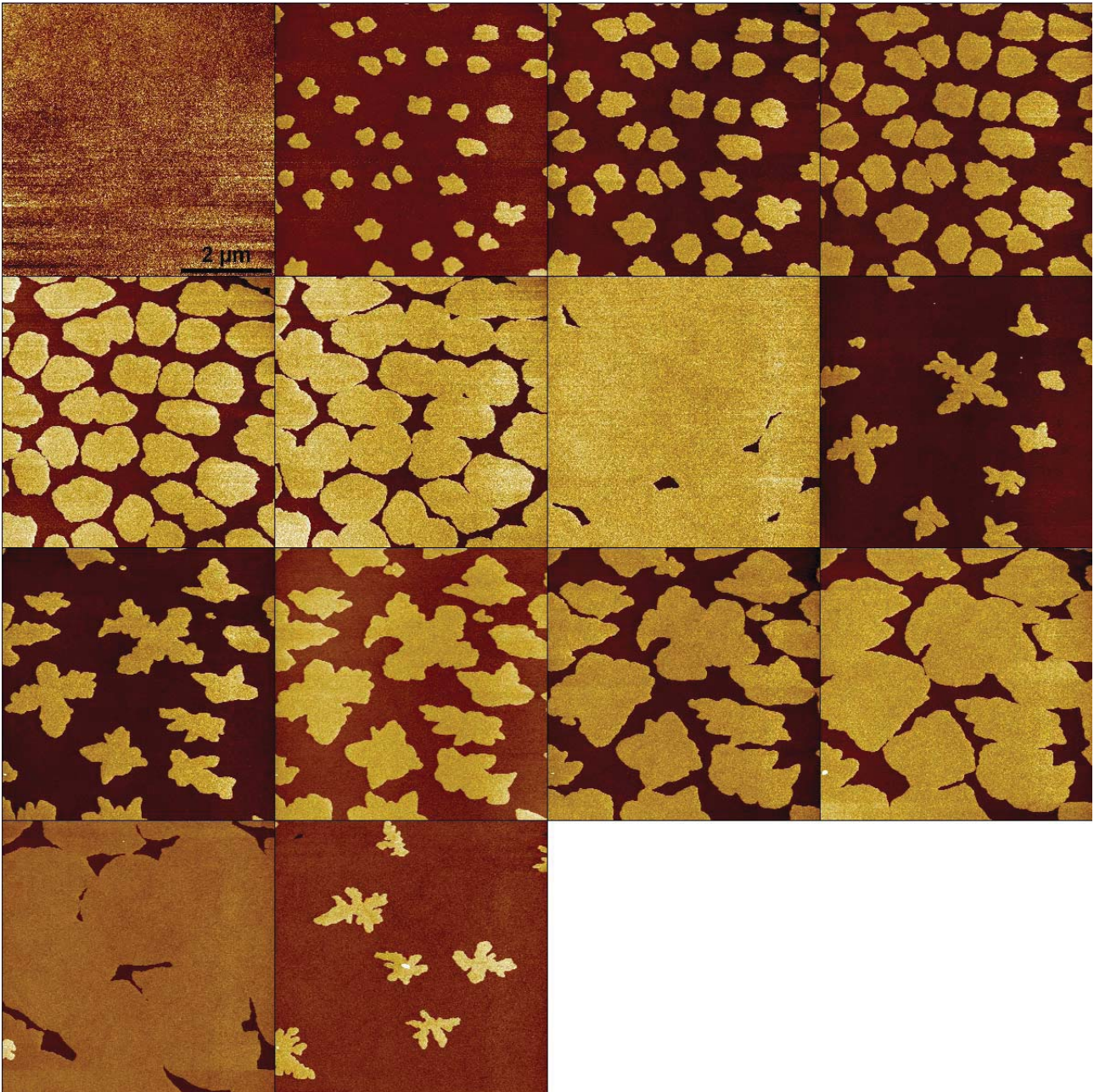


Figure 5.3.2: Stepwise morphological evolution of 6T islands on native silicon oxide at 100°C substrate temperature.

In fact, if we perform the same real-time in-situ growth experiment at a higher substrate temperature like shown in Figure 5.3.2 (here 100°C) a perfect layer-by-layer or Frank-van-der-Merwe growth is found.

Up to a total coverage of about 2.1 ML, again reached in steps of 5 min of deposition (corresponding to 0.15 ML in coverage each) followed by immediate AFM imaging, at no stage nucleations of layers beyond the currently completing ML are observed.

Referring to our earlier argumentation on nucleation favouring oxide defects and Ehrlich-Schwoebel barriers, in this case the thermal energy that is provided to the molecules landing on the sample is most likely high enough to avoid 3D nucleation modes.

Again we observe an island shape transition from roundish to dendritic in accordance with the change in the underlying silicon oxide and 6T nucleation substrate. Further it is noteworthy that the 2nd layer dendritic islands exhibit a tendency towards two perpendicular main axes and consequently 4 main branches in an early nucleation stage. While the first layer shows a homogeneous nucleation with no large deviations from the mean island size, the second layer exhibits large differences in the island sizes that are attributed to a heterogeneous nucleation. Apart a clear evidence for not contemporaneous nucleation, competition and confinement are believed to effect the diffusion on the surface slowing down the ripening process for some islands and increasing the size differences. However the initially dendritic islands gradually evolve into more roundish islands, filling in the empty spaces between the branches rather than extending the branches. Eventually the islands coalesce forming a closed layer.

The third layer islands appear much more branched than the second layer islands. This shape difference could indicate a layer dependent diffusion length at low coverages. A more pronounced branching is associated with a reduced diffusion length.

An important new outcome of the real-time growth experiments at five selected substrate temperatures ranging from 25°C to 120°C and at constant flux of molecules is the clear emergence of a substrate temperature dependent effective growth rate. This effect has to our knowledge never been experimentally observed.

Unlike in conventional organic growth systems, the coverage is not monitored by a (cooled) quartz microbalance in our setup. Rather the surface coverage is directly measured on the sample at the chosen substrate temperature by NC-AFM after each deposition interval of 5 min.

The flux of the molecular beam can be considered constant, since the cell temperature is kept accurately at 260°C for all depositions and the deposited quantities are very low (< 3ML) ruling out significant variations in the flux due to a substantial decrease of the crucible material.

In order to illustrate the rate dependence on the substrate temperature, we define the effective growth rate as the amount of organic material growing effectively on the substrate per time at the given constant temperature. It is quantified much more precise directly by the AFM images taken after each growth step and not as usual by a reference measure on a different surface at a different temperature and different position (e.g. by a cooled microquartz balance).

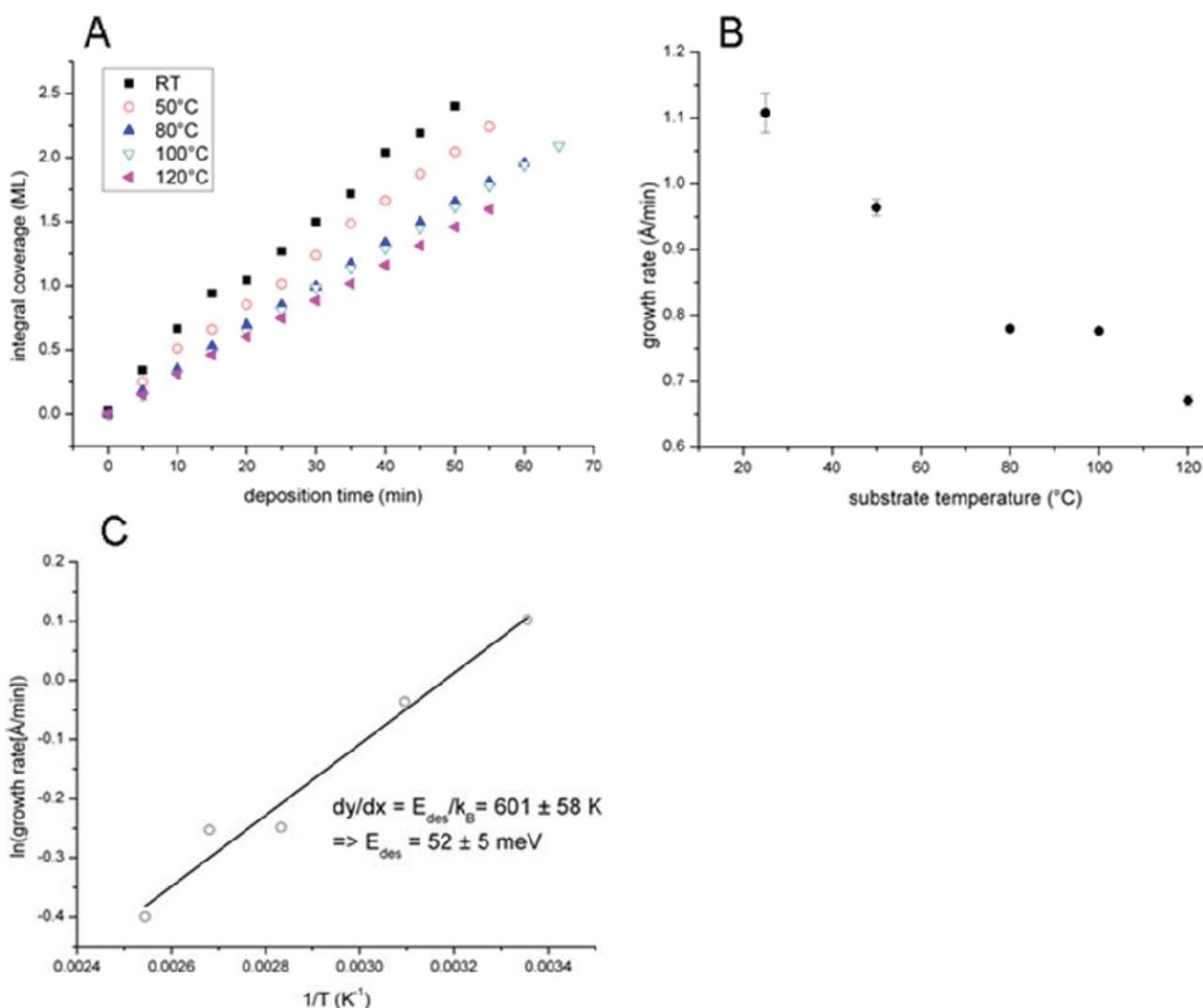


Figure 5.3.3: Integral coverage monitored after each growth step vs time (A), effective growth rate (B) and an Arrhenius-type plot of the growth rate (C) that yields a desorption energy estimate of $52 \pm 5 \text{ meV}$.

In Figure 5.3.3A we show the integral coverage evolution in time for five different substrate temperatures. For each substrate temperature all data points lie on a straight line what confirms again the constant molecular flux at the cell temperature of 260°C. With rising substrate temperature the slope of the decreases corresponding to a reduced effective growth on the substrate. We attribute this monotonic decrease to a reduced sticking or rather increased redesorption on the hot sample surface. The effective growth rate is determined by definition from the linear slope of the integral coverage vs deposition time and is shown in Figure 5.3.3B vs the respective substrate temperature. The effective growth rate decreases monotonic from about 1.11 Å/min at room temperature where redesorption effects are negligible to almost half its value of about 0.67 Å/min at 120°C substrate temperature.

We estimate hence the T6 desorption energy from a Arrhenius-type plot and a linear fit shown in Figure 5.3.3C and obtain 52 ± 5 meV corresponding to the thermal energy at 601 ± 58 K. A complete desorption of ultrathin films of T6 on native silicon oxide could be experimentally verified by XRD reflectometry at ESRF at this substrate temperature by post deposition annealing experiments

Notably lowered rates were reported to increase the domain size and therefore decrease the island density at constant substrate temperature (cite pratontep). However, the overall decrease of the effective deposition rate at elevated temperatures is too small to induce articulated rate dependent variations in the island density.

The changes in shape, fractal dimension, correlation length and nucleation density of the first and second layer islands are rather determined by the substantial differences in substrate temperature and hence diffusion energy. A comparison of the first and second layer nucleation at comparable coverages of approximately 0.2ML (in the so-called aggregation regime) is shown in Figure 5.3.4.

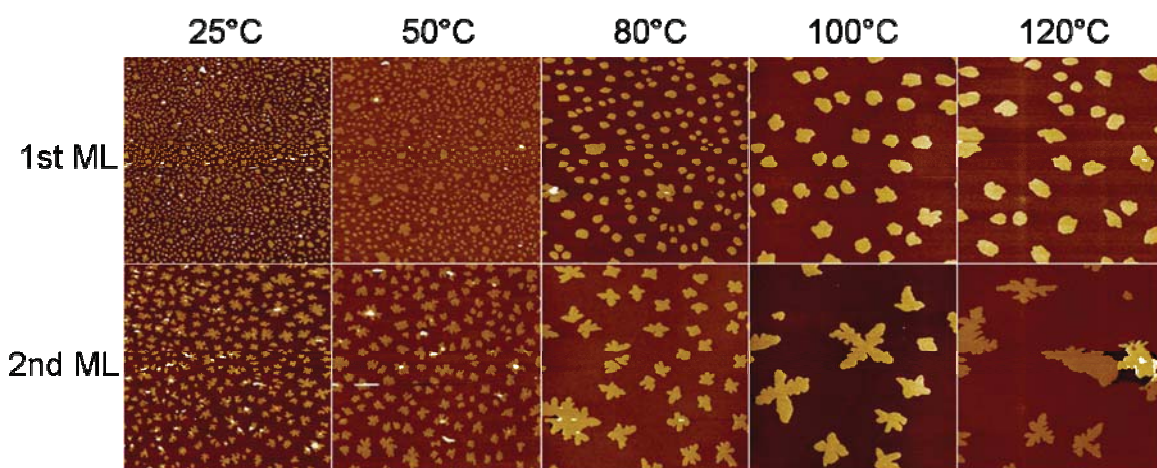


Figure 5.3.4: Comparison of the first and second layer nucleation at different substrate temperatures and coverages of about 0.2ML.

A lower nucleation density can be associated with an eased diffusion of the molecules on the surface and therefore we expect a decrease in the nucleation density with rising substrate temperature. Figure 5.3.4 confirms this trend as a clear decrease of the number of nucleations both in the first and second monolayer with rising substrate temperature is evident. In addition a clear decrease in nucleation density in the second monolayer occurs in the second layer with respect to the first layer at a given temperature and hence thermal energy. We deduce that the diffusion of sexithiophene is better on a completed layer than on the bare silicon oxide surface. This observation is not as trivial as one could expect as the very similar rodlike molecule para-sexiphenyl (p-6P) was recently reported to show an increase in the island density in the second layer that was associated with a hindered diffusion⁵² in contrast our results for 6T.

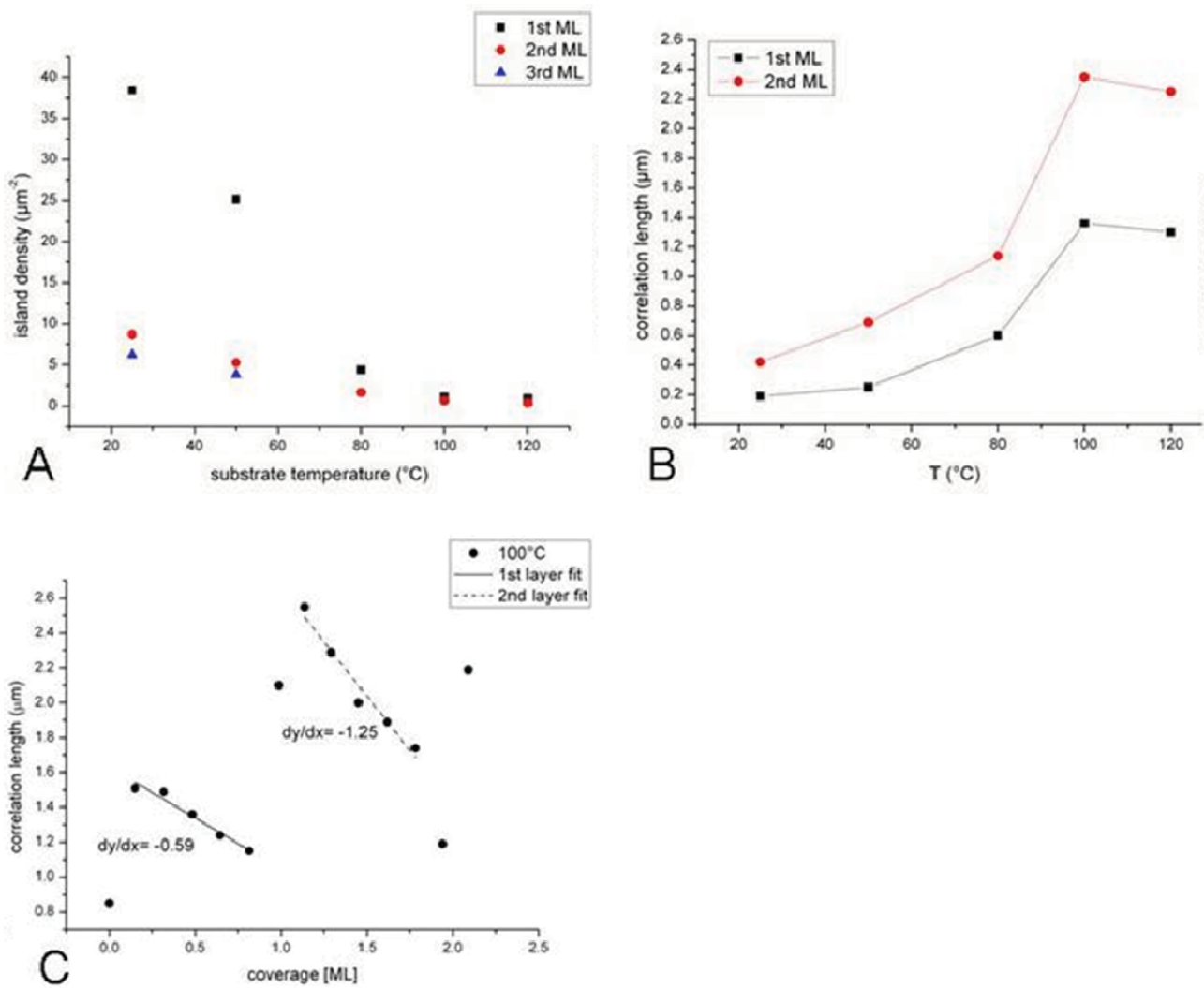


Figure 5.3.5: (A) Nucleation density for the first 3 layers as a function of temperature. (B) Correlation lengths for the first 2 layers as a function of temperature. (C) Correlation length evolution during deposition at 100°C (see Figure 5.3.2).

Figure 5.3.5A summarizes a quantitative graphical representation of the nucleation density for the early stages of deposition shown in Figure 5.3.4. For the first monolayer a drastic almost linear decay was observed up to 80°C. This trend does not continue above 80°C. The island density decreases much slower and seems to converge towards a constant value of about 1 island per μm^2 . For the second monolayer the island density is much lower at room temperature but has an almost linear, yet less pronounced, decrease up to 80°C in common. Besides the relative large absolute difference at low temperatures, the nucleation densities for the first and second layer converge for high temperatures. The third layer nucleation density does not vary substantially for low temperatures indicating a common nucleation mechanism on top of organic layers that is however distinct from the mechanism on bare silicon. The differences are more pronounced at low substrate

temperatures where the lower thermal energy limits the diffusion of molecules on the surface.

In Figure 5.3.5B we plotted the spatial correlation length for the first two layers in function of the substrate temperature that has been determined from power spectrum density transform of the AFM images using a method described in (PRB BISCARINI). As expected the second layer islands exhibit a larger correlation length at all substrate temperatures underlining again change of diffusion on the completed organic layer. However, the first and second layer correlation length between the islands follow the same exponential trend that tends to saturate above 100°C. Although island densities (averaged over the entire scan window) converged for the highest temperatures, the correlation length of the second layer is about two times larger.

In Figure 5.3.5C we show the evolution of the correlation length throughout the deposition with respect to the integral coverage. The depicted values are calculated from the image sequence at 100°C shown earlier in Figure 5.3.2. Both first and second layer evolution can be fitted by a straight line. As the islands increase in size, the correlation length decreases. Although the (effective) growth rate is kept the same, the correlation length decreases at about double the speed for the second layer islands. This is a further evidence for the distinct formation dynamics of the first and second layer that are attributed to the change in surface energy and hence the distinct diffusion of molecules on silicon oxide and an organic monolayer.

6. Real-time in-situ deposition on technological OFET testpatterns

In this chapter we apply the in-situ real-time deposition technique with combined NC-AFM surface morphology measurements to technological OFET testpatterns. The aim of this study is to visualize the growth process of OMBD Sexithiophene close to the electrode or comprising the whole channel region on a 100°C hot testpattern. The growth mechanisms and dynamics at the vertical interface between the polycrystalline gold electrodes and the thermal siliconoxide channel are crucial for charge injection and performance of organic transistors and are so far little studied, not least because it is difficult to access the interface with suitable investigation techniques.

NC- AFM combined with low rate in-situ 6T sublimation provides a stepwise overview on the morphological evolution on the gold electrode, on the SiO_x channel and the direct interface from submonolayer coverages to several monolayers of active organic material. The great benefit for unravelling growth mechanisms on complex substrates is the high precision and reliability of the tip positioning system, even at 100°C substrate temperatures allowing to image the same sample region on a micron scale and follow its evolution.

Much more common than real-time growth investigations starting from organic submonolayers and ultrathin films (REF ARIAN SANTI) are static measurements of morphology and device performance (transfer curves) on one-shot deposited films ranging from 20 nm to several hundred nanometer thickness where good electrical connection is assumed. However it has been found (REF) that only the first few monolayers at the channel interface contribute to charge transport why we performed this study.

Figure 5.3.1a shows the morphology of a Fraunhofer testpattern with a channel length of 5 μm at a pentacene film thickness of about 20 nm. Both source and drain electrodes show pyramidal islands with a higher nucleation density than inside the channel. Figure 5.3.1b shows a magnification of the center channel region and a respective height profile in Figure 5.3.1c across the white line in Figure 5.3.1b confirming the presence of pyramidal terraces. Figure 5.3.1 shows a schematic representation of a polarized OFET with a magnification of the first layers of upright standing molecules that favour charge transport from source to drain parallel to the surface.

The testpattern structures used in this chapter have been introduced and characterized in chapter REF. In Figure 5.3.2 a direct comparison of the Trento type testpattern and the

Fraunhofer type testpattern is shown. The main differences are the employed gold adhesion layer, the native oxide thickness and the electrode height.

NC-AFM in UHV is very sensitive what causes experimental problems when the imaged region includes a large height range as a monitoring of the vertical gold/oxide interface requires. The use of high force constant cantilevers improve the measurement stability. However, both resolution and measurement stability increase on the only about 30 nm high Fraunhofer gold pads with respect to the about 150 nm high Trento electrodes.

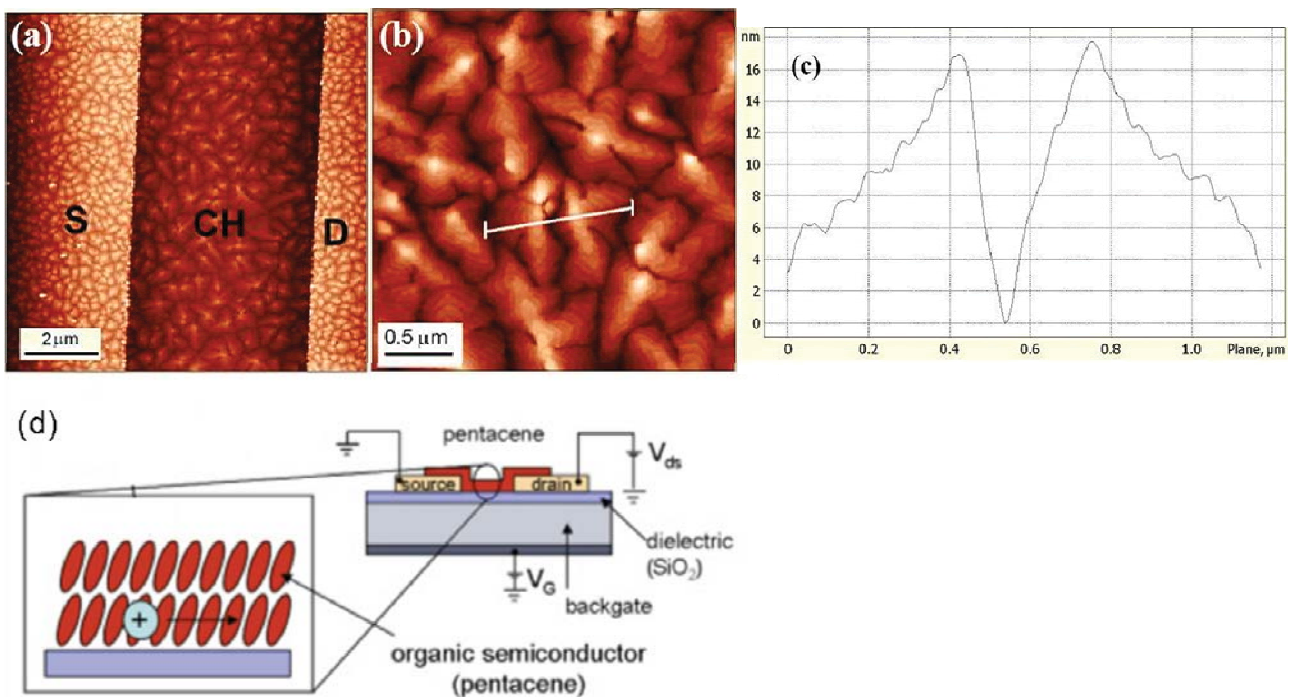


Figure 5.3.1: (a) Morphology of a 20 nm thick Fraunhofer testpattern with 5 μm channel length and pentacene as active material. (b) Magnification of the central channel region. (c) Height profile across the white line in (b) exhibiting terraced structures. (d) Schematic representation of a working pentacene OFET with zoom on standing layers of molecules required for ideal charge transport [Courtesy of Dr. Arian Shehu and Dr. Santiago Quiroga].

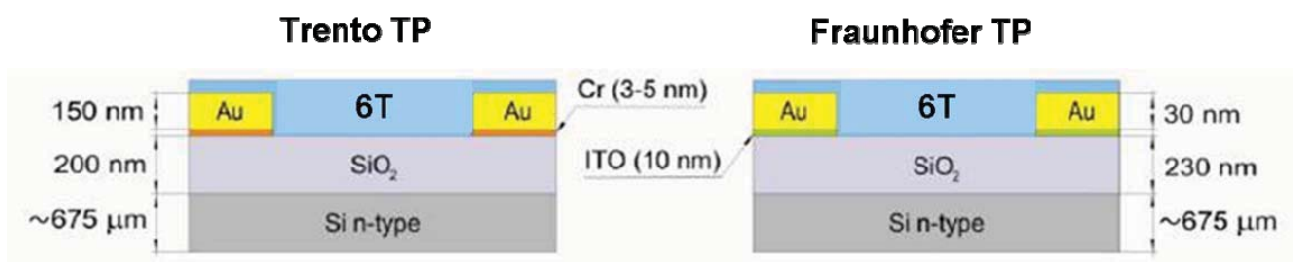


Figure 5.3.2: Comparison of the cross section of the Trento-type (left) and the Fraunhofer-type testpatterns [Courtesy of Dr. Santiago Quiroga].

The experimental conditions for all in-situ real-time morphology evolutions are kept the same. The cell temperature is 260°C and the substrate temperature is 100°C at a base pressure of 4×10^{-9} mbar what translates into an effective deposition rate of about 0.7 Å/min as verified by integral coverage versus deposition time analysis from a morphology sequence like shown in Figure 5.3.3 . The first three images for 10, 20 and 30 min total deposition time have been taken in the same surface regions and illustrate how the initially dendritic islands slowly fill up and develop a roundish shape before the second layer starts to nucleate. Note that from the first deposition of 10 min few three dimensional crystallites form at the lower third of the image. Note further that coverage on the SiO_x outside the channel exhibits a slightly higher coverage than inside the channel. Therefore the data point at 40 min is not included in the deposition rate estimate. The higher coverage is most likely associated to the fact that far from the confining 150 nm high gold electrodes the material does not aggregate at the gold step and diffusion is hence less confined.

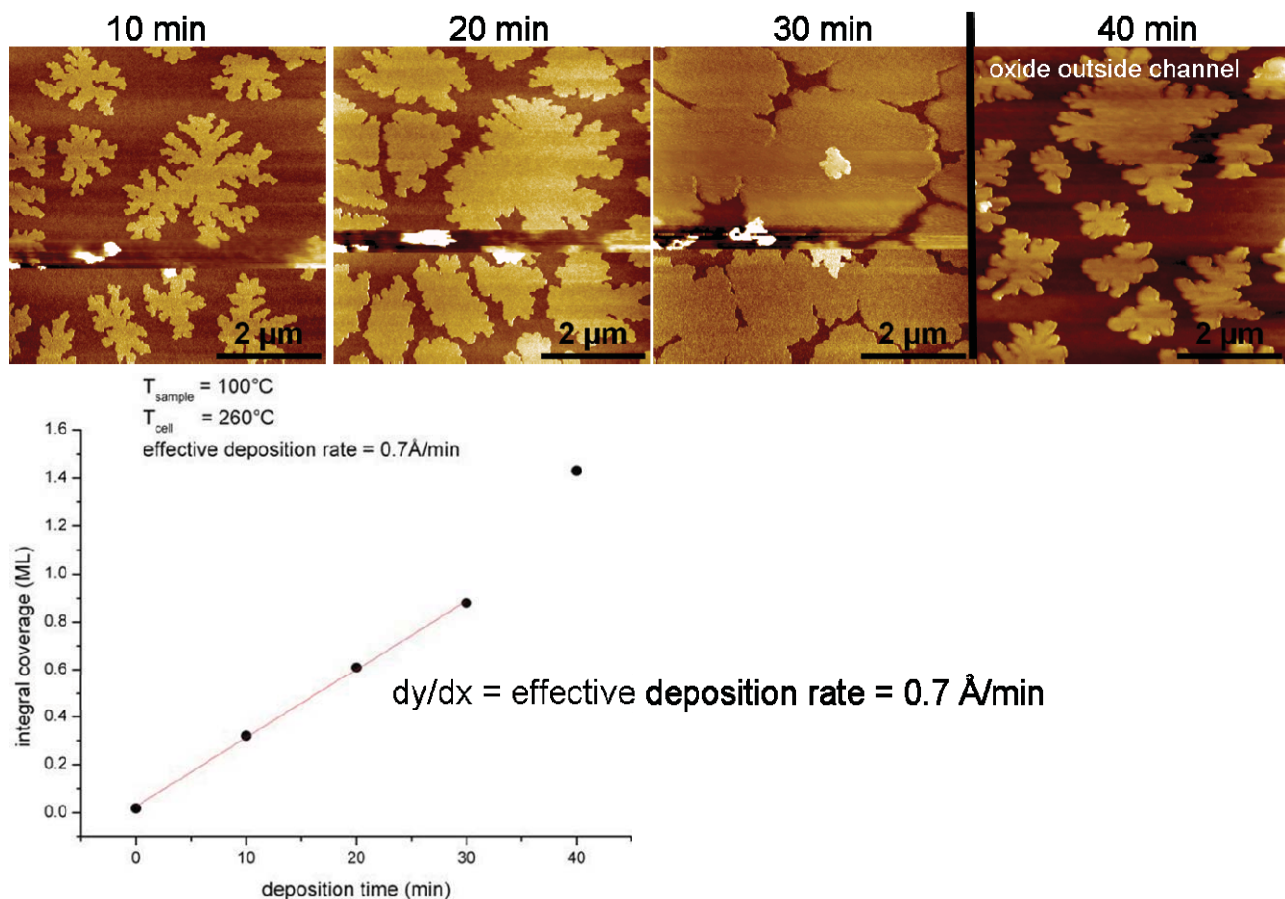


Figure 5.3.3: Coverage evolution inside the Trento TP channel (10–30 min) and morphology on the oxide outside the channel (top). The morphology sequence is used to determine the effective deposition rate.

6.1. 6T on Trento-type testpattern

The large height differences of 150 nm between the gold electrode and the channel of the Trento-type testpattern, limit substantially the investigation of submonolayer growth scenarios by NC-AFM in UHV. However including only the lower border of the electrode double step (REF chapter) with a height difference of about 30 nm, we can achieve a good and stable resolution of the charge injection interface that determines crucially the device performance.

Seeding of around 400 nm big islands prior to the stepwise deposition was found to favor the formation of flat crystals. The seeding procedure consists of the ultra low rate deposition to a thickness corresponding to 5% surface coverage onto a testpattern kept at room temperature.

The following real-time deposition image sequence in Figure 6.1.1 reveals already after 20 min of 6T deposition onto the pre-seeded electrode/channel interface two types of molecular organization. They can easily be distinguished by their larger height and their straight-edged crystalline shape. The islands nucleate between the crystals are initially just one monolayer high and display dendritic or round shapes. The islands are assumed to be composed by polycrystalline 6T incorporating different domains of orientation and defects.

Interestingly, the pre-seeded crystals develop in a layer-by-layer growth and incorporate the organic material from surrounding islands as they grow. Note that the islands do not connect to the gold electrode on the left throughout the entire sequence. The crystals however connect to the gold electrodes and even nucleate at the vertical electrode step (see 40min). Further crystals are supposed to allow for better charge transfer conditions and this pre-seeding technique could therefore be explored for fabrication of devices with higher mobility.

The process of in-situ molecular recrystallization into flat crystals of homogeneous height and with a preferential lateral growth induced by crystal seeds seems to be a promising approach for a growth phase optimization in organic electronics in order to increase the charge injection and device performance.

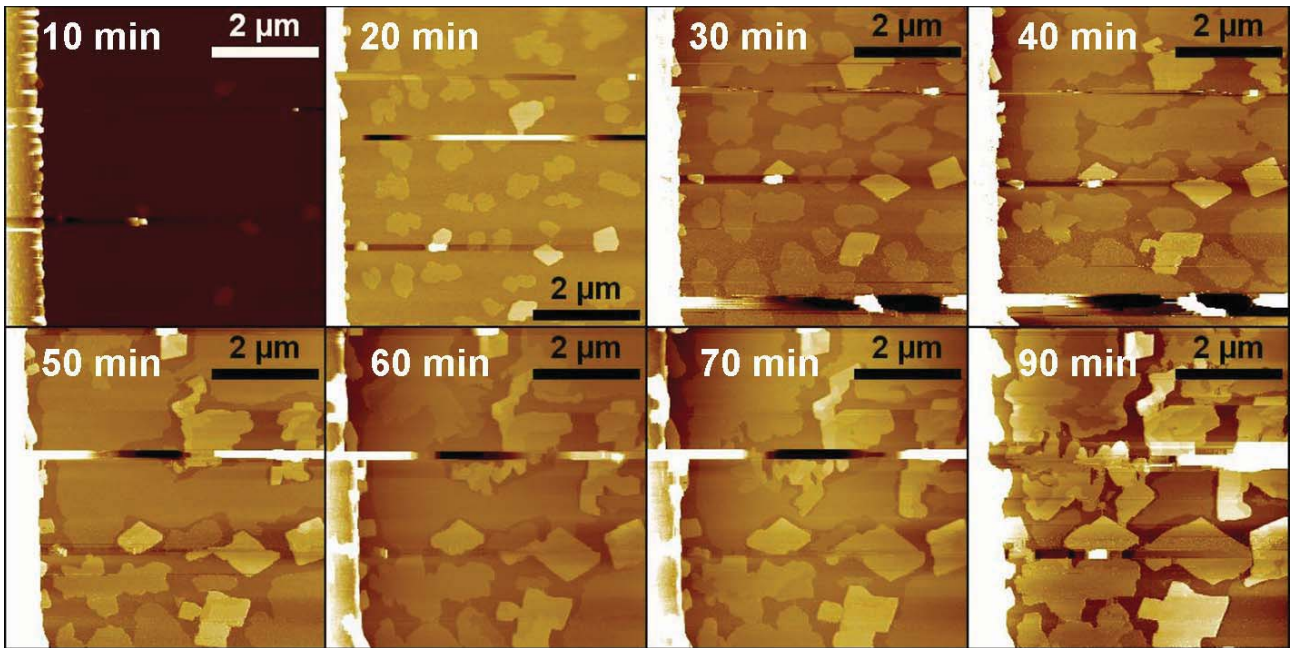


Figure 6.1.1: AFM crystal growth dynamics sequence at a deposition rate of $0.7 \text{ \AA}/\text{min}$ on a pre-seeded Trento TP at the electrode/dielectric interface. Minutes in white are the total deposition time.

6.2. 6T on Fraunhofer-type testpattern

The Fraunhofer testpattern (REF) comprises OFET teststructures with four different channel lengths from $2.5 \mu\text{m}$ to $20 \mu\text{m}$. We present here the morphological evolution of a gold/silicon oxide/gold interface with a channel length of $2.5 \mu\text{m}$. The numbers in white indicate the total 6T sublimation time at an effective deposition rate of $0.7 \text{ \AA}/\text{min}$ onto the 100°C hot testpattern heterostructure. The very narrow channel and the only 25 nm high gold electrodes. Further the Fraunhofer gold electrodes have a much lower surface roughness than the Trento or Arandee gold surfaces which use chromium instead of ITO. Figure 6.2.1 shows the morphological evolution during 6T deposition up to a nominal thickness of 9.8 nm with total deposition time in white. Due to the large height ranges compared to the length scale of 6T molecules ($2\text{-}3\text{ nm}$) we first put a focus on the structures on the gold electrodes in Figure 6.2.1 and then a focus on the channel oxide in Figure 6.2.2. This splitting can be extracted from SPM images by a variation of the graphically displayed range of the height histogram.

The morphology evolution of the gold electrodes is determined by 3 types of 6T aggregation: standing islands of dendritic shape (most likely preceded by a flat lying overlayer), flat lying extendend islands and needle-like 3D crystallites.

At early growth stages up to 30 min most of the 6T adsorbs in form of 3D crystallites around the electrode edge. At 40 min two large and smooth islands of flat lying 6T reach from the right into the image while standing islands have their major evolution from 80-140 min. The standing islands follow a self-similar dendritic growth. From the sequence in Figure 6.2.1 it is likely that the percolation path and performance of the device is dominated by transport through needle-like polycrystallites with an average height of about 200 nm (see Figure 6.2.3).

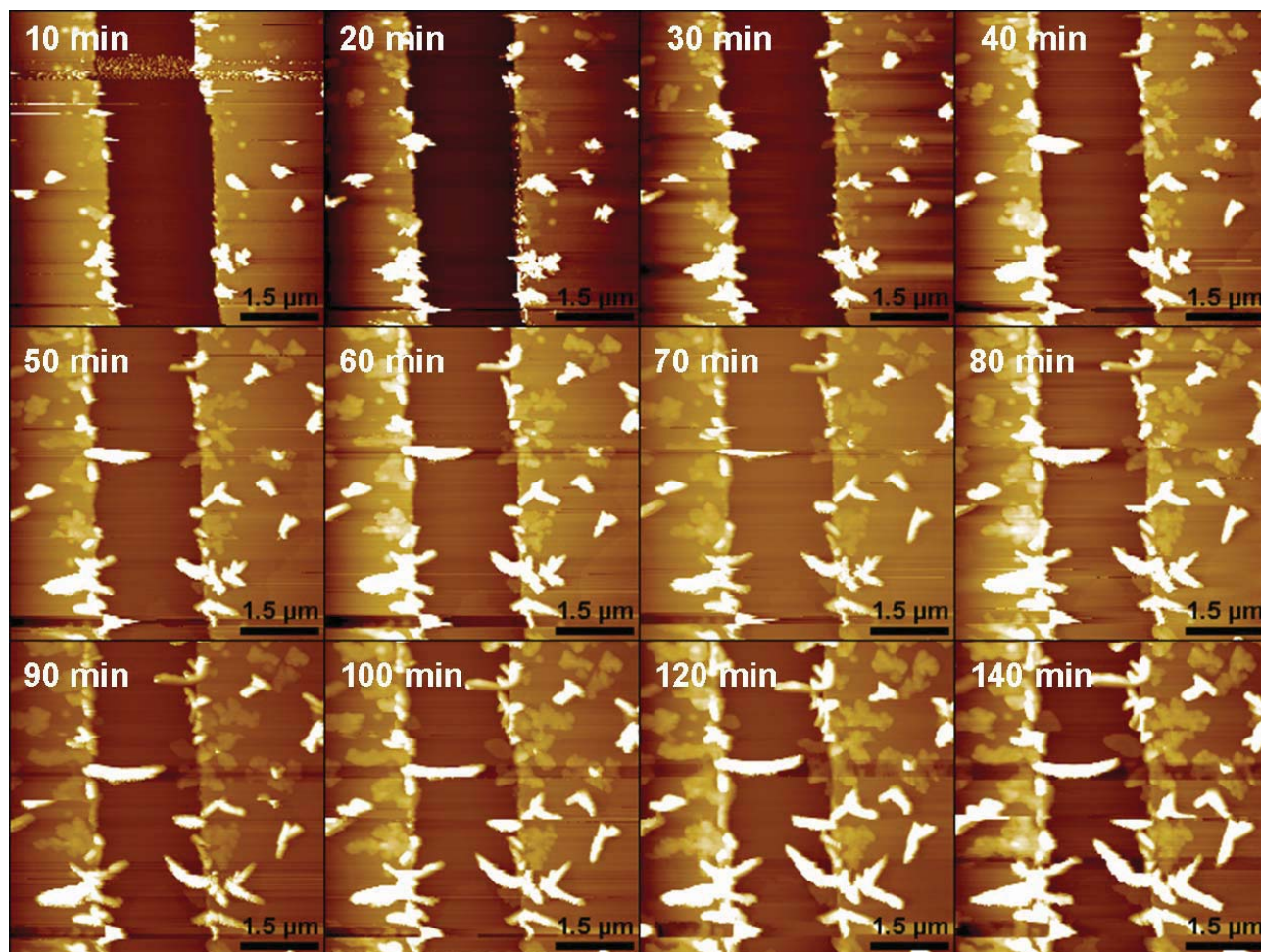


Figure 6.2.1: AFM growth dynamics sequence of 6T with focus on the morphological evolution on the gold electrodes.

Figure 6.2.2 shows again the same morphological evolution but with focus on the structures growing inside the channel. At 30 min there is the first evidence of a 6T island of standing molecules that keeps on growing continuously extending along the channel rather than assuming a circular shape. The island touches the crystallites grown at the electrode edge after about 80 min. After 90 min flat crystals start to grow into the channel. The 6T polycrystals at the electrodes seem to seed the flat crystals. At 140 min (9.8 nm) a second layer island nucleates on top of the standing island instead of assembling into the uncompleted first monolayer like in perfect layer by layer growth.

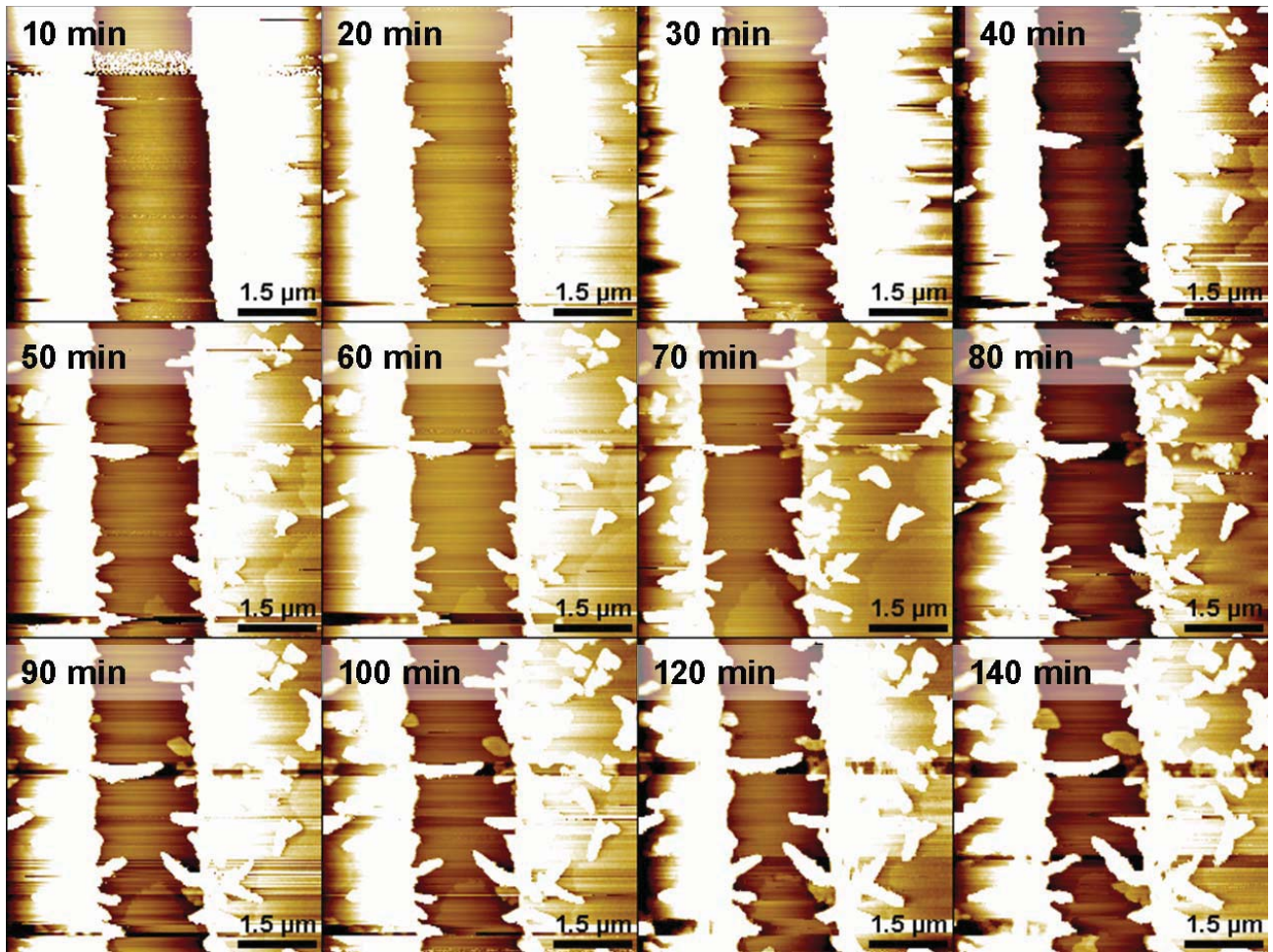


Figure 6.2.2: AFM growth dynamics sequence of 6T with focus on the morphological evolution in the SiO_x channel between the gold electrodes.

When the electrical response of the device is measured during real-time in-situ deposition, the onset of drain current occurs due to the first so-called percolation path, the first semiconducting connection between the electrodes. In Figure 6.2.3 the first two morphological connections are shown as magnifications of the regions A and B at the end of the deposition. Both have in common that the structural connection includes 6T polycrystallites. In region A a flat layer by layer grown crystal probably seeded from the polycrystallites at the electrode edge completes the connection. In region B a single standing monolayer island connects the electrodes though the polycrystallites at multiple points.

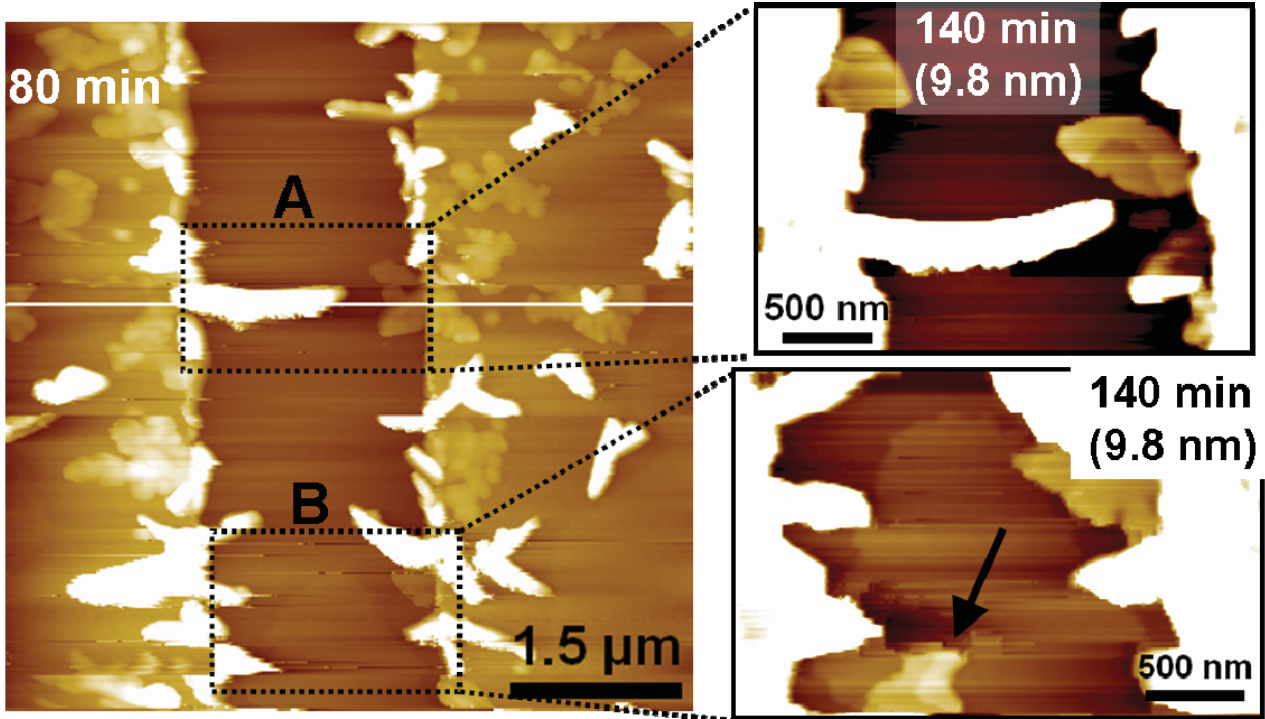


Figure 6.2.3: The first two structures to bridge the channel are shown as magnification of region A and B together with a height profile along the white line.

6.3. Molecular reorganization during OMBD and NC-AFM

In the real-time in-situ experiment, the sample is kept at a chosen temperature (here 100°C) and intervals of deposition alter with intervals of NC-AFM surface imaging. In particular, an interval of 10 min of deposition is followed by imaging the corresponding morphology at closed cell. This procedure differs from the commonly used one-shot deposition up to the desired thickness since we have a vibrating probe that interacts with the film surface rastering every point on in the selected image frame and we add annealing time to the growth process. During the annealing time, the beam is interrupted and the film can evolve on a molecular scale using the energy provided from the heating stage. We have observed two major reorganization phenomena that we want to discuss in the following.

The first reorganization phenomenon occurred when imaging a freshly sublimed submonolayer 6T film onto the Trento-type thermal silicon oxide using a low force constant cantilever. At a submonolayer coverage level, we found three dimensional crystallite structures in 90% of all images on independent sample positions from the first scan. Sometimes they were evolving upon repeated scanning of the same surface area. It is difficult to obtain clear images as the measurement becomes unstable when passing over three dimensional structures. We can assume that the reason for this unstable measurement conditions is the radically changing scanning height and the different nature of interaction between the in UHV oscillating cantilever and the above mentioned 3D crystalline 6T structures. However it is also possible that the scanning tip induces the reorganization or directly modifies the film. Figure 6.3.1 shows a scan sequence of three images taken one after another. The first scan does not show any structures above 1ML height apart the small second layer nucleation in the bottom center island. The second scan instead is considerably disturbed by high structures. The almost 45° orientation of the protruded stripe could indicate a tip mediated pick up and release mechanism. Another hypothesis is that the thermal energy of 100°C provided to the organic film induces local recrystallization, facilitated possibly by defects or impurities on the silicon oxide. However in the third scan the parallel stripes are gone. Nonetheless the only about 20 nm high 3D structures disturb both homogeneous layer by layer growth and NC-AFM imaging. The latter probably suffers both from the sudden change in height (up to several hundred

nanometers) and the strong interaction variation in UHV from submonolayer polycrystalline islands to 3D structures.

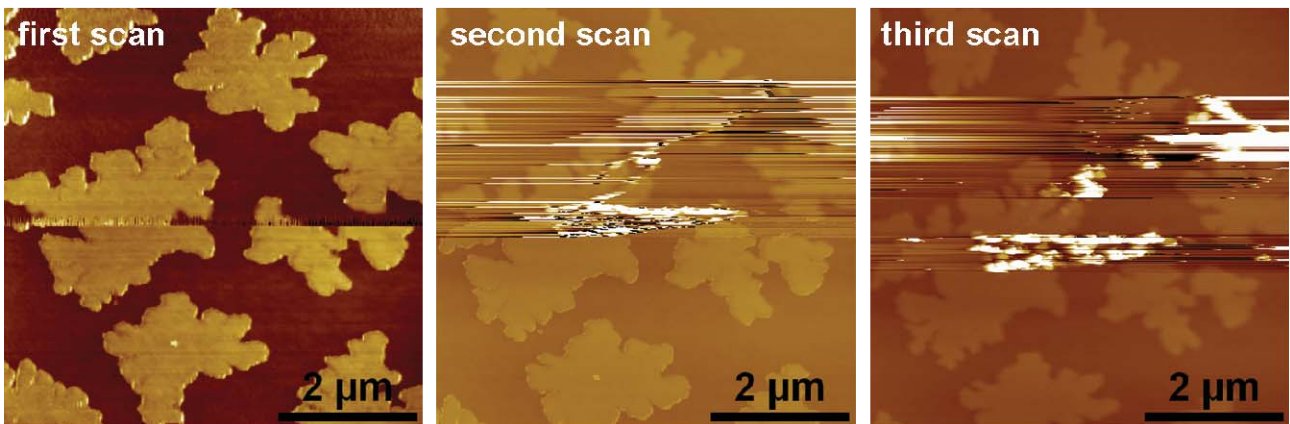


Figure 6.3.1: Consecutive NC-AFM scan sequence on a submonolayer 6T film. 3D structures form spontaneously from the second scan on.

If we zoom down on regions of these spontaneously formed 3D structures, the signal stabilizes and several hundred nanometer big crystallites emerge. Figure 6.3.2 shows the original zone of instability and a zoom-in on it together with a height profile and estimated step heights. The average height of these crystallites is 10-30 nm, but also much higher crystallites form.

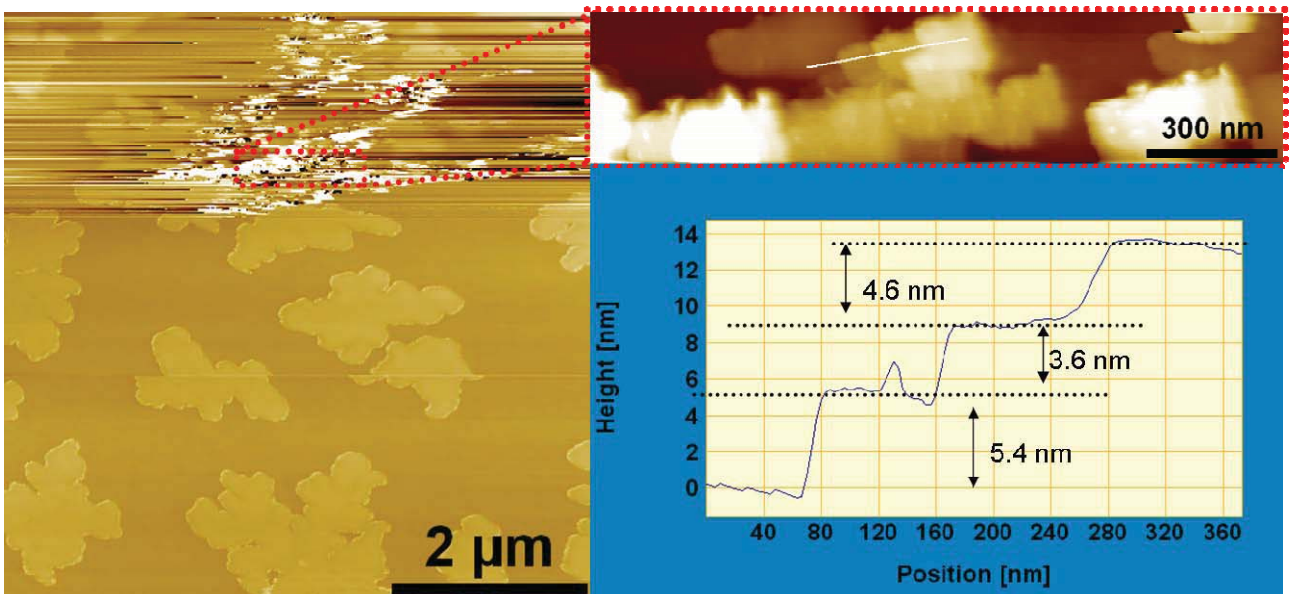


Figure 6.3.2: Zoom-in on a region of spontaneously formed 3D structures of 6T and respective profile with terrace heights.

Three dimensional 6T crystallites interact with the 6T molecules that diffuse on the hot surface and even with already formed islands as shown in Figure 6.3.3. The crystal's so-called capture zone is huge and hence they feed also from already adsorbed islands within their capture zone. This effect also occurs when 6T crystallizes around a surface defect or impurity and usually leads to the formation of an isolated crystal surrounded by a depletion zone that exposes the substrate. Figure 6.3.3 A - D show an identical surface section with different height histogram focus to highlight the multi-scale character of this reorganization phenomenon. The profiles for Figure 6.3.3B, C and D are shown on the right. Standing islands, flat crystals and 3D polycrystalline agglomerates confirm above stated height ranges for the different structures. The latter 3D polycrystalline structures of about 30 nm height as shown in profile B could act as polarized charge traps but in any case they represent a physical interruption of a possible percolation path. The depletion zones around the crystallites are evident in Figure 6.3.3 from the NC-AFM micrographs and height profiles. A high quantity of heterogeneous crystals is assumed to have negative impact on the device performance.

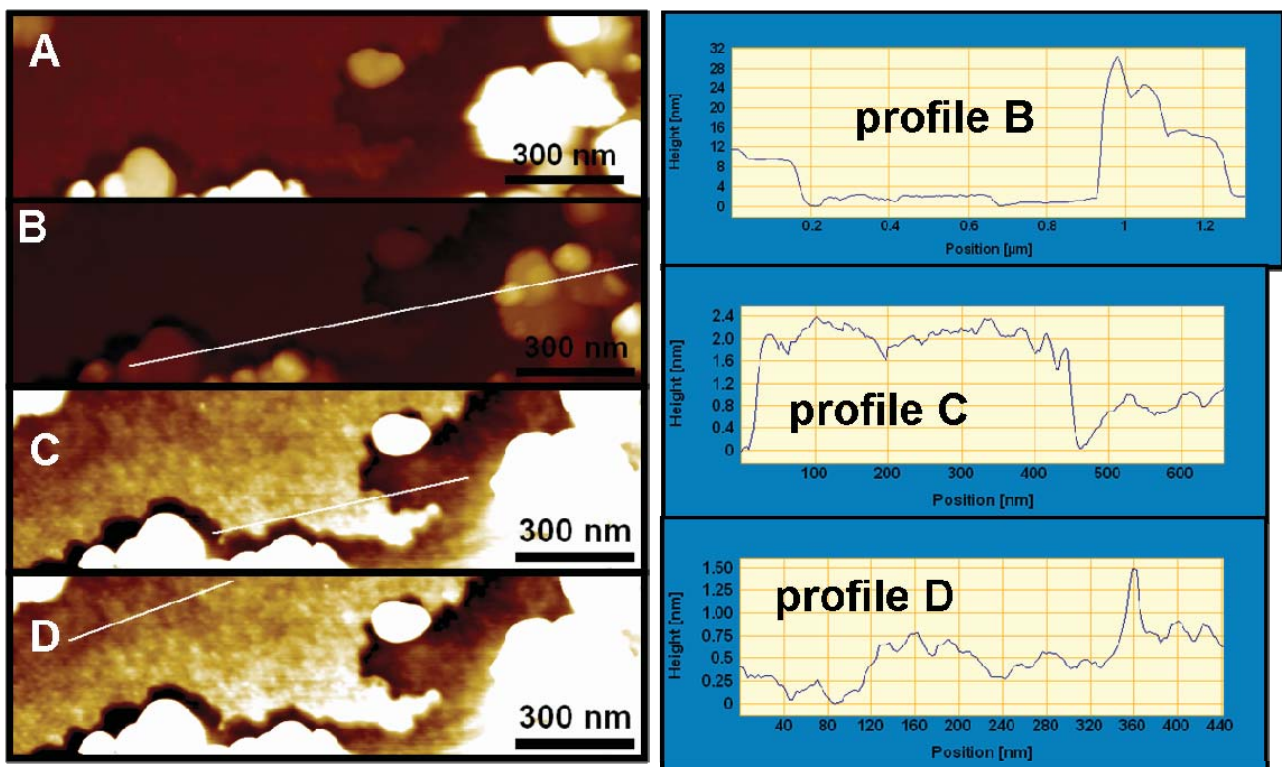


Figure 6.3.3: Interface between polycrystalline 3D structures and standing monolayer islands on SiO_x at different height histogram focuses. The white lines in (B), (C) and (D) are height cross sections shown on the right.

The second reorganization phenomenon is observed when we keep the film at the original substrate temperature of 100°C for 48h after the deposition.

Figure 6.3.4 shows the still ongoing morphology changes in time on a 6.3 nm thick pre-seeded 6T film on a Trento-type testpattern kept at 100°C after deposition for 48h. The AFM micrographs show the charge injection region and comprise the gold electrode border on the left side. The long term annealing was originally carried out to see if the seeding induced crystal phase in Figure 6.1.1 can extend and form fully connected networks of flat crystals for optimized charge transport. Interestingly, it was found that even after a post-growth annealing of 48h the molecules are still reorganizing into flat crystals of 6T. The black arrows in Figure 6.3.4 evidence the two regions where 6T molecules have enough energy to assemble into ordered layers on to of the flat crystals. Figure 6.3.4 shows the growth of an additional layer and a starting nucleation on a time scale of 70 min. The final overview clearly shows that locally also very high structures build up. This might be one of the reasons why the here investigated 6.3 nm thick 6T film is probably too thin to form a percolation network of flat crystals ranging from source to drain.

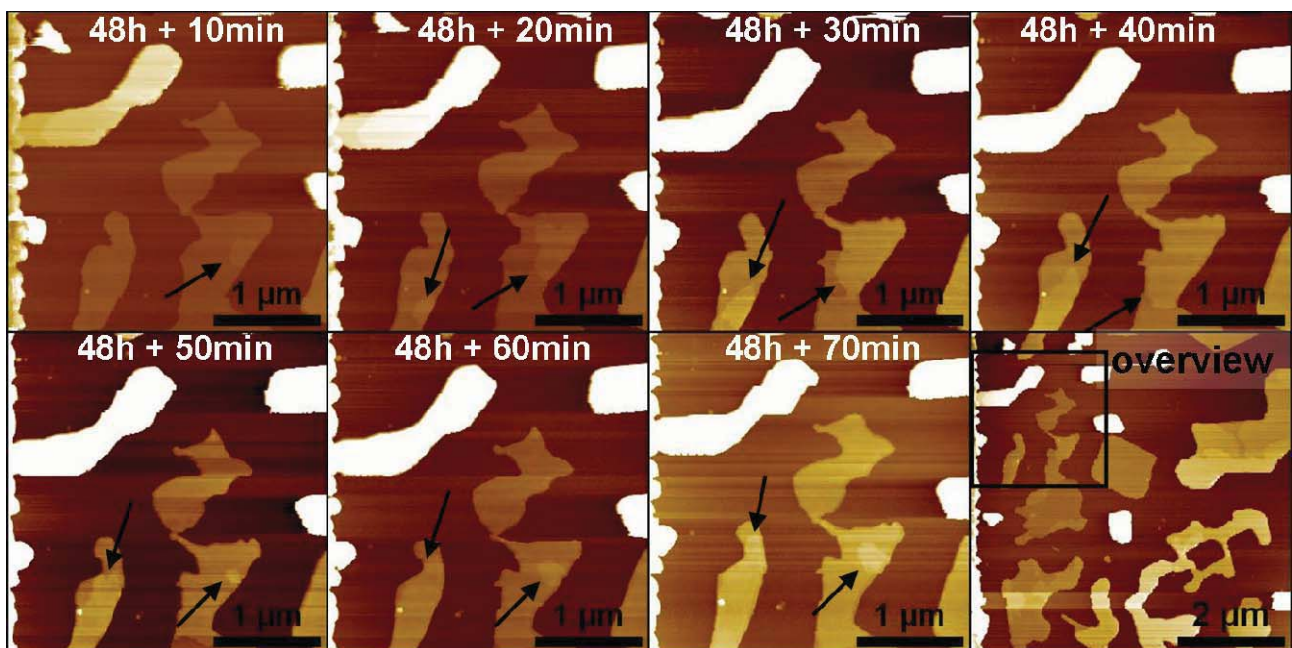


Figure 6.3.4: Sequence of post-growth annealed sample shown in Figure 6.1.1. Even after 48h molecular reorganization at 100°C substrate temperature occurs by up-step diffusion.

Figure 6.3.5A and B show a direct comparison of the film morphology after 48h and after 49h. Both AFM micrographs contain evidenced height cross sections that are shown in Figure 6.3.5C for the 48h case and in Figure 6.3.5D for the 49h case. The profiles across the flat crystals in Figure 6.3.5A show that crystal connected to the electrode and extending over the channel has about the same height as the electrode (see profile 4). The profiles 1, 2 and 3 have about the same height of about 7-12 nm. Their height can be associated with the number of standing monolayers that have display a height of about 2.4 nm each. Hence after 48h of annealing, profile 1 consists of 4 ML (9.6 nm), profile 2 of 3ML (7.2 ML) and profile 3 of both 3ML and 4ML as it shows the nucleation of a new layer at the right crystal border.

If we look at Figure 6.3.5D after 49h of annealing, we can clearly see and measure the layers that have grown on top of the crystal. Profile 1 intersected by the black dotted line confirms the growth of one additional layer, in the case of profile 3, here evidenced by a red circle, up to 3ML plateaus are traced in the height profile.

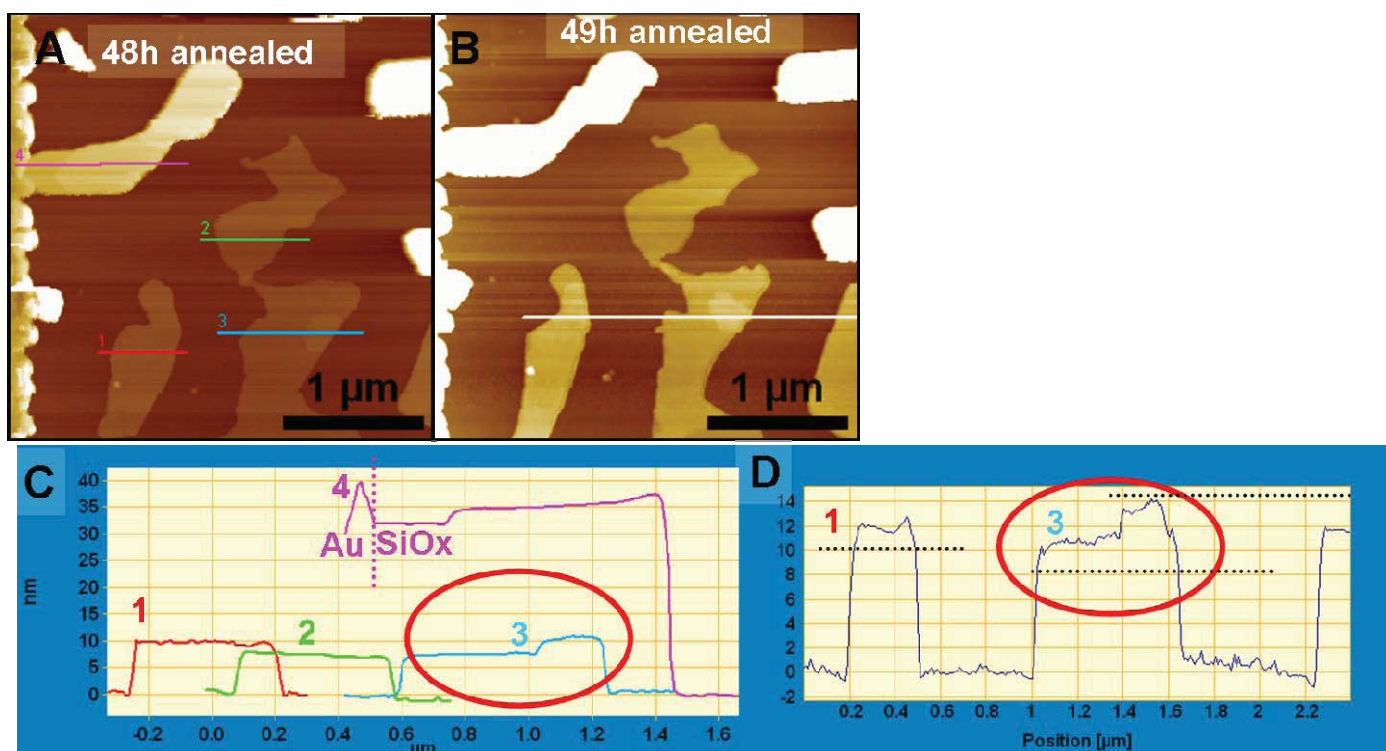


Figure 6.3.5: (A) Electrode/channel interface of 6.3 nm thick 6T film after 48 h annealing at 100°C. The evidenced cross sections are shown in (C). (B) Final morphology after 49h of annealing. The respective height profile in (D) shows the completion of one monolayer and the nucleation of the second.

What molecular processes and orientational transitions occur on top of the islands and crystals? Organic materials are remarkable because they can be grown in molecular layers following a Frank-van-der-Merwe layer by layer growth mode. That means even though in OMBD a constant flux of a molecular beam hits constantly the surface the growth mode is not ballistic. Surface and thermal energy mediated processes together with intermolecular forces of the evaporant molecules lead to interlayer transfer processes. In a perfect layer by layer growth the molecules that land onto existing islands of an uncompleted layer are transferred downwards and assemble into the existing islands. However also upward transfer processes exist like shown in Figure 6.3.5 for long annealing times. Further there are single molecule orientational transitions that are related to the molecular diffusion process of the evaporant on the bare surface and on the first monolayers. In the case of 6T the orientation of the long molecular axis with respect to the surface is under debate since flat lying 6T molecules have been found on thermal oxide and on the top of 6T islands.

We demonstrate here that high resolution NC-AFM in UHV can detect flat lying molecules on top of the seeded flat crystals shown in Figure 6.3.6. Therefore we scan in the center of the monolayer flat crystal in order to obtain the best height resolution. An upward transfer of molecules has been confirmed in post-growth annealing experiments (see Figure 6.3.4). So if we detect flat lying molecules they start to stand up at a certain point, probably driven by the existence of a critical nucleus size (4 molecules in the case of 6T).

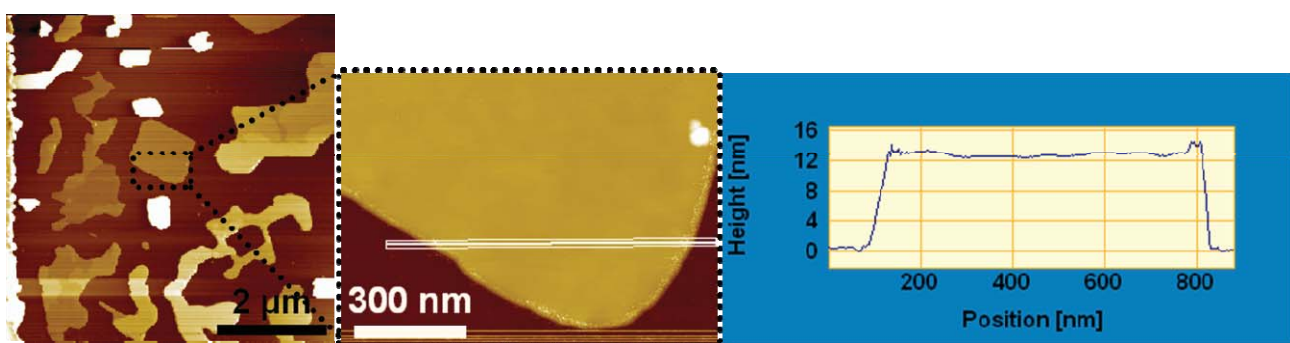


Figure 6.3.6: Morphological overview after 49h of annealing and details of a 12 nm high flat crystal (5ML of standing 6T).

Figure 6.3.7 shows the surface details of the crystal in Figure 6.3.6. We observe a grain-like background roughness apparently resembling the silicon oxide morphology even though the crystal height is 12 nm or 5 ML. At the edge of the crystal domain-like flakes, some with straight crystal reminiscent borders. Figure 6.3.7B represents a zoom taken in the center of the crystal. The shape of the domains is here less crystal reminiscent. It can be assumed that the oscillating cantilever tip modifies the diffusing and reorganizing 6T domains due to the interaction with the tip. A height cross section along the white lines is shown for both AFM micrographs in Figure 6.3.7C and D. In both cases the profile height is about 600-750 pm which is the expected height of a flat lying 6T molecular domain on the crystal surface.

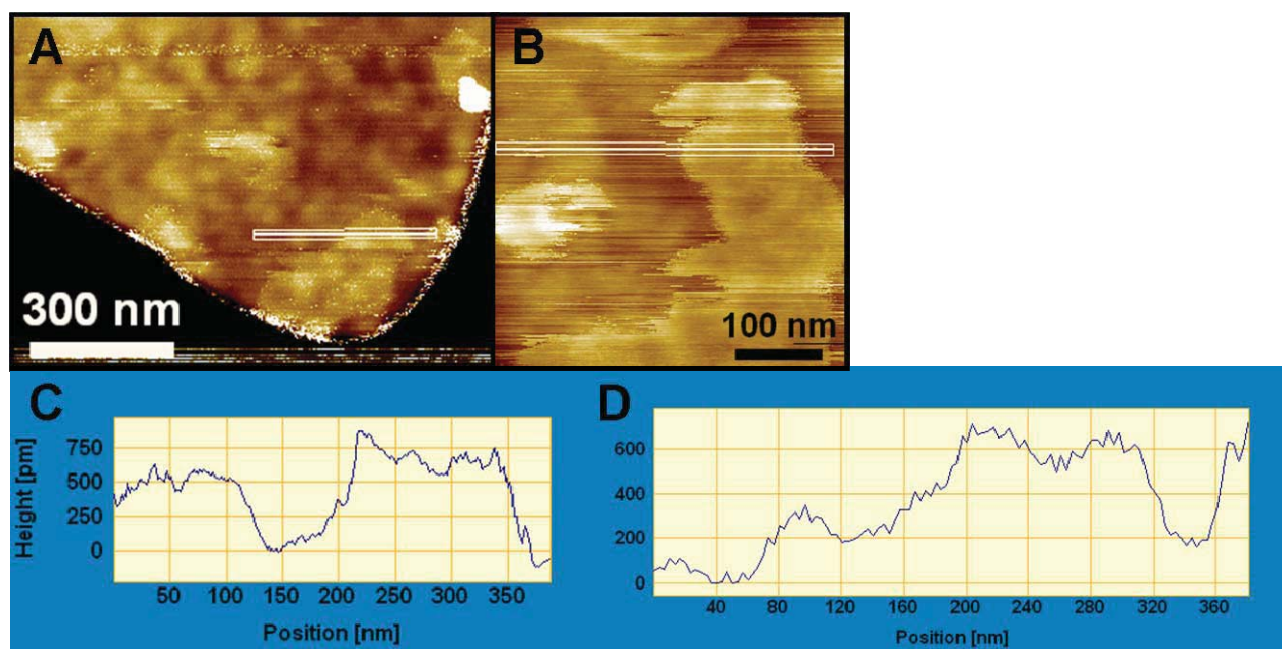


Figure 6.3.7: (A) Surface details of the 6T crystal shown in Figure 6.3.6 . (B) Magnification of the flat crystals central region. (C) Height cross section along the white line in (A). (D) Height cross section along the white line in (B).

6.4. Summary

In this chapter two different types of commercial OFET testpattern structures have been investigated by Non-Contact AFM during growth of the organic material using an in-situ real-time deposition system together with a variable temperature UHV SPM.

A pre-seeding technique in order to promote successfully the growth of flat crystals instead of polycrystalline islands. The approach seems promising but electrical characterizations are still to be performed.

A detailed sequence of the morphological evolution across a channel comprising both source and drain electrodes revealed the presence of standing and lying islands, polycrystallites and flat crystals that form together the first electrical connection. The dominating role - at least when using small channel lengths – is likely played by the polycrystallites.

An outlook could be to try to associate the electrical parameters of the transfer curves used to characterize FET devices and especially the coverage at percolation with the morphology. For this purpose two in-situ real-time growth chambers could be employed: one with deposition onto a connected testpattern and the other monitoring the morphology by AFM at defined times during growth.

7. References

-
- ¹ E. Da Como, “Morphology correlated photophysics in organic semiconductor thin films”, PhD thesis, University of Bologna, 2006.
- ² F. Dinelli, M. Murgia, P. Levy, M. Cavallini, F. Biscarini, and D. de Leeuw, “Spatially correlated charge transport in organic thin film transistors”, *Phys. Rev. Lett.*, 92, 116802, 2004.
- ³ J. Koenigsberger, K. Schilling, *Ann. Physik* **32**, 179 (1910).
- ⁴ M. Volmer, *Ann Physik* **40**, 775 (1913).
- ⁵ E. A. Silinsh, *Organic molecular crystals*. Springer, Berlin 1980.
- ⁶ M. Pope and C. E. Swenberg, *Electronic processes in organic crystals*, Clarendon Press, Oxford 1982.
- ⁷ F. Ebisawa, T. Kurokawa, and S. Nara, *J. Appl. Phys.* **54**, 3255 (1983).
- ⁸ A. Tsumura, H. Koezuka, T. Ando, *Appl. Phys. Lett.* **49**, 1210 (1986).
- ⁹ K. Y. Jen, G. G. Miller, and R. L. Elsenbaumer, *J. Chem. Soc.-Chem. Commun.* 17, 1346 (1986).
- ¹⁰ A. Assadi *et al.*, *Appl. Phys. Lett.* **53**, 195 (1988).
- ¹¹ C. W. Scherr, *J. Chem. Phys.* **21**, 1582 (1953).
- ¹² V.C. Sundar, J. Zaumseil, V. Podzorov, E. Menard, R.L. Willet, T. Someya, M.E. Gershenson, and J.A. Rogers, „Elastomeric transistor stamps: Reversible probing of charge transport in organic crystals”, *Science*, 303, 1644, 2004.
- ¹³ Z. Bao, J. Locklin, *Organic Field-Effect Transistors*, CRC Press, Boca Raton, 2007.
- ¹⁴ J.H. Kang, X.Y. Zhu, *Appl. Phys. Lett.* 82, 3248 (2003).

-
- ¹⁵ A.Brillante, R.G. Della Valle, L. Farina, A. Ghirlando, M. Masino, E. Venuti, *Chem. Phys. Lett.* 357, 32 (2002).
- ¹⁶ T. Siegrist, Ch. Kloc, J.H. Schoen, B. Batlogg, R.C. Haddon, S. Berg, G.A. Thomas, *Angew. Chem. Int. Ed. Engl.* 40, 1732 (2001).
- ¹⁷ D.J. Grundlach, Y.Y. Lin, T.N. Jackson, S.F. Nelson, D.G. Schlom, *IEEE Electron Device Lett.* 18, 87 (1997).
- ¹⁸ D. Fichou, F. Charra, A.O. Gusev, *Adv. Mater.* 13, 555 (2001).
- ¹⁹ M.A. Loi, E. Da Como, F. Dinelli, M. Murgia, Roberto Zamboni, Fabio Biscarini and Michele Muccini, Supramolecular organization in ultra-tin films of sexithiophene on silicon dioxide, *Nature Materials* 4, 81, 2005.
- ²⁰ Y. Zheng, D. Qi, N. Chandrasekhar, X. Gao, C. Troadec, A.T.S. Wee, *Langmuir* 23, 8336 (2007).
- ²¹ Binnig, G.; Rohrer, H.F.: Vacuum Tunnel Microscope. In: *Helv. Phys. Acta*, volume 55:pp. 128–128, 1982.
- ²² Binnig, G.; Rohrer, H.F.; Gerber, C.; Weibel, H.: Tunneling through a controllable vacuum gap., *Appl. Phys. Lett.*, volume 40:pp. 178–180, 1982.
- ²³ C. Klok, P.G. Simpkins, T. Siegrist, and R.A. Laudise, “Physical vapour growth of cm-sized crystals of α -hexathiophene”, *J. Crystal Growth*, 182, 416-427, 1997.
- ²⁴ G. Horowitz, B. Bachet, A. Yassar, P. Lang, F. Demanze, J-L. Fave, F. Garnier, Growth and characterization of sexithiophene single crystals, *Chem. Mater.* 7, 1337 (1995).
- ²⁵ F. Meinardi, M. Cerminara, S. Blumdtengel, A. Sassella, A. Borghesi, R. Tubino, Broad and narrow bands in the photoluminescence spectrum of solid state oligothiophenes: Two marks of an intrinsic emission, *Phys. Rev. B* 67, 184205 (2003).
- ²⁶ R. N. Marks, R. H. Michel, W. Gebauer, R. Zamboni, C. Taliani, R. F. Mahrt, M.Hopmeier, Disorder influenced optical properties of α -sexithiophene single crystals and thin evaporated films, *J. Phys. Chem. B* 102, 7563 (1998).

-
- ²⁷ B. Servet, G. Horowitz, S. Ries, O. Lagorsse, P. Alnot, A. Yassar, F. Deloffre, P. Srivastava, R. Hajlaoui, P. Lang, and F. Garnier, "Polymorphism and charge transport in vacuum evaporated sexithiophene films", *Chem. Mat.*, 6, 1809-1815, 1994.
- ²⁸ J.F. Moulin, R. Kshirsagar, F. Dinelli, and F. Biscarini, "In situ x-ray synchrotron study of organic semiconductor ultrathin films growth", *Nucl. Instr. Met. B*, 2006.
- ²⁹ G. Horowitz, B. Bachet, A. Yassar, P. Lang, F. Demanze, J-L. Fave, F. Garnier, Growth and characterization of sexithiophene single crystals, *Chem. Mater.* 7, 1337 (1995).
- ³⁰ A. J. Lovinger, D. D. Davis, A. Dodabalapur, H. E. Katz, Comparative structures of thiophene oligomers, *Chem. Mater.* 8, 2836 (1996).
- ³¹ Cynthia Heiner, Order and Symmetries of Sexithiophene within Thin Films Studied by Angle-Resolved Photoemission, Diplomarbeit 2004, Freie Universität Berlin.
- ³² R. Li, P. Buerle, E. Umbach, Vibrational and geometric structure of quaterthiophene on Ag(111), *Sur. Sci.* 331-333, 100 (1995).
- ³³ F. Elfeninat, C. Fredriksson, E. Sacher, A. Selmani, A theoretical investigation of the interactions between thiophene and vanadium, chromium, copper, and gold, *J. Chem. Phys.* 102, 6153 (1995).
- ³⁴ G. Liu, J. A. Rodriguez, J. Dvorak, J. Hrbek, T. Jirsak, Chemistry of sulfur-containing molecules on Au(111): Thiophene, sulfur dioxide, and methanethiol adsorption, *Sur. Sci.* 505, 295 (2002).
- ³⁵ S. Prato, L. Floreano, D. Cvetko, V. DeRenzi, A. Morgante, S. Modesti, F. Biscarini, R. Zamboni, and C. Taliani, Anisotropic ordered planar growth of α -sexithienyl thin films, *J. Phys. Chem. B* 103, 7788 (1999).
- ³⁶ R. Telesca, H. Bolink, S. Yunoki, G. Hadziioannou, P. Th. Van Duijnen, J. G. Snijders, H. T. Jonkman, G. A. Sawatzky, Density-functional study of the evolution of the electronic structure of oligomers of thiophene: Towards a model Hamiltonian, *Phys. Rev. B* 63, 155112 (2001).

-
- ³⁷ Cynthia Heiner, Order and Symmetries of Sexithiophene within Thin Films Studied by Angle-Resolved Photoemission, Diplomarbeit 2004, Freie Universität Berlin.
- ³⁸ A.B. Chwang, C.D. Frisbie, *J. Phys. Chem. B* **2000**, *104*, 12202-12209
- ³⁹ F. Biscarini et al., *J. Chem Phys.* 1998.
- ⁴⁰ Operating Instructions OME-40, Dr. Eberl MEB Komponenten GmbH, Germany 2006.
- ⁴¹ J.Lukkari, M. Alanko, L.Heikkila, R. Laiho and J. Kankare, *Chem. Mater.* *5*, 289 (1993).
- ⁴² F. Matino, L. Persano, V. Arima, D. Pisignano, R.I.R. Blyth, R. Cingolani, and Ross Rinaldi, *Phys. Rev. B* *72*, 085437 (2005)
- ⁴³ S. Pratontep, M. Brinkmann, F. Nuesch, L. Zuppiroli, *Phys. Rev. B* *69*, 165201 (2004).
- ⁴⁴ T.Belser, M. Stoehr, A. Pfaltz, *J. Am. Chem. Soc.*, 2005, *127* (24).
- ⁴⁵ M.A. Loi, E. Da Como, F. Dinelli, M. Murgia, R. Zamboni, F. Biscarini and M. Muccini, *Nature Mat.*, Vol *4*, 2005, 81-85.
- ⁴⁶ PhD Thesis, S.D. Quiroga and A. Shehu, "IN SITU REAL-TIME INVESTIGATION OF ORGANIC ULTRA-THIN-FILM TRANSISTORS: GROWTH, ELECTRICAL PROPERTIES AND BIOSENSING APPLICATIONS", CNR-ISMN Bologna, Italy, 2010.
- ⁴⁷ B. Voigtlaender, André Zinner, and Thomas Weber, High temperature scanning tunnelling microscopy during molecular beam epitaxy, *Rev. Sci. Instrum.* *67*, 2568, 1996.
- ⁴⁸ F.-J. Meyer zu Heringdorf, M.C. Reuter & R.M. Tromp, Growth dynamics of pentacene thin films, *Nature*, vol *412*, 517, 2001.
- ⁴⁹ We can associate the cell temperature to a reproducible flux since the deposited quantities (<3ML) are small compared to the amount of 6T in the crucible (~2 cm³) and the water-cooled effusion cell is optimized for precise temperature control at low deposition rates. Further this has been experimentally verified (graph not shown in this paper).

⁵⁰ G. Ehrlich and F. G. Hudda, *J. Chem. Phys.* **44**, 1039, 1966.

⁵¹ R. L. Schwoebel and E. J. Chipsey, *J. Appl. Phys.* **37**, 3682, 1969.

⁵² J. Yang, T. Wang, H. Wang, F. Zhu, G. Li, D. Yan, *J. Phys. Chem B* 2008, 112, 7821. x

This work is supported by EC FP7 ONE-P Large Scale project no. 212311.